



UNIVERSITA' DEGLI STUDI DI PALERMO

Scuola Politecnica

Computational Modeling of Ascending Thoracic Aortic
Aneurysm and Dissection

TESI DI DOTTORATO DI
ANTONINO RINAUDO

TUTOR
PROF. ANTONINO PASTA

CO-TUTOR
MAGNIFICO RETTORE FABRIZIO MICARI

DOTT. ING. SALVATORE PASTA

DOTTORATO DI RICERCA IN PROGETTAZIONE MECCANICA SSD: ING/IND 14

XXVI CICLO – ANNO ACCADEMICO 2013-2015

Abstract

Cardiovascular diseases account for over 4.3 million of deaths per year in Europe with a 110 billion of Euros as related cost. In particular, aortic aneurysms and especially ascending thoracic aortic aneurysms, increasing the risk of aortic wall rupture and dissection, are related to high mortality and comorbidity.

Epidemiologic studies shown that when ascending thoracic aortic aneurysm reaches 6 centimeter in diameter the risk of aortic rupture dramatically increase to 14% per year. Thus, the criterion adopted in the clinical practice for identification of patients that need a surgical operation is based on the evaluation of the aortic diameter and its comparison with the threshold value of 6 centimeter. This criterion is advantageous for its simplicity but has failed several times, with aneurysm rupture below the indicated threshold value. Indeed, the necessity of a more accurate and reliable criterion, based on biomechanical analyses, that may help physician in their decision making process is evident. This criterion should be based on the synergy of two different approaches (i.e. hemodynamic and genetic). Specifically, the genetic approach proposes that ascending thoracic aortic dilatation relates to aortic wall weakness due to developmental defect, while hemodynamic theory points out the importance of particular flow condition that may lead to excessive loads on aortic wall and thus imparting a permanent aortic wall dilatation. However, the most reasonable theory is that the synergy of genetic and hemodynamic predisposing factors may stimulate the development of aortic permanent dilatation (i.e. aneurysm), rupture or dissection.

Purpose of this work was to study the hemodynamic inside aorta by mean of application of numerical methods to patient specific aortic geometries with ascending thoracic aortic aneurysms. Specifically, computational fluid dynamic analyses and fluid-structural analyses

were applied to aortic geometries to collect relevant parameters, such as Wall Shear Stress, Von Mises Stress and pressure inside aorta, that may play a key role in aortic aneurysm onset and growth.

Since ascending thoracic aortic aneurysm has a high incidence in patients with bicuspid aortic valve, in this study computational analyses were applied to assess hemodynamic conditions in aorta of patients with bicuspid aortic valve and to compare them to those of patients with normal tricuspid valve. Moreover, a deeper study was executed on the hemodynamic differences in aortas with bicuspid aortic valve but different valve phenotypes. This study focused also on the evaluation of hemodynamic in aorta of patients with other pathologies such as type B aortic dissection and penetrating atherosclerotic ulcer.

Contents

Chapter 1

Introduction	1
1.1. Cardiovascular Apparatus Disease	1
1.2. Aorta	2
1.3. Aortic Aneurysm	6
1.3.1. Abdominal aortic aneurysms	7
1.3.2. Thoracic aortic aneurysm	8
1.4. Aortic dissection	10
1.5. Bicuspid aortic valve	12
References	16

Chapter 2

State of the art	19
2.1. Introduction	19
2.2. 4D flow MRI	20
2.3. Computational modeling	21
2.3.1. Fluid structural interaction	23
References	24

Chapter 3

Methodology	26
3.1. Introduction	26
3.2. Fluid structural interaction	27
3.3. Geometry reconstruction	29
3.3.1. Image acquisition: Computer Tomography	30
3.3.2. Image reconstruction: Segmentation and 3D model	31
3.4. Geometry discretization	33
3.5. Computational fluid dynamics analysis	34

3.5.1. CFD preprocessing	34
3.6. Structural model	38
References	41

Chapter 4

FSI application to ATAA study	45
4.1. Introduction	45
4.2. Method	47
4.3. Results	48
4.4. Conclusion	62
References	63

Chapter 5

The role of aortic shape and valve phenotype in aortic pathologies	66
5.1. Introduction	66
5.2. Method	67
5.2.1. Data collection	67
5.2.2. Computational analyses	69
5.2.3. Statistical analyses	72
5.3. Results	73
5.4. Discussion	84
Reference	86

Chapter 6

FSI applied to penetrating ulcer	88
6.1. Introduction	88
6.2. Experimental Procedure	89
6.3. Results	91
6.4. Conclusion	94
Reference	96

Chapter 7

CFD analyses to assess dissected aorta perfusion and predict negative outcome 99

7.1. Introduction	99
7.2. Procedure	100
7.3. CFD analyses	101
7.4. Results	102
7.5. Conclusion	109
Reference	111

Chapter 8

Toward the evaluation of the thoracic aortic stent graft failure risk related to endograft infolding 114

8.1. Introduction	
8.2. Material and Method	115
8.2.1. Phantom and flow circuit	116
8.2.2. Perfusion setting	118
8.2.3. FSI computational modeling	120
8.3. Results	120
8.4. Conclusion	125
Reference	126

Chapter 8

Conclusion 128

Nomenclature

Symbol	Description
3D	Three-Dimensional
AA	Ascending Aorta
AAA	Abdominal aortic aneurysm
AC	Acutely-Complicated
AE	Aneurysm Evolution
AI	Aortic insufficiency
AO	Aortic Stenosis
AoA	Aortic Aneurysm
AoD	Aortic Dissection
AOP	Aortic Valve Plane
AP	Anterior-posterior
ATAA	Ascending Thoracic Aortic Aneurysm
BAV	Bicuspid Aortic Valve
CFD	Computational Fluid Dynamics
CT	Computer Tomography
CTA	Computed tomography angiography
CVD	Cardiovascular disease
CVS	Cardiovascular system
ECG	Electrocardiogram
FEM	Finite Element Method
FL	False Lumen
FPI	False-lumen Pressure Index
FSI	Fluid-Structural Interaction
GCI	Grid Convergence Index

HFI	Helical Flow Index
LSA	Left Subclavian Artery
LV	Left Ventricle
MRI	Magnetic Resonance Imaging
OSI	Oscillatory Shear Index
PAU	Penetrating Atherosclerotic Ulcer
PE	Protrusion Extension
PISO	Pressure-Implicit with Splitting of Operators
PRESTO	Pressure Staggering Option
RA	Right-Antero
RE	Reynolds Number
RL	Right-Left
STJ	Sino-Tubular Junction
TAA	Thoracic Aortic Aneurysm
TAG	Thoracic Aortic Stent-Graft
TAV	Tricuspid Aortic Valve
TAWSS	Time-averaged Wall Shear Stress
TEVAR	Thoracic Endovascular Repair
TL	True Lumen
UDF	User Define Function
UN	Uncomplicated
WPS	Wall Principal Stress
WSS	Wall Shear Stress

Chapter 1

Introduction

1.1. Cardiovascular Apparatus Disease

The cardiovascular system (CVS) is a closed loop that consists of a pump (i.e. the heart), a series of tubes (i.e. the vessels) and a fluid (i.e. the blood), that is pumped from the heart and flows inside the vessels.

In Europe, cardiovascular diseases (CVDs) account for over 4.3 million of deaths per year that correspond to 48% of all deaths in the old continent [1]. Moreover, it has been estimated that, in 2006, Europe spent 110 billion of Euros as CVD related costs. Thus, there is an effective necessity to improve the management of patients with CVD in order to reduce the costs in term of human life and economic resources.

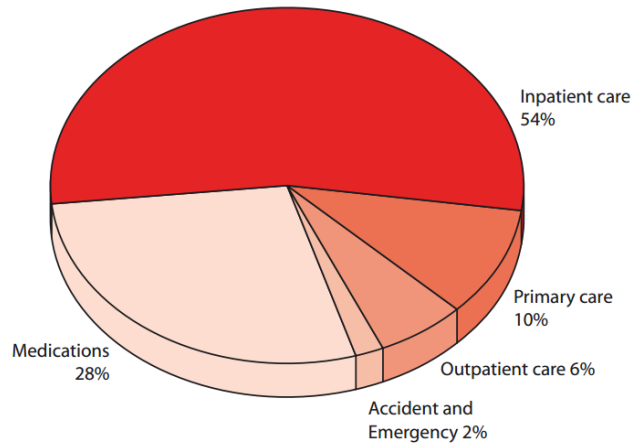


Figure 1.1 Cost of CVD to the European health care system in 2006 [1].

Among the diseases affecting the CVS it is possible to distinguish between those affecting the heart (i.e. cardiomyopathies, heart failure, heart valve diseases) and those affecting the aorta and the other vessels of the CVS (i.e. aortic aneurysm, aortic dissection, coronary artery diseases).

The CVS components degree of complexity lead to an objective impossibility to carry on a study that may fully understand all the CVS disease thus, aim of this work was to study only the aortic pathologies in order to improve the clinical management of patients.

1.2. Aorta

The aorta, the main artery of human circulatory system, carries oxygenated blood from the heart to the periphery of the human body. The aorta is spanned by a unidirectional blood flow ejected by the left ventricle (LV); flow direction is maintained constant by the aortic valve, which opens and closes allowing blood flow from the LV to the ascending aorta and avoiding the blood backflow inside the heart.

The aorta vascularize the closest organs and regions, directly, by mean of collateral branches and the furthest regions, indirectly, by mean of branches that depart from large collateral arteries departing from the aorta.

The aorta is divided into thoracic aorta and abdominal aorta; the thoracic aorta generates from the LV of the heart, just beyond the aortic valve and consists of the aortic root, the ascending aorta (AA), the aortic arch and the descending aorta.

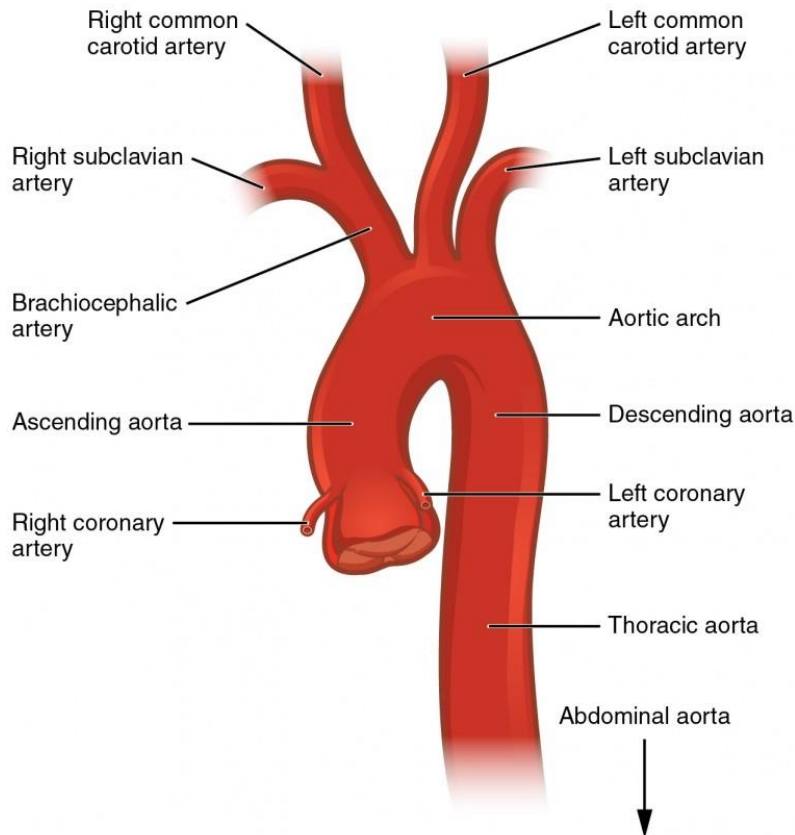


Figure 1.2 Schematic representation of the aorta (<https://commons.wikimedia.org>)

The aortic root consists of the sinuses of Valsalva, the aortic valve leaflets, the commissures and the inter-leaflets triangles. The sinuses (right, left and non-coronary) are aortic root bulges connected to the three aortic valve leaflets and to the sino-tubular junction; they named according to the coronary arteries arising from them. The aortic valve leaflets separate the LV volume to aortic volume and with their motion, allow the blood to flow from the LV to the aorta, during systole and prevent the backflow of blood into the LV during diastole, when the pressure inside aorta becomes higher than the intra-ventricular pressure.

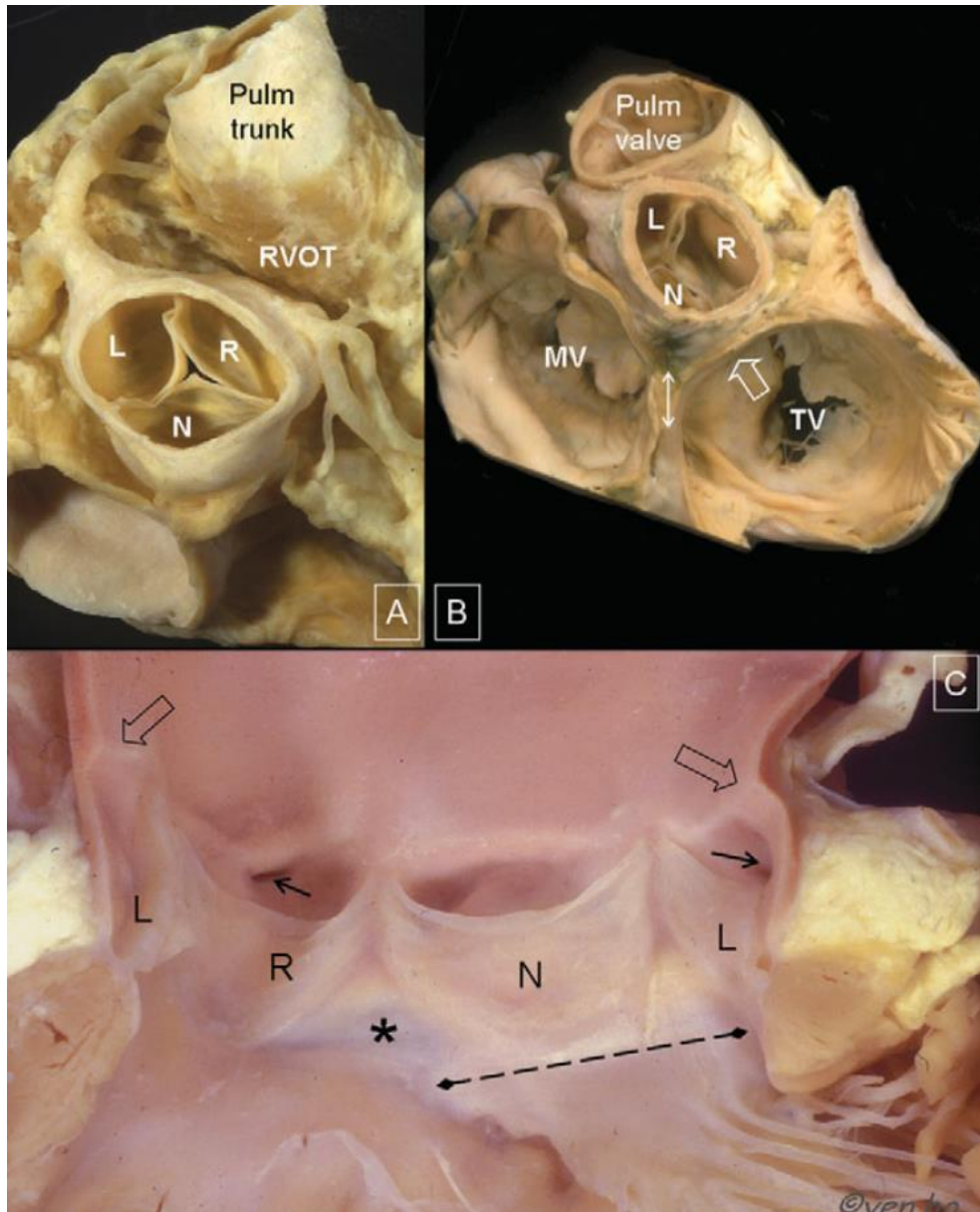


Figure 1.3 (A), (B), (C) Aortic root views.

Left (L), Right (R) and Non-coronary (N) sinuses. R and L sinuses are the closest to pulmonary trunk and give origin to coronary arteries [2]. MV= mitral valve, TV = tricuspid valve.

The aortic arch connects the ascending and descending aorta and from it depart three branches (i.e. the supra-aortic vessels), that distribute the blood to the brain and the upper limbs. The descending aorta branches, within the abdomen, into the two iliac arteries that provide blood to the lower limbs.

The aortic diameter decreases with the distance from the aortic root; specifically, the normal diameter of the AA is $<2.1 \text{ cm/m}^2$ while, that of descending aorta is $<1.6 \text{ cm/m}^2$ [3]. Thus, the AA has a diameter of 3.0 cm, the descending thoracic aorta of 2.5 cm and the abdominal aorta of 1.8-2.0 cm, approximately [4].

The arteries are generally subdivided in elastic and muscular; the arteries closest to the heart and with a large diameter (for example the aorta) are of elastic type while those located to the periphery are muscular. However, despite their subdivision, all the arteries have the same microscopic structure.

The aortic wall has three layers: the intima (tunica intima), media (tunica media) and adventitia (tunica externa).

- The tunica intima is the inner layer and consists of a layer of endothelial cells and a portion of connective tissue.
- The tunica media is the middle layer of the aortic wall; it is responsible for the aortic behavior; specifically, it consists of smooth muscle cells, connective tissue and elastic fibers. The elastic fibers accumulate energy during systole with aortic expansion and give back this energy during diastole with aortic contraction.
- The most external layer is the tunica adventitia that consists of connective tissue, nerves and nutrient vessel.

Copyright © The McGraw-Hill Companies, Inc. Permission required for reproduction or display.

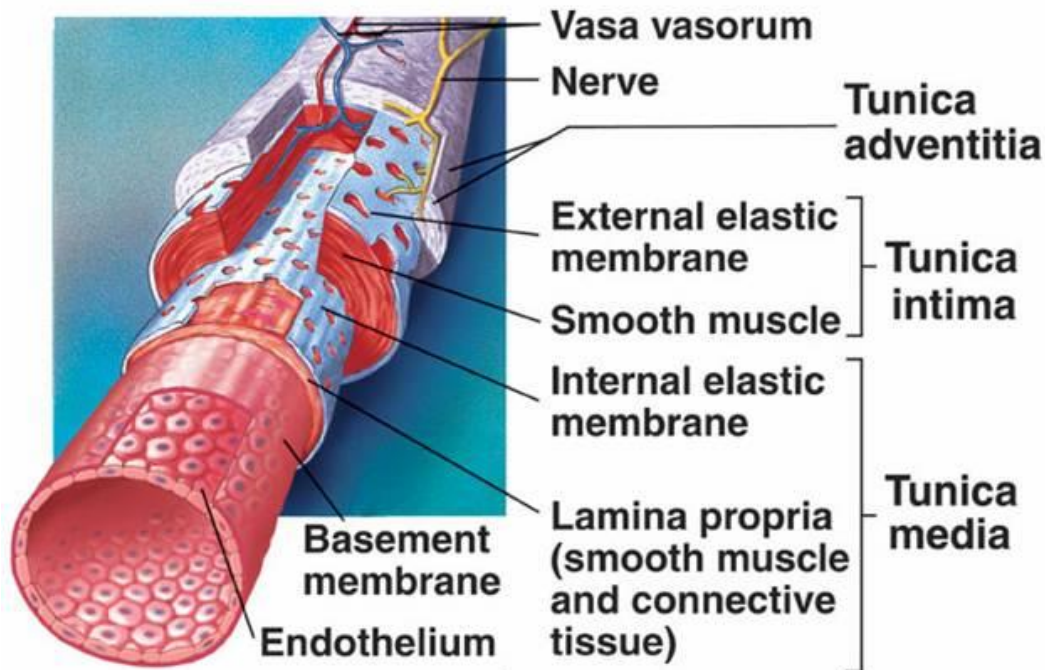


Figure 1.4 Representation of the main component of the arterial vessel wall

The aorta changes its dimension and mechanical properties with the ageing; specifically, aortic diameter increases while the aortic compliance decreases during patients' life. Loss in aortic wall compliance and increase in aortic wall stiffness lead to pulse pressure and pulse wave velocity raising with a consequent reduced perfusion of the peripheral organs[3].

1.3. Aortic Aneurysm

An aortic aneurysm is a permanent and localized dilatation of the aorta resulting in a 50% increase in diameter (ratio of observed to expected diameter ≥ 1.5).

The human artery most interested by aneurysms is the aorta due to its extension and its particular location, close to LV, that expose it to relevant pressure loads.

Aortic Aneurysms (AoAs) may be distinguished, on the base of their location, into abdominal aortic aneurysms (AAAs) and thoracic aortic aneurysms (TAAs). These two typologies of dilatations differ for their localization, morphology and rupture mechanism.

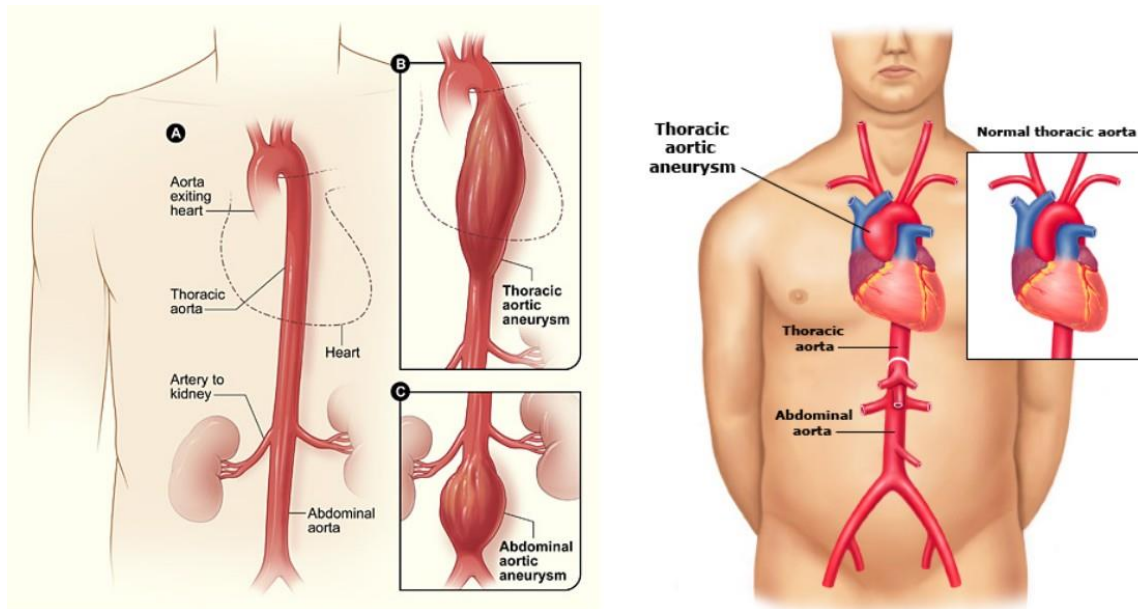


Figure 1.5 Representation of the various type of aortic aneurysm.

AoAs are managed pharmacologically or surgically based on their dimension and their risk of rupture or complications.

As basic approximation, it is possible to describe aorta as a thin-walled cylinder under pressure and thus describe the hoop stress created by an internal pressure with the Laplace law:

$$\sigma_{\theta} = \frac{P * r}{t} \quad \text{Eqn. 1.1}$$

Where P is the internal pressure, r is the aortic radius and t the aortic wall thickness. In this way, since the wall stress is proportional to aortic diameter, it is possible to confirm that the risk of aneurysm rupture increase with the aneurysm size.

1.3.1. Abdominal aortic aneurysms

AAA is an enlargement of the portion of aorta that extends into the abdomen. Most of AAAs are asymptomatic until their excessive dilatation or rupture.

An aortic dilatation may be connected to several causes but since only few AAAs are directly related to specific cause most aneurysms are classified as non-specific.

AAA incidence ranges between 1% and 3% of the population and is higher for male (i.e. 8-9%) if compared to female (i.e. 1-2.2%) patients[5]. Moreover, due to population ageing and increasing in screening programs, AAA incidence has increased in the last decades.

AAAs are usually treated, if un-ruptured, with elective surgical repair as soon as they reach a threshold diameter value else, if ruptured with emergency surgical repair. Pharmacologically management is indicated when the aneurysm growth rate and size do not exceed a threshold value.

1.3.2. Thoracic aortic aneurysm

Ascending thoracic aortic aneurysms (ATAAs) are the most common pathologies of the thoracic aorta and are mainly caused by the artery hardening. Some ATAAs are asymptomatic and growth slowly but as the aneurysm grows some people may experience back pain, cough, pain in the chest and shortness of breath.

Despite their low incidence (0.0059%) [6], ATAA are particularly lethal with an estimated mortality rate as high as 62% in patient with ATAA larger the 6 cm [7].

ATAAs are associated with several predisposing factors, such as the presence of a congenital defect like the bicuspid aortic valve (BAV), or the presence of connective tissue disorder such as Marfan or Ehlers syndrome.

The choice of the best treatment for ATAA is an ongoing debate since physician have to deal with the risk of leaving the aneurysm untreated and the risk connected to treat the aneurysms surgically. Elective surgical procedures are often contraindicated due to high risk connected to surgery and to patients' general condition; adversely, if left untreated, ATAAs may suddenly rupture or dissect leading to a mortality rate as high as 96%. Understanding when these complications may happen is the most critical part in the clinical decision process about elective surgical repair. Currently, the gold standard to evaluate the timing of operation for patients with ATAA is based on the maximum aortic diameter criterion suggested by Coady at al. [8]. This criterion prescribes that if

AoAs diameter is above 6 centimeter, for both ATAA and AAA, an elective surgical procedure should be operated. Clinical decision is also supported by the evaluation of aneurysm growth rate; it has been reported an average aneurysm growth of 0.1cm/year for TAAs, with an average of 0.19 cm/year for descending thoracic aortic aneurysms and 0.07 cm/year for ATAAs[9].

Despite diameter criterion is widely used in clinical practice worldwide, aneurysm rupture with a diameter value below 6 centimeter is not infrequent. Moreover, following the European guidelines, an ATAA associated with BAV should be replaced at 5.0 cm if ATAA growth more than 0.2 cm/year or in presence of risk factor like hypertension[9].

Della Corte et al. [10] proposed a classification scheme of the dilated aorta in which the aortas were divided on the base of their dilatation pattern (i.e. non-dilated, ascending phenotype and root phenotype). Another classification proposed by Schaefer et al. [11] classify the aorta in three groups (i.e. Type N, Type A and Type E) according to the commonly observed shapes of aortic dilatations.

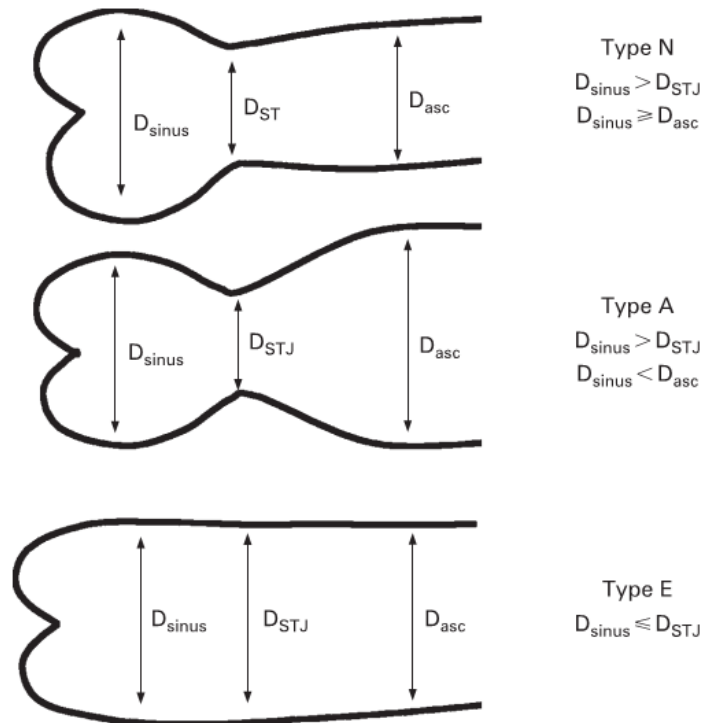


Figure 1.6 Schaeffer classification of aortic dilatation

Several attempts have been made to establish if the mechanism on the basis of ATAA is genetic or hemodynamic in origin. The genetics theory supports the idea that ATAA is a direct consequence of aortic wall weakness and that this weakness is due to abnormal regulatory pathways of extracellular matrix degeneration within the aortic media. This idea is supported by the observation that BAV and TAV had histological and molecular differences. On the other hand the hemodynamic theory is based on the idea that abnormal flows inside aorta, as those introduced by BAV, may impose high loads on aortic wall that promote the aneurysm generation and growth. This theory is supported by the observation that different phenotype of BAV lead to different aortic dimension. However, it is possible to speculate that both hemodynamic and genetic may be responsible for aneurysm growth.

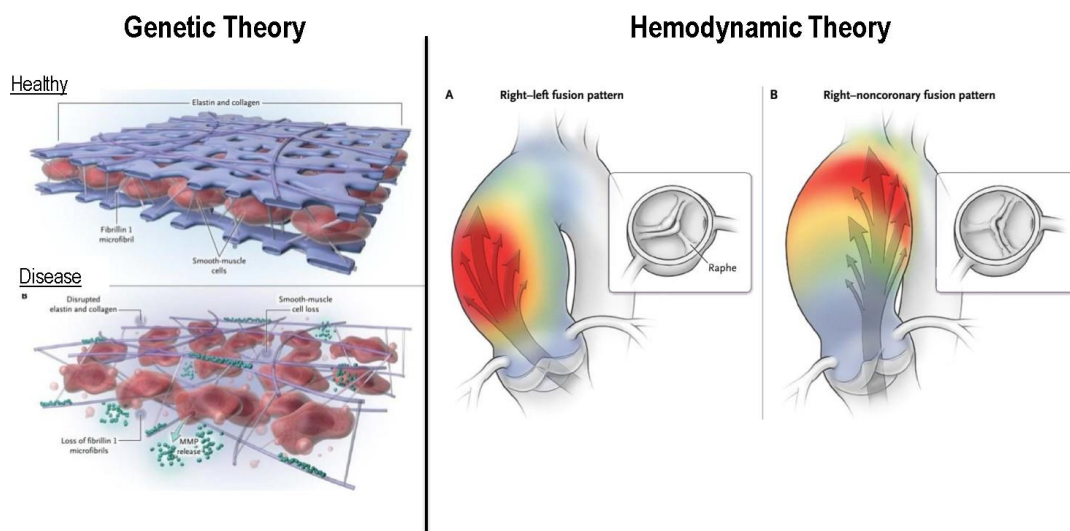


Figure 1.7 Representation of the genetic and hemodynamic theory on the basis of ascending thoracic aortic aneurysms [12]

1.4. Aortic dissection

Aortic dissection (AoD) originates from a tear in the intimal layer of the aortic wall that allows the blood to flow inside it and create a false lumen in the space previously occupied by the medial

layer. Thus, patients with AoD present a dual lumen, an original lumen (i.e. true lumen (TL)) and a pathological lumen (i.e. false lumen (FL)).

AoD, despite improvements in diagnosis and surgery, remains a challenging clinical emergency with high in-hospital and follow-up mortality rates.

Diagnosis of AoD is sometimes difficult and thus the actually reported incidence rates, 3-4 per 100000 persons per year, are probably underestimating the true phenomenon incidence. AoD is defined acute if the diagnosis is made within 2 weeks following the initial onset of symptoms, otherwise it is chronic [13].

Following the Stanford classification, an AoD is defined type A if it involves the ascending aorta while it is defined type B if originates distally to the left subclavian artery. Type B AoD, with a mortality rate as high as 25% within 30 days, has better survival rate than the type A AoD. Complications, related to AoD, are presents in 15-20% of the patients and refer to adverse events such as aortic dilatation prone to rupture or end-stage heart failure[14].



Figure 1.8 Representation of a patient chest with a type B aortic dissection starting from aortic arch up to the iliac trunk.

Patients with Stanford Type A AoD are treated with emergency surgical procedure due to high risk-related of rupture. Patients, surgically treated for type A AoD, may suffer for a residual type B AoD. Residual dissection is managed pharmacologically and monitored over time as a native type B AoD.

Management of patients with Stanford Type B AoD is more complex and challenging since different approaches are used on the base of patient clinical condition. Patients who have uncomplicated Stanford type B AoDs are treated pharmacologically using antihypertensive drugs and have a survival rate as high as 89%[15]. Surgical intervention is reserved for cases that are complicated by progression of dissection, rupture or impending rupture, refractory chest pain, or end-organ ischemia caused by compromised aortic branches [16-18]. Specifically, if aortic diameter is larger than 7 cm physician should propose an elective surgery[9]. In spite of a reduced in-hospital mortality, the long-term overall survival of patients with dissection is ranging from 50% to 80% at 5-years and from 30% to 60% at 10-years, with no differences between Type A and Type B AoDs [19, 20].

1.5. Bicuspid aortic valve

Normal tricuspid aortic valve has three cusps that, with their motion, allow the blood to flow from the LV to the aorta, during systole, and avoid the return of blood into the left ventricle, in diastole. Pathological valves have one or two cusps instead of the normal three due to problems during valvulogenesis.

BAV is the most common congenital heart[21] defect, presents in approximately 1-2% of the population[22]; it accounts for more morbidity and mortality than all other congenital cardiac malformations combined. Specifically, it is the result of the fusion of two adjacent cusps and for this, BAV has two unequal-sized leaflets. Cusps' fusion leads, most of the time, to the generation of a big leaflet with a central raphe.

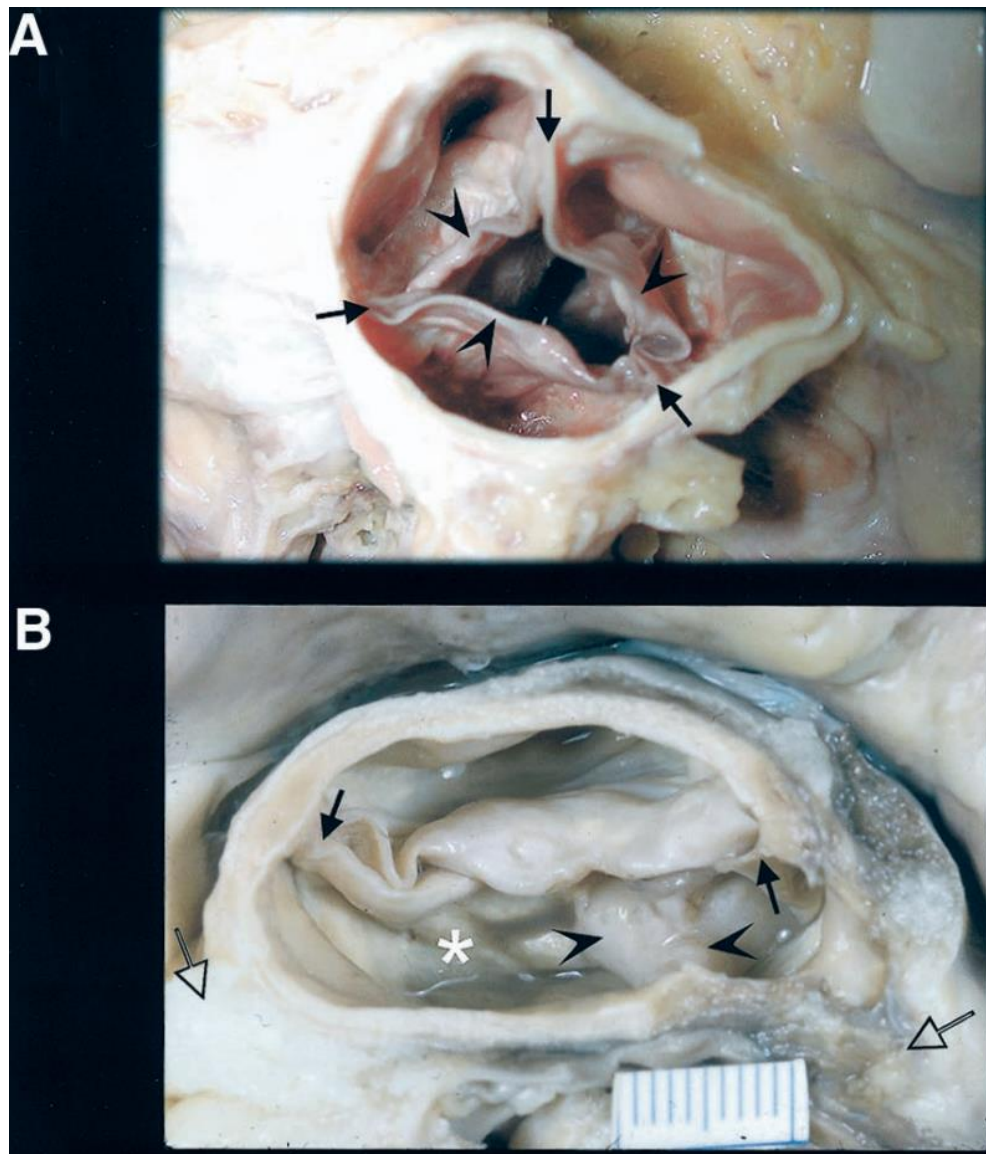


Figure 1.9: A) Normal tricuspid aortic valve; B) Congenitally bicuspid aortic valve

Several BAV phenotypes exist and they may be distinguished on the base of cusps and commissures fusion. Specifically, phenotype stratifications of BAV aortopathy have been proposed by Schaefer et al. [11] and by Kang et al.[23].

Schaefer classified BAV phenotypes into two groups, Type 1 and Type 2, on the base of the spatial position of the fused cusps.

In a different way Kang named the BAV phenotypes as right-left (RL) and anterior-posterior (AP); the AP phenotype is consequent to fusion of the right and left coronary cusps. The fusion of the

non-coronary cusp with one of the two coronary cusps generates a BAV named as RL from Kang. Thus, in this classification, types I and II represent AP BAV with or without raphe, respectively; types III, IV represent RL BAV with raphe and type V represents RL BAV without raphe.

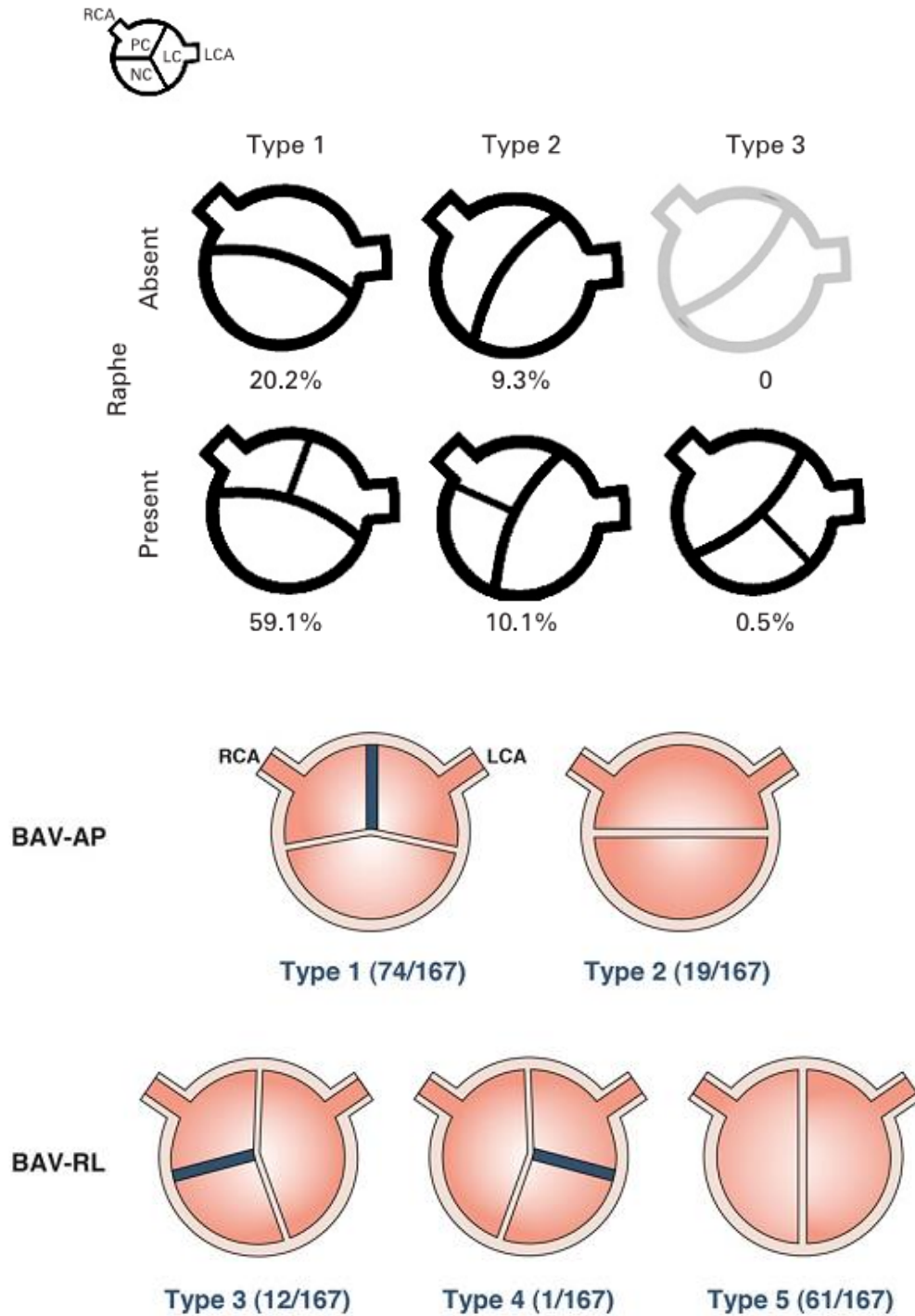


Figure 1.10: (A) BAV classification with Schaefer[11] indications. (B) Kang [23] BAV classification

A BAV may or not presents a raphe that is defined as the area of congenital leaflets fusion.

The most common phenotype is that with left and right cusps fusion [24].

BAV is frequently associated with several complications of which, one of the most common is the valve stenosis. Moreover, several studies have confirmed the correlation between BAV and ATAA[25] and it has been displayed that patient with BAV have 9-fold higher risk of AoD. Additionally, Phillippi et al.[26] observed a remarkable bimodal age distribution in ATAA population reporting a mean age of 51 years for BAV patients compared to a mean age of 68 years for patients with normal TAV.

References

1. Allender, S., et al., *European cardiovascular disease statistics*. 2008.
2. Ho, S.Y., *Structure and anatomy of the aortic root*. European Heart Journal-Cardiovascular Imaging, 2009. **10**(1): p. i3-i10.
3. Erbel, R. and H. Eggebrecht, *Aortic dimensions and the risk of dissection*. Heart, 2006. **92**(1): p. 137-142.
4. Bäck, M., et al., *Biomechanical factors in the biology of aortic wall and aortic valve diseases*. Cardiovascular research, 2013. **99**(2): p. 232-241.
5. Sakalihasan, N., R. Limet, and O. Defawe, *Abdominal aortic aneurysm*. The Lancet, 2005. **365**(9470): p. 1577-1589.
6. Vorp, D.A., et al., *Effect of aneurysm on the tensile strength and biomechanical behavior of the ascending thoracic aorta*. The Annals of thoracic surgery, 2003. **75**(4): p. 1210-1214.
7. JOYCE, J.W., et al., *Aneurysms of the Thoracic Aorta A Clinical Study with Special Reference to Prognosis*. Circulation, 1964. **29**(2): p. 176-181.
8. Coady, M.A., et al., *What is the appropriate size criterion for resection of thoracic aortic aneurysms?* The Journal of thoracic and cardiovascular surgery, 1997. **113**(3): p. 476-491.
9. Elefteriades, J.A., *Natural history of thoracic aortic aneurysms: indications for surgery, and surgical versus nonsurgical risks*. The Annals of thoracic surgery, 2002. **74**(5): p. S1877-S1880.
10. Della Corte, A., et al., *The ascending aorta with bicuspid aortic valve: a phenotypic classification with potential prognostic significance*. European Journal of Cardio-Thoracic Surgery, 2014. **46**(2): p. 240-247.
11. Schaefer, B.M., et al., *The bicuspid aortic valve: an integrated phenotypic classification of leaflet morphology and aortic root shape*. Heart, 2008. **94**(12): p. 1634-1638.
12. Verma, S. and S.C. Siu, *Aortic dilatation in patients with bicuspid aortic valve*. New England Journal of Medicine, 2014. **370**(20): p. 1920-1929.
13. Hebballi, R. and J. Swanevelder, *Diagnosis and management of aortic dissection*. Continuing Education in Anaesthesia, Critical Care & Pain, 2009. **9**(1): p. 14-18.

14. Tsai, T.T., et al., *Long-term survival in patients presenting with type A acute aortic dissection Insights from the International Registry of Acute Aortic Dissection (IRAD)*. *Circulation*, 2006. **114**(1 suppl): p. I-350-I-356.
15. Hagan, P.G., et al., *The International Registry of Acute Aortic Dissection (IRAD): new insights into an old disease*. *Jama*, 2000. **283**(7): p. 897-903.
16. Chang, C.-P., et al., *The role of false lumen size in prediction of in-hospital complications after acute type B aortic dissection*. *Journal of the American College of Cardiology*, 2008. **52**(14): p. 1170-1176.
17. Fann, J.I., et al., *Surgical management of aortic dissection during a 30-year period*. *Circulation*, 1995. **92**(9): p. 113-121.
18. Miller, D., et al., *Independent determinants of operative mortality for patients with aortic dissections*. *Circulation*, 1984. **70**(3 Pt 2): p. I153-64.
19. Yu, H.-Y., et al., *Late outcome of patients with aortic dissection: study of a national database*. *European journal of cardio-thoracic surgery*, 2004. **25**(5): p. 683-690.
20. Bernard, Y., et al., *False lumen patency as a predictor of late outcome in aortic dissection*. *The American journal of cardiology*, 2001. **87**(12): p. 1378-1382.
21. Ward, C., *Clinical significance of the bicuspid aortic valve*. *Heart*, 2000. **83**(1): p. 81-85.
22. Fedak, P.W., et al., *Clinical and pathophysiological implications of a bicuspid aortic valve*. *Circulation*, 2002. **106**(8): p. 900-904.
23. Kang, J.-W., et al., *Association between bicuspid aortic valve phenotype and patterns of valvular dysfunction and bicuspid aortopathy: comprehensive evaluation using MDCT and echocardiography*. *JACC: Cardiovascular Imaging*, 2013. **6**(2): p. 150-161.
24. Siu, S.C. and C.K. Silversides, *Bicuspid aortic valve disease*. *Journal of the American College of Cardiology*, 2010. **55**(25): p. 2789-2800.
25. Cripe, L., et al., *Bicuspid aortic valve is heritable*. *Journal of the American College of Cardiology*, 2004. **44**(1): p. 138-143.
26. Phillippi, J.A., S. Pasta, and D.A. Vorp, *Biomechanics and pathobiology of aortic aneurysms*, in *Biomechanics and Mechanobiology of Aneurysms*. 2011, Springer. p. 67-118.

Chapter 2

State of the art

2.1 Introduction

It has been proposed that the synergy of genetic and hemodynamic predisposing factors may stimulate the development of aortic dilatation (i.e. aneurysm), rupture or dissection. Thus, an in-deep knowledge of genetic and hemodynamic processes is fundamental to obtain a criterion for management of patients with aortic diseases that may substitute the actual criterion based on the measurement of the largest aortic diameter.

Aim of this thesis was to study the hemodynamic inside aorta and compare healthy patients with pathological ones. For this, all the technologies available to catch hemodynamic inside aorta were studied in order to evaluate which one was the most accurate and reliable. Moreover, the most used and accurate diagnostic tools were studied to evaluate which one was the most suitable for 3D aortic geometries reconstruction.

Among the several investigation methods used to study hemodynamic inside aorta, the 4D flow MRI and the computational modeling are the most used and appreciated while the standard 2D echocardiography combined with particle image velocimetry (PIV) is emerging as a novel non-invasive technique.

2.2. 4D flow MRI

4D flow MRI is an innovative, non-invasive technique for quantification of blood characteristics inside a chosen volume of control that gives good results when applied to thoracic aorta.

4D flow MRI allows visualizing the flow velocity field in a 3D fashion so that indirect estimations of hemodynamic parameters such as the WSS can be computed. Moreover, 4D flow MRI allows the visualization of normal aortic flow, with good agreement with the 2D and 3D phase-contrast, and abnormal secondary blood flow pattern [1].

Although 4D flow MRI has several positive aspects, the accuracy of WSS predictions from 4D flow MRI is strongly limited by a low spatial and temporal resolution of the order of 2 mm³ and 40 milliseconds, respectively. This results in an averaging of the measured velocity field, which negatively affects the calculated values of the velocity gradient at vessel edges and therefore the shear stress parameter.

In previous research studies, 4D flow MRI was applied to ATAAs to assess hemodynamic inside aneurysmal aorta; abnormally pronounced helical or vortical flow features were shown in patients with ATAA. Moreover, with 4D flow MRI, a relation between BAV and aortic dilatation was highlighted [2-4].

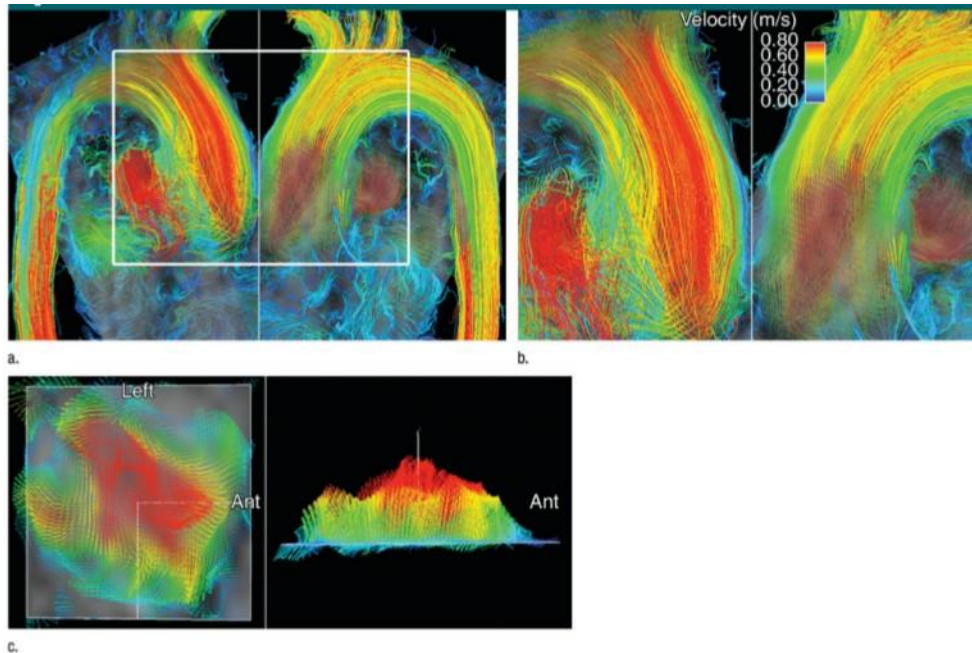


Figure 2.1: Systolic flow in a patient with a TAV obtained by four-dimensional flow MRI. [1] However, despite accordance in 4D flow MRI predicted hemodynamic and real hemodynamic, several studies demonstrated that absolute values of MRI-derived WSS are not trustworthy and that computational modelling is clearly advantageous for such investigations[2], [3]. It should be noticed that, standard 2D echocardiography combined with particle image velocimetry allows to rapidly estimating flow patterns and valvular diseases, in a less invasive and more reliable way than 4D flow MRI.

2.3. Computational modeling

Computational modeling has been widely applied in numerous fields of the engineering industries and, in the last decades, it has been applied to increase the knowledge about complex problems connected to cardiovascular diseases.

Computational modeling is based on the solution of complex fluid-dynamic or structural problems by discretize the region of interest in small elements, named finite element, on the vertices of which the local solution is calculated. The global solution is then calculated in the whole region of interest

by mean of interpolation of the results obtained in the local solution. Thus, it is possible to confirm that the solution obtained by applying the computational modeling is only an approximation of the real one and that the accuracy of this solution increases with the reduction of the small elements size.

Computational fluid dynamic analyses (CFD) are executed to study the fluid-dynamic inside a prefixed volume while structural analyses are executed to evaluate the stress and displacement system of a region of interest. At a higher degree of complexity, CFD and structural analyses are coupled to solve fluid-structural interaction analyses (FSI). The coupling between the CFD and the structural solvers is based on data exchange data over a fixed surface area. FSI analyses are more complex and time-consuming than simple CFD or structural analyses but the solutions obtained with FSI analyses are more accurate.

Computational modeling has been proposed as a valid tool to support physicians during their activities and to drive their decision-making process about which therapy or procedure propose for a specific patient. Moreover, computational modeling may be used in didactic tools like simulator to train young physicians.

CFD, structural and FSI analyses set up demand for a cluster of information containing data about geometries, material properties and other boundary conditions.

In the firsts biomechanical studies on cardiovascular apparatus or in general on human body the numerical simulations were quite basic; these firsts approaches used simple CFD or structural analyses in which the studied 3D geometries were merely simplifications of the real anatomies. For the specific case of an aortic aneurysm, the aortas were modeled as tubes with a curvature in proximity of the aortic arch while the aortic valve, most of the time, were not modeled at all.

In addition, the boundary conditions adopted were rough approximations of the real ones and the material properties defined had low accuracy (i.e. aortic wall modeled as single layer and with material behavior described by low accuracy constitutive models).

Nowadays, with advancements in technique, the computational analyses are executed on patient specific geometries reconstructed from diagnostic data and boundary condition; this analyses are more accurate and thus more useful for clinical use.

Patient specific geometries are reconstructed from patient computer tomography (CT) scans or magnetic resonance imaging (MRI) data, while boundary condition such as flow rate are collected from patient echocardiography data. Material properties (i.e. arterial wall material and blood properties) are described with validated, by mean of in vitro study, constitutive models.

2.3.1 Fluid-Structural Interaction

FSI analyses are multidisciplinary analyses involving both CFD and structural models to solve problems about the interaction between solid structures and moving fluids. A fluid in contact with a solid structure exerts, thanks to its pressure and velocity, forces on this structure and, as results of this interaction, the solid structure tends to deform. If the structural deformation is sensible, it may influence fluid behavior and pathway.

A deformable aorta with an internally flowing blood is the typical problem that could be studied with FSI analyses; in this situation, the aortic wall deformations and stresses are related to the pressure and the viscous fluid forces of the moving blood. In FSI applied to aorta, the CFD and the structural solvers exchange their solution over a shared surface that is the aortic wall.

In FSI analyses, data exchanges may be set both as unidirectional and as bidirectional. Bidirectional data exchanges are more complex and time-consuming than unidirectional ones but they are much more accurate; indeed, in particular cases in which bidirectional data transfer is too highly time-consuming, the unidirectional data transfer is used.

References

1. Hope, M.D., et al., *Bicuspid Aortic Valve: Four-dimensional MR Evaluation of Ascending Aortic Systolic Flow Patterns I*. *Radiology*, 2010. **255**(1): p. 53-61.
2. Papathanasopoulou, P., et al., *MRI measurement of time-resolved wall shear stress vectors in a carotid bifurcation model, and comparison with CFD predictions*. *Journal of Magnetic Resonance Imaging*, 2003. **17**(2): p. 153-162.
3. Markl, M., P.J. Kilner, and T. Ebbers, *Comprehensive 4D velocity mapping of the heart and great vessels by cardiovascular magnetic resonance*. *J Cardiovasc Magn Reson*, 2011. **13**(7): p. 10.1186.
4. <http://blog.image32.com/mri-vs-cat-scan/>. Available from: <http://blog.image32.com/mri-vs-cat-scan/>.

Chapter 3

Methodology

3.1. Introduction

The purpose of this work was to study, by application of experimental and numerical methods, CVDs with a particular focus on aortic pathologies. CFD analyses were executed to study hemodynamic variables inside aortas affected by aneurysm, dissection or with an implanted stent; moreover, structural analyses were performed to assess aortic wall displacements and stresses. At a higher degree of complexity, CFD and structural analyses were coupled in FSI analyses. Thus, case by case, on the base of the variable of interest, it was chosen to execute a simple CFD or a more complex FSI analysis.

Patient specific geometries are reconstructed from patient CT scans or MRI data, while boundary condition such as flow rate are collected from patient echocardiography data. Material properties (i.e. arterial wall material and blood properties) are described with validated constitutive models.

3.2. Fluid-Structural Interaction

In this thesis, parallel-coupled two-way FSI analyses were performed using the commercial software MpCCI v4.2 (Fraunhofer SCAI, Germany); this software is used to exchange data between the meshes of several simulation codes in the coupling region. More in detail, for the purpose of this research, MpCCI was used to couple the structural solver, ABAQUS v6.12 (SIMULIA Inc., Providence, RI), and the fluid solver, FLUENT v14.0.0 (ANSYS Inc., Canonsburg, PA).

MpCCI coupled the CFD and the structural solver, with the identification of the aortic wall as common boundary surface. The MpCCI algorithm, which allows for non-matching meshes, identifies nodes or elements near each other based on an association scheme, and data are then transferred from one node to the other (Fraunhofer, 2008) [1, 2, 4, 5].

MpCCI offer three possibilities for data transfer between the coupled codes:

- 1) Both codes exchange before iteration. The data are transferred immediately before the first solution step and after at every following step
- 2) Codes exchange after the iteration. In this case, the data are transferred only after the first solution step.
- 3) One code exchanges before iteration and the other after. This combination lead to a wide variety of algorithms but only few of them are eligible to perform FSI analyses.

a) Both codes exchange before iteration

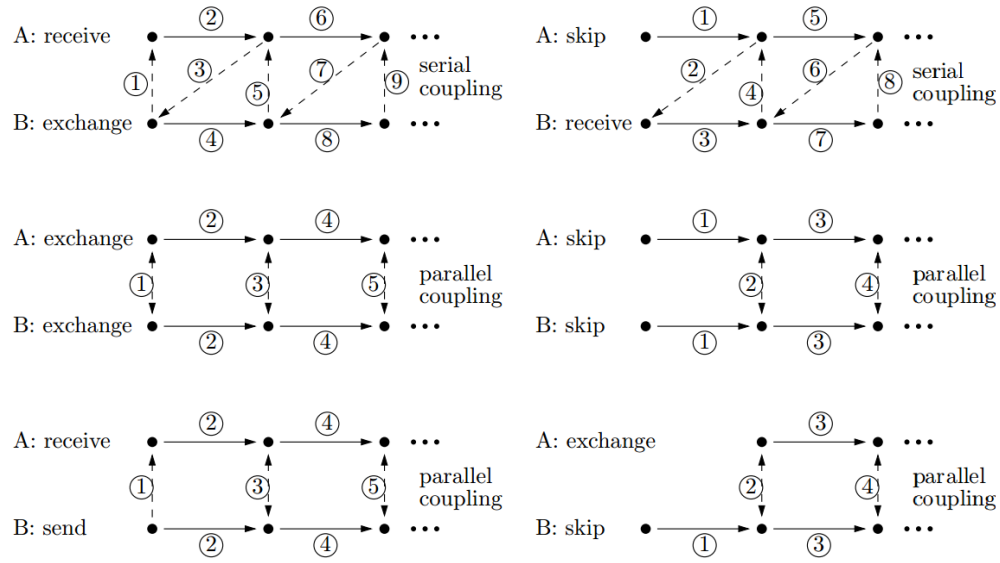


Figure 3.1: MpCCI coupling schemes with CFD and structural code exchange before iteration.

b) Both codes exchange after iteration

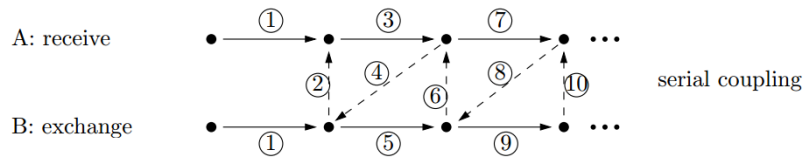


Figure 3.2: MpCCI coupling schemes with CFD and structural code exchange after iteration.

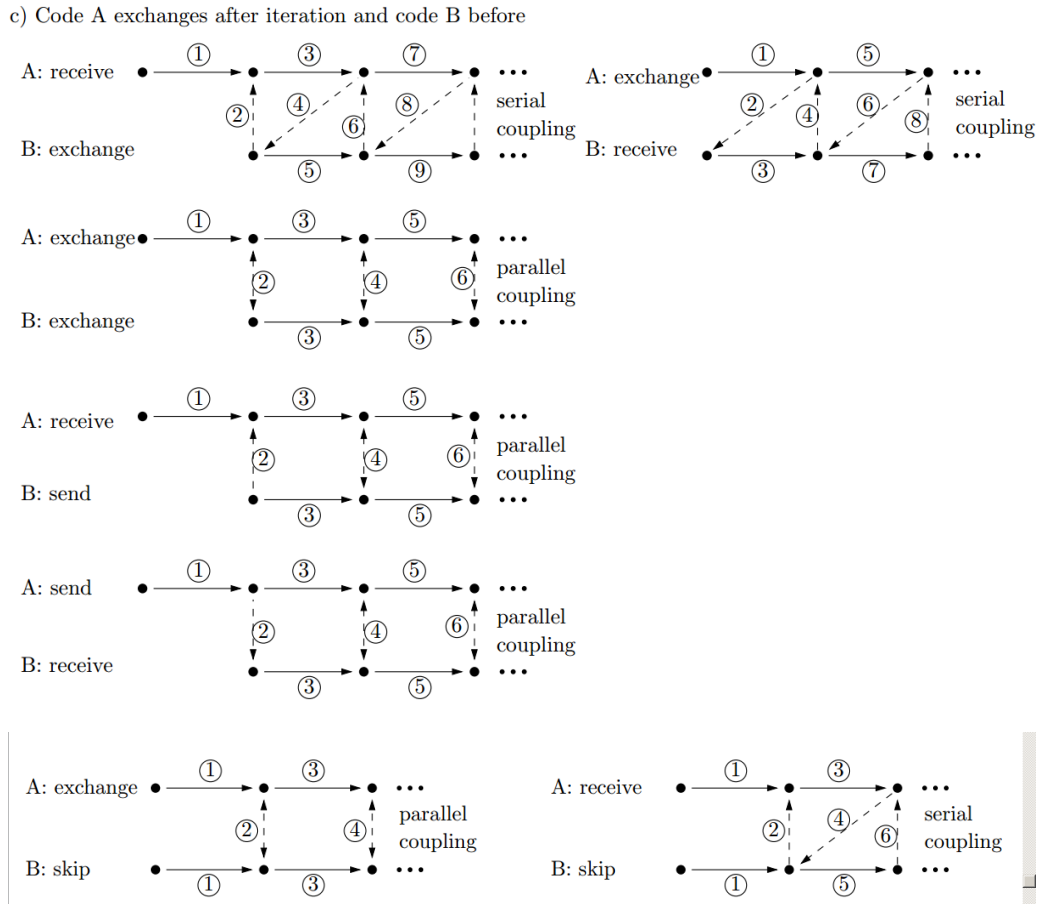


Figure 3.3: MpCCI coupling schemes with CFD and structural code exchange alternatively one after and one before iteration.

In order to execute the analyses, it is important to select one of the proposed data transfer models and impose the time step that define the frequency of the data exchange between the two solvers. All the analyses, executed during this research work, used a parallel coupling scheme (i.e. skip-skip scheme) in which both of the solvers exchange data before every iteration (see figure A). The time step chosen was selected in accordance with cardiac cycle total time.

3.3. Geometry Reconstruction

Computational analyses were executed on patient specific aortic geometries reconstructed from Electrocardiogram (ECG)-gated computed tomography angiography (CTA). The patients' scans

were taken from the radiologic records of our local hospital, the Mediterranean Institute for Transplant and Advanced Specialized Therapies (IsMeTT), after local research ethics committee's approval. The patients involved into these studies were informed and were asked for their informed consent.

ECG-gated CTA scans were retro-reconstructed, with specific software, to obtain images at cardiac phase with the largest orifice area of the aortic valve, if needed, which frequently occurs at 50-100 milliseconds after the R peak.

3.3.1. Image Acquisition: Computer Tomography

A CT is an imaging technique that combines multiple X-ray images, from different angulation, to produce picture of the many structures inside the human body, including internal organs, bones and vessels. The final data obtained is a cluster of bi-dimensional images of the three human body views (i.e. sagittal, coronal and axial plane).

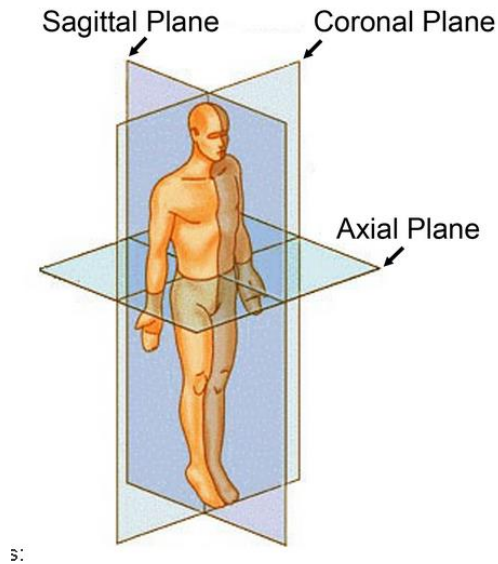


Figure 3.4: Three planes of the human body [4]

The CT is executed with a CT scanner that consists of an X-ray source that emit a narrow beam, and a group of detectors that receive the attenuated rays. Since their first appearance, CT scans have been developed throughout four generations; nowadays, the most used scans are those of the

third and fourth generations. Third generation scans have rotating X-ray tube and receptors while the fourth generation scans present a rotating X-rays tube and a stationary array of detectors.

A process of CT image acquisition goes through a first phase of X-rays attenuation record and a second phase of data elaboration. In the acquisition phase, the patient lie on a flat examination bed and the X-ray tube rotates around him perpendicularly to his length-axis; the X-ray tube emits a fan-shaped beam that pass the patient body and hit the receptors. In the elaboration phase, the data acquired by the receptors are sent in to a computer that mathematically reconstruct the data and produce a map of the attenuation coefficient μ .

This imaging method measures the attenuation of the X-rays intensity traversing the patient; the attenuated intensity is equal to $I=I_0*e^{-\mu x}$, where I_0 is the emitted ray intensity, x the length of the ray pathway and μ the linear attenuation coefficient. The latter is dependent from the beam energy and the density of the encountered material.

3.3.2. Image Reconstruction: Segmentation and 3D model

CT scans are a group of planar images with grayscale information that, in order to be used in a finite element analysis, need to be translated into a three-dimensional model. Each image pixel has its own grayscale value that, as previously described, is strictly related to material density.

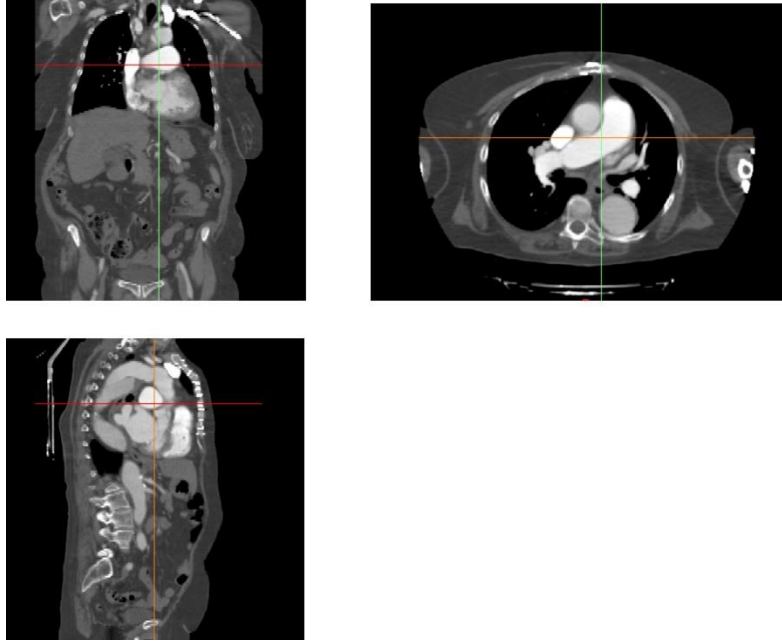


Figure 3.5 CT image with the three view (i.e. sagittal, axial and coronal plane) of a patient with type B aortic dissection

Several commercial software allow the final user to import images in .dicom format, standard file extension for CT scans, and, after a reconstruction process, to export it in 3D format (.stl, .step), standard file extensions for modelling or finite element software.

The first step followed in the reconstruction process of .dicom images was the image segmentation to highlight the region of interest, the aorta in the specific case of this work; the image segmentation is defined as that process of partitioning an image in multiple regions in order to point out the region of interest. Segmentation process proposed by commercial software were applied both automatically and manually. Both manual and automatic segmentation procedures have positive and negative aspect and in order to fully reconstruct a model it is important to use both of them. Indeed, manual segmentation is a time consuming procedure but if compared to automatic segmentation it is more accurate. Thus, automatic segmentation is used as first step of image reconstruction to reduce the region of interest while manual segmentation is used as second step to eliminate all the erroneously selected or unselected area from automatic segmentation.

The most used and useful automatic segmentation operation is the thresholding; in this operation, we set a range of grayscale values that delimitates the pixels to be taken into account during automatic segmentation.

After thresholding procedure, other additional tools were used to increase the accuracy of the final geometry. The final product of the reconstruction procedure is a three-dimensional geometry of the requested organ.

3.4. Geometry discretization

Finite element/volume methods are numerical techniques for the approximate solution of partial differential equations.

Finite element/volume methods are based on the discretization of the region of interests in small surface/volume elements, which form a mesh, whose vertices, called nodes, are the points where the solution is computed. The kind of these small elements, their shape and dimension strongly influence the analysis convergence and solution quality. Additionally, as higher is the number of elements as closer will be the discretized domain to the continuous domain, with a consequently more accurate solution. Adversely, at higher number of elements corresponds higher computational resources and time; for this, during the discretization process it is necessary to mediate between solution accuracy and computational time by choosing the appropriate number and type of elements that constitute a mesh.

For the purpose of this research, the 3D aortic models reconstructed from patient CT scans were imported, in .iges format in GAMBIT 2.3.6 (ANSYS Inc., Canonsburg, PA). GAMBIT is a commercial software tool developed to discretize lines, areas and volumes in small finite element.

In this work, for each patients, two different meshes were realized; one of these was used to solve CFD analyses and the other to solve structural analyses. The CFD mesh is related to the lumen of the aorta while the structural mesh is related only to the aortic wall.

The CFD mesh was generated by discretizing the volume of interest in~1 million unstructured tetrahedral elements. More in detail, TGrid Meshing Scheme was used; with this scheme, Gambit attempts to create a mesh with only tetrahedral elements but if it is necessary uses also hexahedral, pyramidal and wedge elements. Pyramidal elements are mainly used near pre-meshed faces while

hexahedral and wedge elements in proximity of boundary layers. After mesh generation, with check of volume mesh it is possible to visualize the number of mesh elements and the 3D mesh quality and in case optimize the obtained mesh. The final output file is an .msh file that contains all the information about the discretization and that is ready to be imported into a numerical analysis software.

To achieve good convergence in CFD simulations, mesh quality checks were performed using grid convergence index (GCI)[4].

3.5. Computational fluid dynamics analysis

Fluid flow is governed by conservation of mass, momentum and energy partial differential equations. For most engineering problems, the analytical solution of the abovementioned differential equations is almost impossible and thus their solution is obtained, with an approximate solution, by the application of CFD solver.

In the CFD approach the continuous real domain volume is discretized in an approximate discrete domain with small volume elements whose vertices form a grid of points inside the domain; the solution, velocity vectors and pressure values, is obtained only in the points of the grid. The variable values in all other points of the domain are computed interpolating the values obtained in the grid point. In this project, CFD was applied to aortic pathologies and for this, we used patient specific geometries reconstructed from patient radiographic data.

3.5.1. CFD preprocessing

Fluid dynamic inside aortas was evaluated by steady and unsteady CFD simulations, which were performed using FLUENT v13.0.0 (ANSYS Inc., Canonsburg, PA).

The computational approach was based on an experimentally-validated second-order algorithm, which was developed to resolve specifically high-frequency, time-dependent flow instabilities encountered in complex cardiovascular anatomies [5, 6].

The blood flow was assumed incompressible and Newtonian with a density of 1060 kg/m^3 and viscosity of $3.71 \times 10^{-3} \text{ Pa} \cdot \text{s}$; this viscosity value corresponds to hematocrit level equal to 40%. Blood could be assumed as Newtonian fluid when the shear rate is above a threshold value. In many studies, the shear rate threshold value was proposed in the range between 50 s^{-1} and 300 s^{-1} [7],[8]. A Newtonian fluid has a viscosity independent from the shear stress at a fixed temperature. Newton law expresses a linear relationship between viscous stress and strain rate:

$$\tau = \mu \frac{du}{dy} \quad \text{Eqn. 2.1}$$

Where μ is the constant fluid viscosity.

The assumption of Newtonian fluid for blood with a constant viscosity is feasible in large vessels [9]. Although several works such as Khanfar et al.[10] shown that the non-Newtonian assumption of blood affects the blood flow in the thoracic aorta, their simulations did not display significant differences in WSS calculated with simulations with Newtonian and non-Newtonian. Moreover, since blood, even in the same patient, changes its characteristics depending on several factors, even assuming blood as non-Newtonian would have introduced a certain amount of approximation.

A pressure-velocity coupling algorithm was used as solution method. Specifically, a pressure-implicit with splitting of operators (PISO) and skewness correction was used as pressure-velocity coupling algorithm to improve the convergence of the transient calculations in close proximity of distorted cells. The PISO algorithm is highly recommended for transient flow calculation since it can maintain stable calculation even with large time step and under-relaxation factors of 1.0 for momentum and pressure. In a similar way, in steady state simulation, the PISO algorithm with skewness correction is recommended since it reduces the effect of element with high degree of distortion.

2nd order upwind scheme was applied to discretize the convective terms in momentum equations in order to eliminate numerical diffusion in calculations. Pressure staggering option (PRESTO) scheme as pressure interpolation method was set with 2nd order accurate discretization. 1st order accuracy is acceptable for laminar flow in a quadrilateral or hexahedral grid with flow aligned with

the grid; in CFD study of the aorta where the grid is tetrahedral the flow is never aligned with the grid and thus a more accurate results is obtained by using a 2nd order discretization. Sometimes, it is necessary to start the analysis with a 1st order scheme, to have the first initial values and then, after few iterations, switch to 2nd order to achieve the most accurate results. Convergence was enforced reducing the residual of the continuity equation by 10^{-7} at all-time steps.

In this thesis, boundary conditions were imposed as:

- Velocity inlet at aortic root region in order to obtain the total cardiac output. Depending on the analysis typology, the velocity inlet imposed had a steady value or a pulsatile flow waveform that consisted of ten points. In steady simulation, the velocity inlet imposed was an average of the velocities calculated in the whole cardiac cycle while in the unsteady analyses the 10 velocities, one for each cardiac cycle point, were imposed as the real velocities calculated at that time in a patient cardiac cycle. Specifically, the inflow aortic profile presented a fundamental frequency of 1 Hz as we performed in previous works[11, 12]. In both cases, the imposed cardiac output is equal to 5 LPM.
- Cardiac output was split between the outflow area by mean of resistance applied to the supra-aortic vessels and abdominal aorta; more in detail, 80% of the whole cardiac output was diverted into the abdominal aorta and 20% into the supra-aortic vessels. In the supra-aortic vessel, 10% of the blood flow through the brachiocephalic trunk, 4% through the left common carotid artery and 6% through the left subclavian artery as it used in a similar study [13].

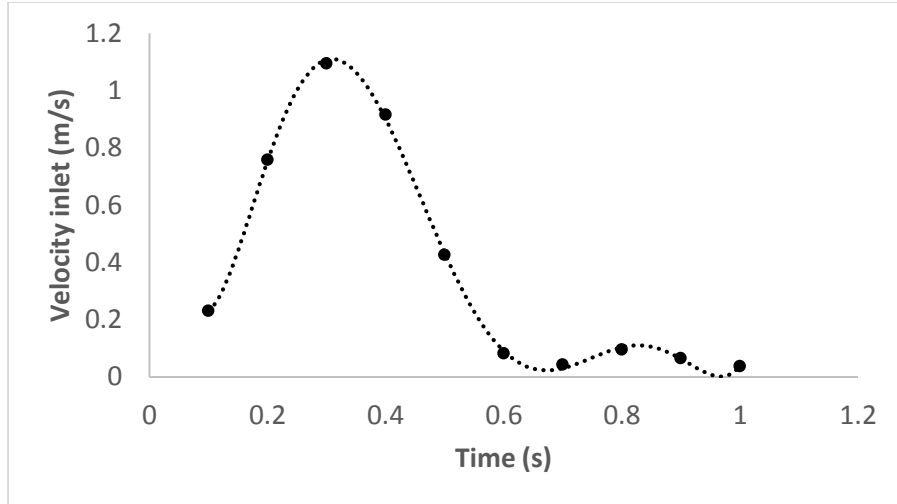


Figure 3.6 Velocity inlet profile imposed as boundary condition for unsteady CFD simulation at the aortic valve region.

In unsteady analyses, steady state solutions were used to initialize the flow field prior to the transient analyses. To address the numerical stability problems, related to the high systemic resistances of multi-outlet aortic anatomy (i.e., since even the minute flow rate adjustments are transferred as large pressure oscillations in 3D domain), an iterative under-relaxation-based resistance boundary condition was coupled to each outlet [6]. At each inner iteration, the pressure gradient calculated at the outlets was attenuated ten times to ensure smoother convergence. Each downstream resistance was coupled to the solver iteratively to prevent divergence due to multiple outlets.

Unsteady simulations were continued through three cardiac cycles to eliminate nonlinear start-up effects, and results presented here were obtained at the last cycle.

During post-processing operations, several parameters such as velocity vectors, fluid pressure, wall shear stress (WSS), time-average WSS and Oscillatory Shear Index (OSI) were studied. The OSI is a parameter that allows monitoring the WSS changes in direction and magnitude over a cardiac cycle.

Specifically, the time-averaged WSS magnitude was defined as[14]:

$$\tau_w = \frac{1}{T} \int_0^T |\vec{t}_w| dt \quad \text{Eqn. 2.2}$$

Where $|\vec{t}_W|$ is the magnitude of wall shear stress vector, \vec{t}_W , and T is the duration of one cardiac cycle. The OSI was defined as [14]:

$$OSI = \frac{1}{2} \left(1 - \frac{\int_0^T \vec{t}_W dt}{\int_0^T |\vec{t}_W| dt} \right) \quad \text{Eqn. 2.3}$$

OSI value ranges between 0.0 and 0.5, with 0.0 corresponding to unidirectional flow and 0.5 to highly pulsated flow.

3.6. Structural Model

Mechanical response of aorta was evaluated with finite element analyses executed on ABAQUS FE code (Simulia, Inc., Providence, RI). FEM substitutes to the real structures an approximate structure made by small elements namely finite elements; as high the number of finite elements is as more accurate the analysis result is.

As previously described, finite element software tools request, in order to execute the analyses, a cluster of information data about material properties of the studied object, boundary condition (i.e. nodal load and degree of freedom), and analysis typology.

Aortic wall material could be modeled as an active or a passive material:

- Active aortic wall behavior is influenced by the properties and amount of elastin, collagen and by the contraction of smooth muscles.
- Passive aortic wall behavior is only influenced by elastin and collagen with no contribution of smooth muscles since their support to material properties is not known[15]. Most of the models actually used are passive and polynomial or exponential function.

Some constitutive models consider aortic wall as a single layer element and other as multiple layers. In general, the arterial behavior is described with a strain-energy function that usually is of

exponential type. The strain energy function mostly used to describe the aortic wall behavior is that proposed by Fung et al. [16] that has been reformulated several times and for different applications [15]. One of the most general Fung strain-energy function reformulation is that proposed by Humphrey [17], this formulation is three-dimensional:

$$\Psi = \frac{1}{2}c[e^Q - 1] \quad \text{Eqn. 2.4}$$

Where Ψ is the strain-energy, c is a material parameter and Q is given by:

$$Q = b_1 E_{\theta\theta}^2 + b_2 E_{ZZ}^2 + b_3 E_{RR}^2 + 2b_4 E_{\theta\theta} E_{ZZ} + 2b_5 E_{ZZ} E_{RR} + 2b_6 E_{RR} E_{\theta\theta} + b_7 E_{\theta Z}^2 + b_8 E_{RZ}^2 + b_9 E_{R\theta}^2 \quad \text{Eqn. 2.5}$$

Where b_i ($i=1, \dots, 9$) are non-dimensional parameters, E_{ij} are the component of the modified Green-Lagrange strain tensor that refer to a cylindrical coordinate system.

The strain-energy function proposed above is three-dimensional but, in the common practice a less complex equation is used; this simplify equation is a bi-dimensional strain-energy function that depends only from $E_{\theta\theta}$, E_{ZZ} and $E_{\theta Z}$. Thus, the two-dimensional strain-energy function proposed by Fung et al. has the following form:

$$\Psi = \frac{1}{2}c[e^Q - 1] \quad \text{Eqn. 2.6}$$

With Q equal to:

$$Q = b_1 E_{\theta\theta}^2 + b_2 E_{ZZ}^2 + 2b_4 E_{\theta\theta} E_{ZZ} \quad \text{Eqn. 2.7}$$

Raghavan et al. [18] proposed a constitutive theory that models the non-linear behavior of the AAA wall with an homogenous, isotropic and incompressible strain energy function. On the base of the finite elasticity, the strain energy proposed was related to the Left Cauchy-Green tensor (B) and its first and second invariants (I_b and II_b):

$$W = W [I_b, II_b] \quad \text{Eqn. 2.8}$$

Where W is the strain energy density.

The final formulation of this strain energy function is:

$$W = \alpha(I_b - 3) + \beta(I_b - 3)^2 \quad \text{Eqn. 2.9}$$

Where α and β are two model parameters describing the mechanical properties of the aneurysmal wall.

All the models presented above are based on the matching of experimental data with the constitutive equation by mean of material parameters. However, this approach, namely phenomenological, describes only the general macroscopic mechanical response of the arterial wall to sollicitation but it is not able to describe the relation between deformation mechanism and arterial wall architecture. Thus, histological approach, in which aortic wall is described as a multi-layer material has been proposed; each layer was described as a fiber-reinforced composite obtaining a material description that considers the histologic structure of the wall material. Moreover, it is possible to confirm that, a more realistic constitutive model, as the fiber-reinforced model, is an important step to assess changes in biological tissue structure and function as response to external loads [19]. Gasser and collaborators [19], proposed a fiber-reinforced constitutive model that adopted the strain energy function:

$$W = \frac{C}{2}(I_1 - 3) + \frac{k_1}{k_2} \{ \exp[k_2(kI_1 + (1 - 3k)I_{4i} - 1)^2] - 1 \} \quad \text{Eqn. 2.10}$$

Where k_1 , k_2 and C were the material parameters and k was a structural parameter.

The first invariant of the right Cauchy-Green strain tensor was:

$$I_1 = \lambda_{\text{circ}}^2 + \lambda_{\text{long}}^2 + (\lambda_{\text{circ}}\lambda_{\text{long}})^2 \quad \text{Eqn. 2.11}$$

The tensor invariant was:

$$I_{41} = I_{42} = \lambda_{\text{circ}}^2 \sin^2 \gamma + \lambda_{\text{long}}^2 \cos^2 \gamma \quad \text{Eqn. 2.12}$$

Where γ was a material parameter.

For structural analyses, aortic wall was modeled as a bi-layered hyper-elastic (i.e. tunica intima with portion of delaminated media and tunica adventitia with portion of delaminated media) element.

References

1. Rudski, L.G., et al., *Guidelines for the Echocardiographic Assessment of the Right Heart in Adults: A Report from the American Society of Echocardiography: Endorsed by the European Association of Echocardiography, a registered branch of the European Society of Cardiology, and the Canadian Society of Echocardiography*. Journal of the American Society of Echocardiography : official publication of the American Society of Echocardiography, 2010. **23**(7): p. 685-713.
2. Fraunhofer, *SCAI MpCCI Documentation 2008*. Sankt Augustin, Germany.
3. <http://blog.image32.com/mri-vs-cat-scan/>. Available from: <http://blog.image32.com/mri-vs-cat-scan/>.
4. Celik, I.B., U. Ghia, and P.J. Roache, *Procedure for estimation and reporting of uncertainty due to discretization in {CFD} applications*. Journal of fluids {Engineering-Transactions} of the {ASME}, 2008. **130**(7).
5. Pekkan, K., et al., *Neonatal aortic arch hemodynamics and perfusion during cardiopulmonary bypass*. Journal of biomechanical engineering, 2008. **130**(6): p. 061012.
6. Dur, O., et al., *Computer-aided patient-specific coronary artery graft design improvements using CFD coupled shape optimizer*. Cardiovascular engineering and technology, 2011. **2**(1): p. 35-47.
7. Long, D.S., et al., *Microviscometry reveals reduced blood viscosity and altered shear rate and shear stress profiles in microvessels after hemodilution*. Proceedings of the National Academy of Sciences of the United States of America, 2004. **101**(27): p. 10060-10065.
8. Chan, W., Y. Ding, and J. Tu, *Modeling of non-Newtonian blood flow through a stenosed artery incorporating fluid-structure interaction*. Anziam Journal, 2007. **47**: p. 507-523.
9. Lee, S.-W. and D.A. Steinman, *On the relative importance of rheology for image-based CFD models of the carotid bifurcation*. Journal of biomechanical engineering, 2007. **129**(2): p. 273-278.
10. Khanafer, K.M., et al., *Modeling pulsatile flow in aortic aneurysms: effect of non-Newtonian properties of blood*. Biorheology, 2005. **43**(5): p. 661-679.

11. Dur, O., et al., *Optimization of inflow waveform phase-difference for minimized total cavopulmonary power loss*. Journal of biomechanical engineering, 2010. **132**(3): p. 031012.
12. Pasta, S., et al., *Computer modeling for the prediction of thoracic aortic stent graft collapse*. Journal of vascular surgery, 2013. **57**(5): p. 1353-1361.
13. D'Ancona, G., et al., *Haemodynamic predictors of a penetrating atherosclerotic ulcer rupture using fluid–structure interaction analysis*. Interactive cardiovascular and thoracic surgery, 2013. **17**(3): p. 576-578.
14. He, X. and D.N. Ku, *Pulsatile flow in the human left coronary artery bifurcation: average conditions*. Journal of biomechanical engineering, 1996. **118**(1): p. 74-82.
15. Holzapfel, G.A., T.C. Gasser, and R.W. Ogden, *A new constitutive framework for arterial wall mechanics and a comparative study of material models*. Journal of elasticity and the physical science of solids, 2000. **61**(1-3): p. 1-48.
16. Fung, Y., K. Fronek, and P. Patitucci, *Pseudoelasticity of arteries and the choice of its mathematical expression*. American Journal of Physiology-Heart and Circulatory Physiology, 1979. **237**(5): p. H620-H631.
17. Humphrey, J.D., *Mechanics of the arterial wall: review and directions*. Critical reviews in biomedical engineering, 1994. **23**(1-2): p. 1-162.
18. Raghavan, M. and D.A. Vorp, *Toward a biomechanical tool to evaluate rupture potential of abdominal aortic aneurysm: identification of a finite strain constitutive model and evaluation of its applicability*. Journal of biomechanics, 2000. **33**(4): p. 475-482.
19. Gasser, T.C., R.W. Ogden, and G.A. Holzapfel, *Hyperelastic modelling of arterial layers with distributed collagen fibre orientations*. Journal of the royal society interface, 2006. **3**(6): p. 15-35.

Chapter 4

FSI application to ATAA study

4.1 Introduction

The purpose of this research was to evaluate the presence of hemodynamic differences in patients with ATAAs. More in detail, the influence of BAV on ATAAs growth was assessed by comparison of the hemodynamic related to BAV and TAV patients.

This work is part of a wider program that aims to improve the actual clinicians' decision-making process about patient with ATAA. Specifically, the actual criterion adopted by the physician to evaluate the most appropriate procedure to follow for a specific patient with ATAA is based on the evaluation of the patients' clinical situation and on the maximum aortic diameter criterion. The general indication is that a patient with an aortic diameter larger than 6.0 cm needs to be threatened

surgically, while patients with aortic diameter smaller than the above mentioned threshold value may be managed with a pharmacologically therapy and be subjected to a specific follow up path. The biggest issue with this criterion is that it has failed numerous time as described by McGloughlin at al. [1]. For this, the main goal of the work is to apply FSI analyses on ATAA geometries to evaluate the presence of some particular values able to highlight and thus foresee the risk for an imminent aortic wall rupture. Starting from this generic purpose and from the observation of a strong correlation [2, 3] between ATAA formation and BAV presence we proposed to study the influence of BAV in ATAA formation and growth.

The most relevant theory about BAV and ATAA suggests that this correlation has a genetic cause in origin; however, it has been shown that hemodynamic flow inside ATAAs with BAV has different characteristics if compared to the flow observed in ATAAs with TAV. For this, the basic hypothesis of this study was that the particular flow pattern in ATAAs with BAV may contribute to increase shear forces on aortic wall, resulting in inhibition of the vascular remodeling process. Moreover, several in-vitro studies demonstrated that altered wall shear stress (WSS) and temporal WSS oscillations (i.e., the oscillatory shear index (OSI)) impact the endothelial cell function, including migration, proliferation and activation of transcription factors[4, 5]. Thus, the synergy of these factors with the elevated wall stresses connected to hemodynamic disturbances may lead to proximal dilatation of the AA.

The computational FSI analyses, that merge the advantages of structural and CFD analyses, allow evaluating, simultaneously, the relevant hemodynamic and mechanical forces specific of the mechanics of ATAAs. In this way, it is possible to obtain a more accurate evaluation of the patient clinical situation and gives, to the physicians, a more accurate tool to decide which procedure apply for a specific patient.

FSI has already been applied in several patient-specific simulations to study aortic aneurysms[6],[7] with interesting results and showing a high reliability.

The application of FSI has advantages if compared to other procedure actually used in clinical practice. As example, FSI results better than 4D flow MRI since it allows to direct calculate

preeminent hemodynamic predictors such as the WSS and blood pressure, which are instead impossible to evaluate with 4D flow MRI.

4.2 Method

The FSI analyses were executed on 3D model geometries reconstructed from patients who underwent ECG-gated computed tomography angiography (CTA) scans at ISMETT. We segmented three ATAAs geometries of patients with TAV and two with BAV. The reconstruction included the aortic valve completely opened, the ascending aorta, the aortic arch with the supra-aortic vessels and the descending aorta.

After geometry reconstruction, the .iges geometries were imported into gambit to generate two separate meshes, one for fluid and one for structural analyses.

FSI analyses were executed with a total analysis time of 0.68 s divided into 100 time step of 0.0068 s in order to complete an entire cardiac cycle; data exchange between the two computational solvers were imposed every time step.

For the structural solution, aortic wall was modeled as a two layers element since, after dissection, the aortic wall is divided into an inner section (intima and dissected media) and an outer section (dissected media and adventitia). Wall thickness was imposed to 1.7 mm (i.e. 1 mm for outer layer and 0.7 mm for inner layer), as measured experimentally[7]; moreover, aortic wall material was modeled as hyperelastic, incompressible and isotropic, whose mechanical properties were derived from previously published experimental data [7].

As boundary conditions, the distal regions of supra-aortic vessels, the aortic valve and descending aorta were fixed in all directions; in this way, the aortic was forced to deform in physiological way. The aortic valve leaflets were modeled as rigid without the possibility to move during the deformation process.

In the CFD model, the cardiac output (i.e. aortic inlet flow rate) was imposed constant at 5 L/min and was distributed between the aortic outlet, supra-aortic vessels and descending aorta, with a ratio of 40/60. On the base of these assumptions, inlet aortic flow velocity and pressure boundary conditions were calculated at inlet and outlets, which were also extended six diameters normal to the vessel cross section. Specifically, velocity boundary condition were set using user define function (UDF) in which the flow rate was calculated as proportional to vascular resistance and differential pressure between the vessels and the right atrium.

Following delamination of ATAA tissue samples, tensile tests on the delaminated halves were performed to evaluate the elastic stress-stretch response of the outer (adventitia and dissected media) and inner (intima and dissected media) layers of the dissected aortic wall. Thus, the data sets were fit using the constitutive model developed by Raghavan and Vorp [8].

4.3 Results

The biomechanical model proposed by Raghavan and Vorp[8] suits reasonably the stress-stretch data found for all specimens analyzed ($R^2 > 0.95$). Following figures shown the stress-stretch curves for layers of ATAA wall.

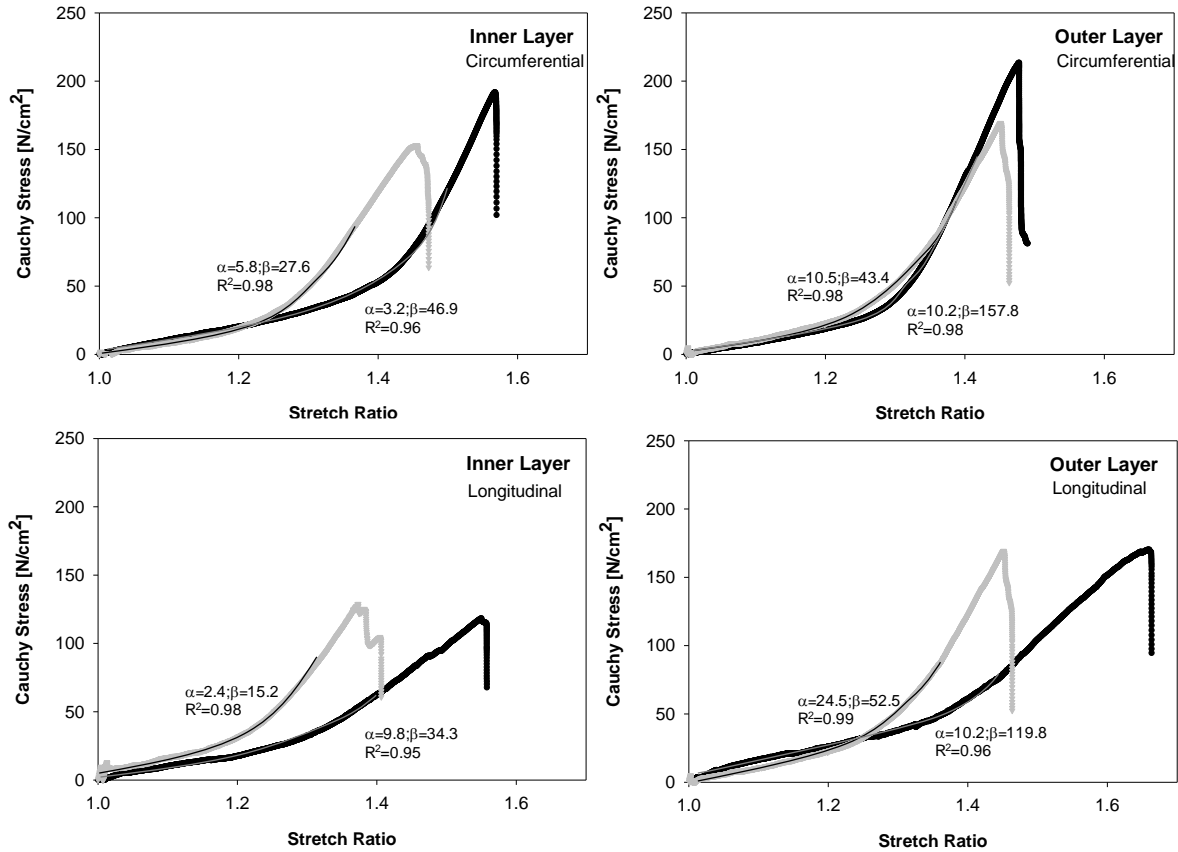


Figure 4.1: Representative tensile stress-stretch response for inner and outer layer of ATAAs with BAV (black dot) and TAV (gray dot); individual material parameters and determination coefficient are reported for each curve.

No difference was found among mean values of α and β , shown in the following table, for TAV and BAV ATAAs.

Table 4.1: Population mean values of material parameters obtained by fitting experimental data of all tensile tests on the inner and outer layers of ATAAs and used for FSI modeling. Material parameters are valid for stretch ratio below 1.3 for TAV ATAA and 1.45 for BAV ATAA, respectively. Data are mean \pm SEM.

	Inner Layer		Outer Layer	
	α [N/cm ²]	β [N/cm ²]	α [N/cm ²]	β [N/cm ²]
BAV ATAA (n=10)	7.6 \pm 2.8 (R ² =0.96)	48.7 \pm 9.4 (R ² =0.95)	14.9 \pm 5.6 (R ² =0.98)	158.1 \pm 15.8 (R ² =0.97)
TAV ATAA (n=7)	2.4 \pm 1.0 (R ² =0.96)	34.5 \pm 8.9 (R ² =0.97)	12.1 \pm 6.1 (R ² =0.97)	59.5 \pm 13.8 (R ² =0.98)

Maps of blood pressure (see figure 4.2) for ATAA patients shown no remarkable differences between values of pressure for BAV and TAV patients except for patient D in which high pressure insisted on a wider area if compared to other subjects. Both BAV and TAV ATAAs shown high blood pressure over cardiac cycle in the AA close to the greater curvature of the aortic wall.

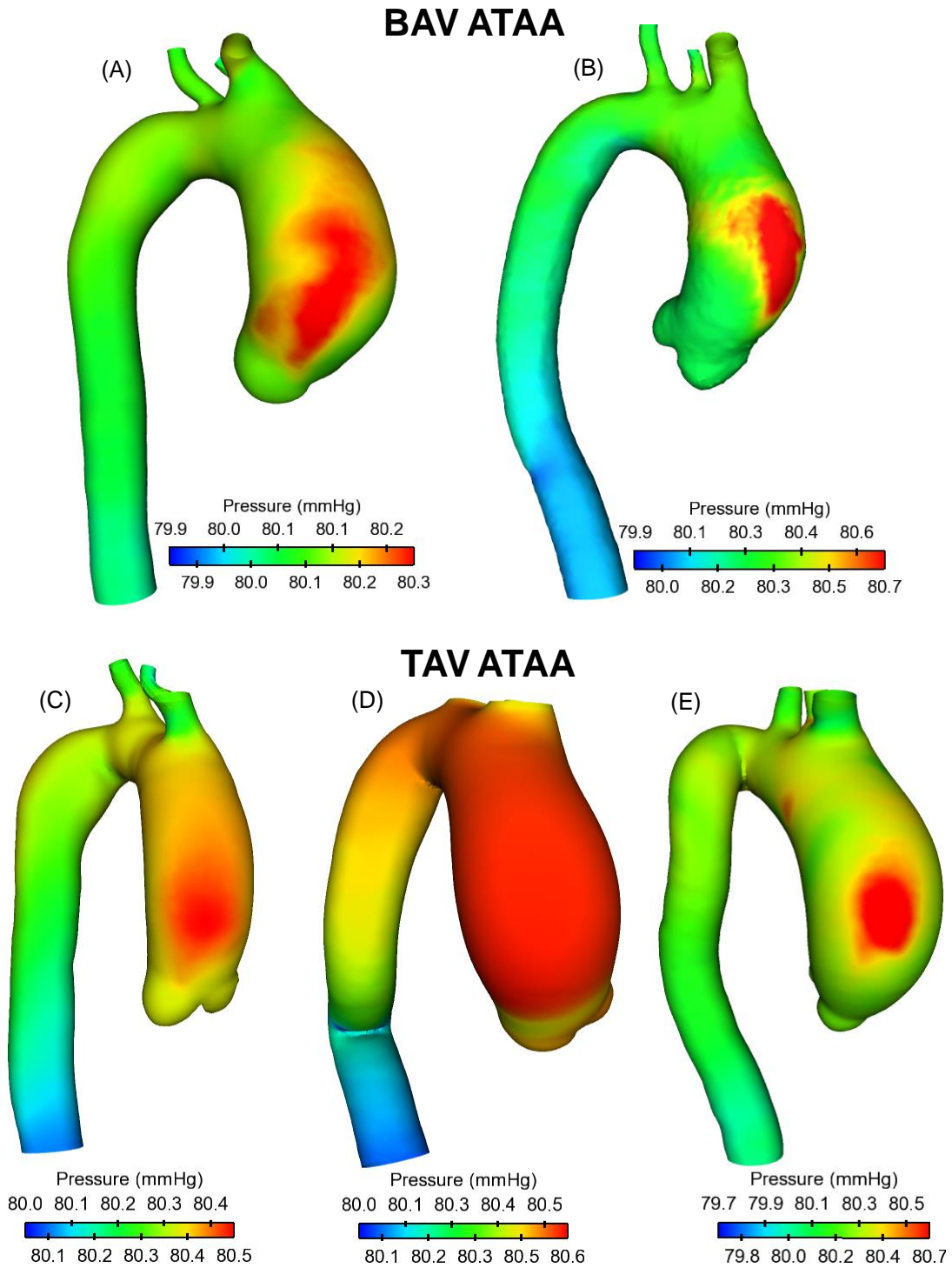


Figure 4.2: Time-averaged blood pressure map for ATAA patients with BAV (top two models) and TAV (bottom three models)

High WSS regions, shown in figure 4.3, affected the anterolateral region of AAs and the WSS distributions were similar to those of high-pressure distribution, see figure 4.2.

The region of high WSS was more extended for patients with BAV if compared to those with TAV. All patients, with exception of D, shown an increase of WSS and pressure values from the aortic valve to ascending dilated aorta; patient D had high WSS values in the sino-tubular junction (STJ) region for all the patients with the only exception of patient D in which elevated WSS was located into the STJ. These observations indicate that the anterolateral region of aneurysmal aorta is the most solicited and thus it is also the most exposed to risk of aneurysm onset and evolution.

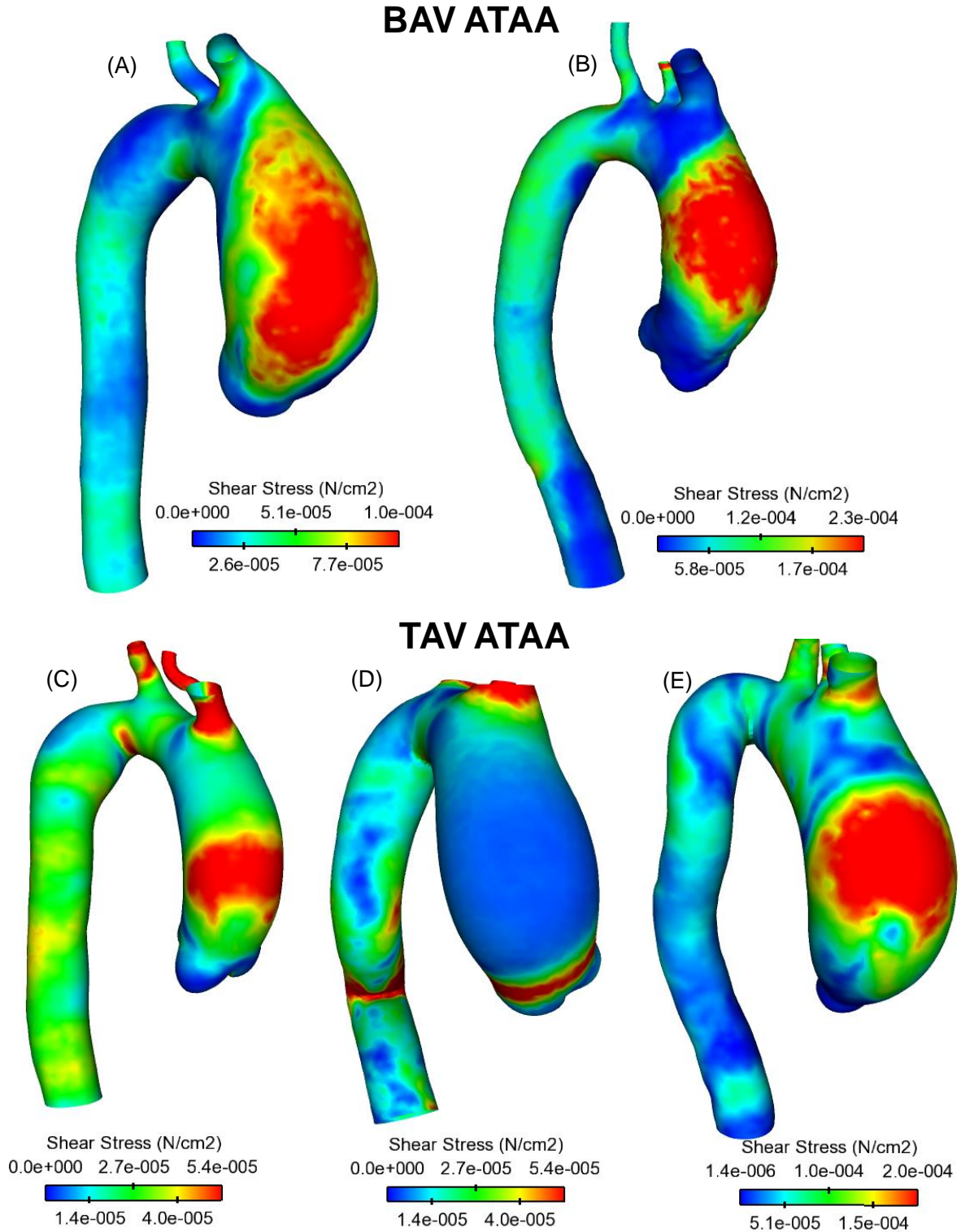


Figure 4.3: Wall shear stress for ATAA patients with BAV (top two models) and TAV (bottom three models)

WSS had a fluctuating trend during a cardiac cycle thus, this oscillation was studied by computing the oscillatory shear index (OSI); the latter is an index of the predominant blood direction during a complete cardiac cycle. OSI assumed values between 0.0 and 0.5, where 0.0 value indicates that blood follow an almost fixed direction during the cycle while 0.5 value indicates a highly oscillating flow. OSI, for all ATAAs, was high on the left and right side of the aortas whereas was low on the outer greater and inner smaller curvatures of the ascending aortas.

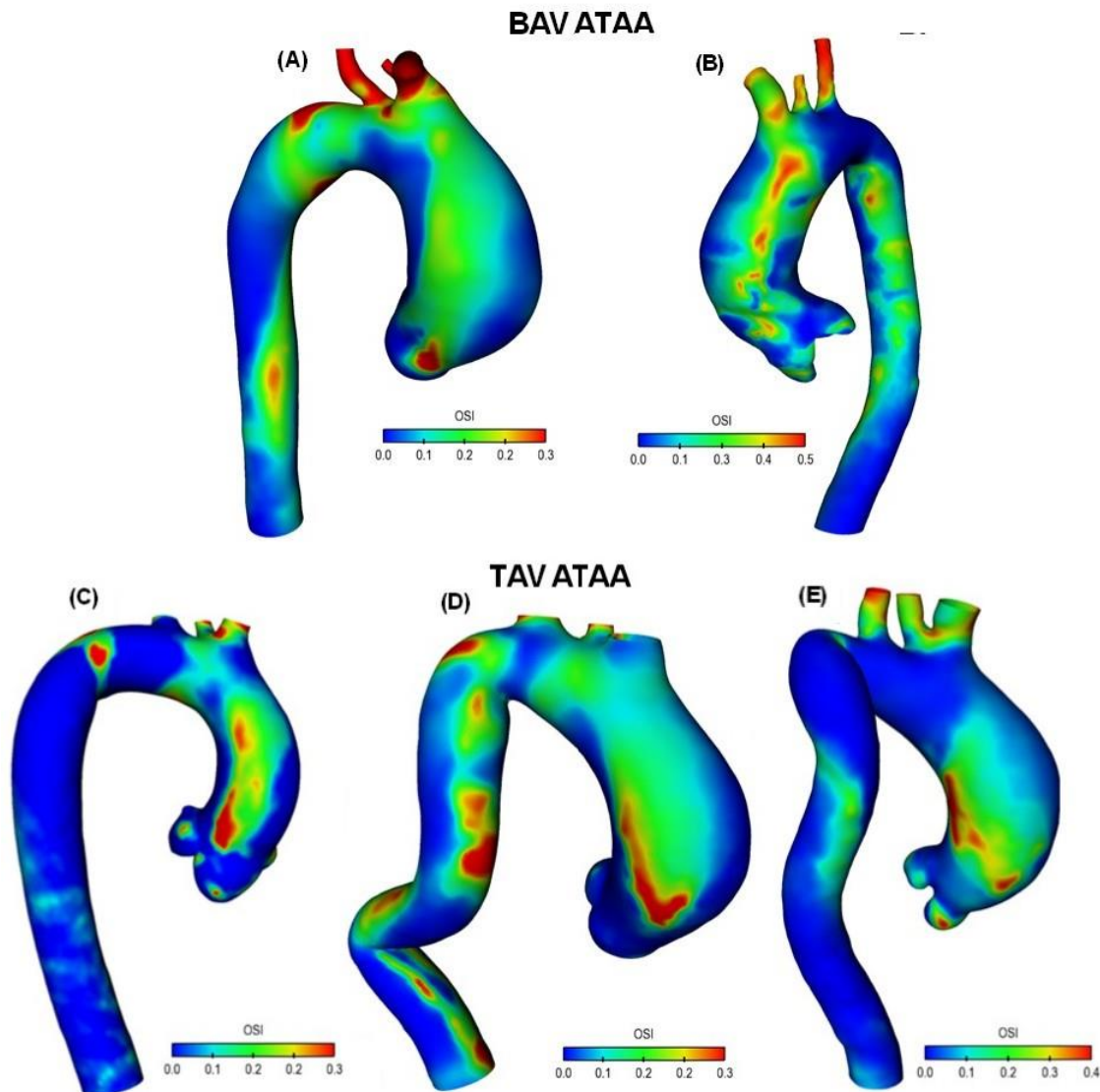


Figure 4.4: Distribution of oscillatory shear index (OSI) for ATAA patients with BAV (top two models) and TAV (bottom three models)

Distinguishing among the two studied groups, BAV ATAAs had lower values of TAWSS and higher values of OSI compared to those of TAV ATAAs even if, it is important to consider that, each aneurysm had a specific diameter and thus it is difficult to compare these 5 cases since their diameters are not comparable. However, it is possible to speculate that BAV introduced a highly skewed flow inside ATAAs that led to different OSI and TAWSS distributions than those of TAV ATAAs.

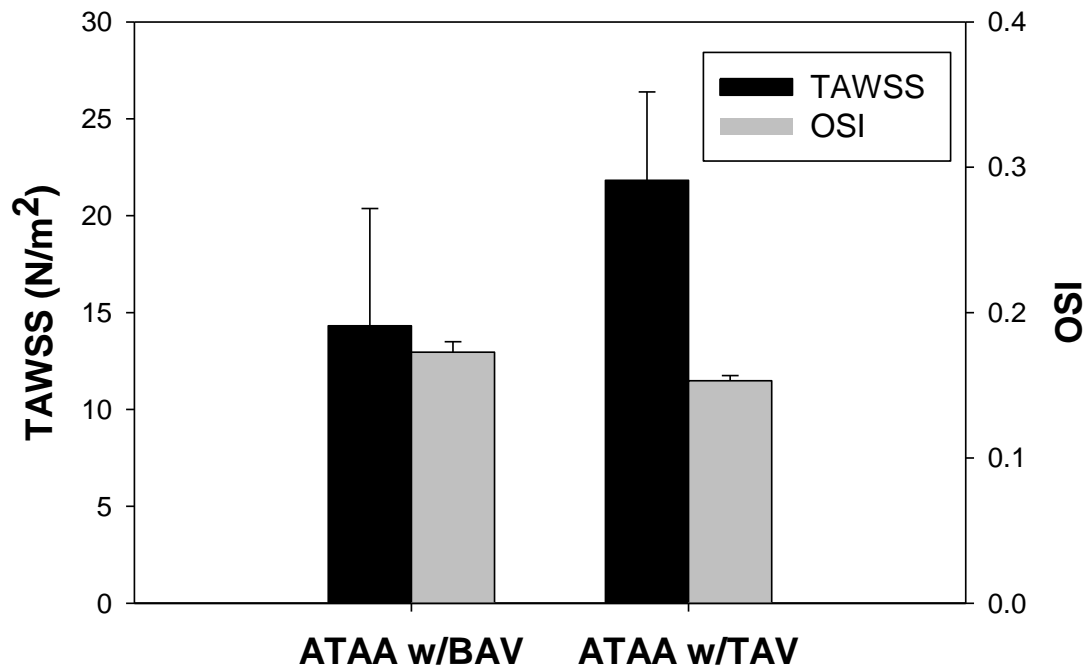


Figure 4.5: Comparison of both TAWSS and OSI for ATAAs with either BAV or TAV.

In the following figures, blood flow pathways for all ATAAs are illustrated by streamlines whereas vector analyses at aortic valve plane (AoP), STJ and AoA are shown only for patients (A) and (C).

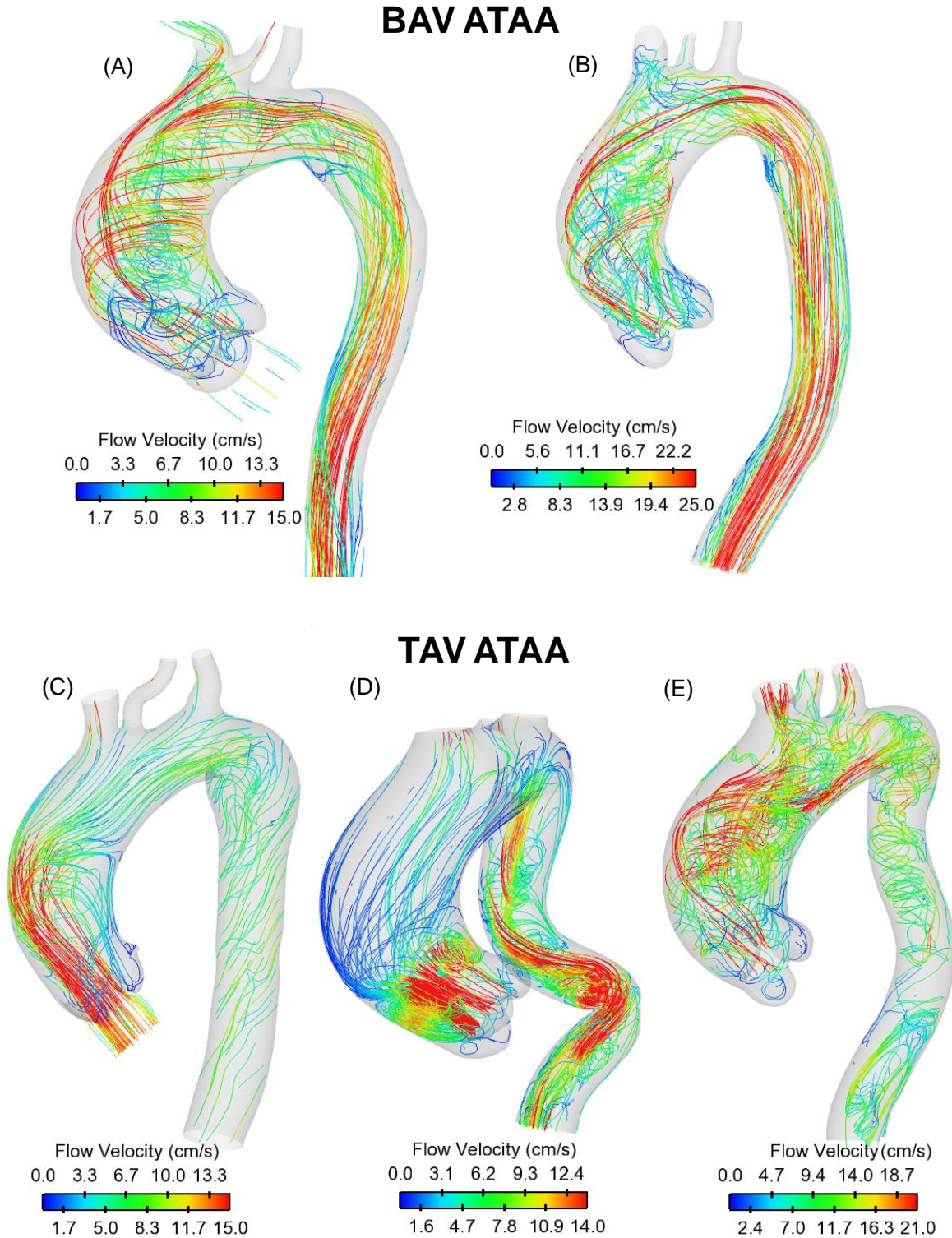


Figure 4.6: Streamlines of blood velocity over cardiac cycle for ATAA patients with BAV (top two models) and TAV (bottom three models)

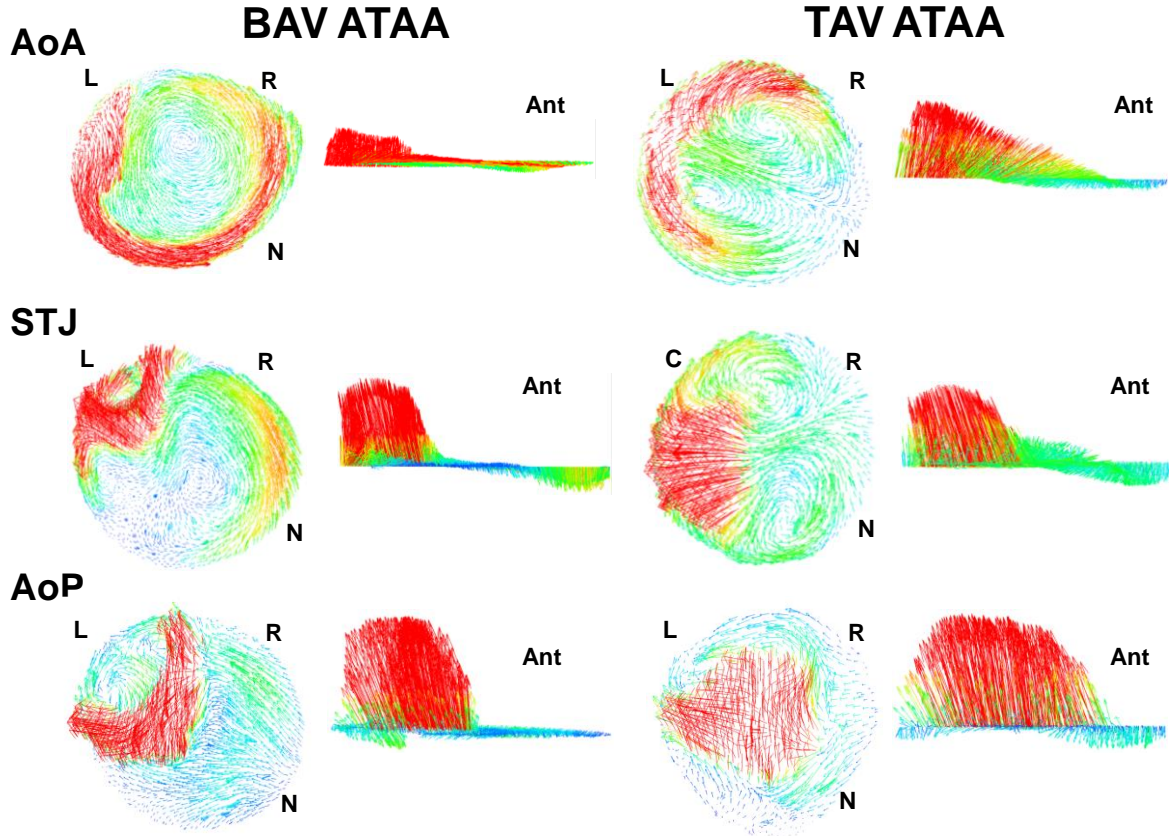


Figure 4.7: Vector analysis at AoP, STJ and AoA anatomical levels for ATAA patient (A) with BAV and ATAA patient (C) with TAV; *L* = left-coronary artery, *R* = left-coronary artery, *N* = non-coronary artery and *Ant* = anterior direction

For both patients (C) and (D) with non-stenotic TAV, parallel streamlines spanned the aneurysmal ascending aorta with minimal deviance from the initial direction of the aortic valve flow and slight degree of flow skewing close to the greater curvature of AoA. Slow, minimally helical flow was seen in AoP (Figure 4.7 for patients (C)). Additionally, the high blood flow velocity was manifested at same mid-ascending aortic location where the high blood pressure and WSS occurred (compare Fig. 4.6 with Figs. 4.2 and 4.3). In a different way, BAV ATAAs exhibited left-handed nested helical flows in the ascending thoracic aorta (Fig. 4.6 and 4.7), which were similar to those shown by Hope and collaborators [9] using 4D flow MR imaging. Abnormal flow pattern in which streamlines wrapped back toward the aortic valve was observed at AoP for patient (A) with BAV (Fig. 4.7). Using qualitative visual criteria suggested by Sigovan et al[10], we

observed mild flow eccentric flow at AoP and marked eccentric flow at STJ and AoA for patient (A) with BAV, see table 4.2.

Table 4.2: Population values of pressure, WSS and WPS.

	BAV			TAV		
	AoA	STJ	AoP	AoA	STJ	AoP
Flow Eccentricity	marked	marked	mild	mild	normal	normal
Pressure (mmHg)	80.52	80.45	80.37	80.45	80.38	80.32
WSS (N/cm ²)	8.2e ⁻⁵	7.8e ⁻⁵	6.5e ⁻⁵	5.4e ⁻⁵	3.0e ⁻⁵	1.5e ⁻⁵
WPS (N/cm ²)	28	42	23.3	23	30	18

Abnormal secondary flow pattern was marked for BAV ATAAAs and TAV ATAA with severe aortic stenosis and regurgitation but not exhibited by patients with fully opened TAV (i.e., both patients (C) and (D)).

For inner aortic layer of patients (A) and (C), local maxima of wall principal stress (WPS) were found higher than that of the outer layer (WPS= 30 N/cm² for inner layer and WPS = 8.5 N/cm² for outer layer of patient (C)). Patient (A) with BAV exhibited similar, but higher WPS than patient (C) with TAV (WPS = 42 N/cm² for inner layer and WPS = 30 N/cm² for outer layer of BAV ATAA).

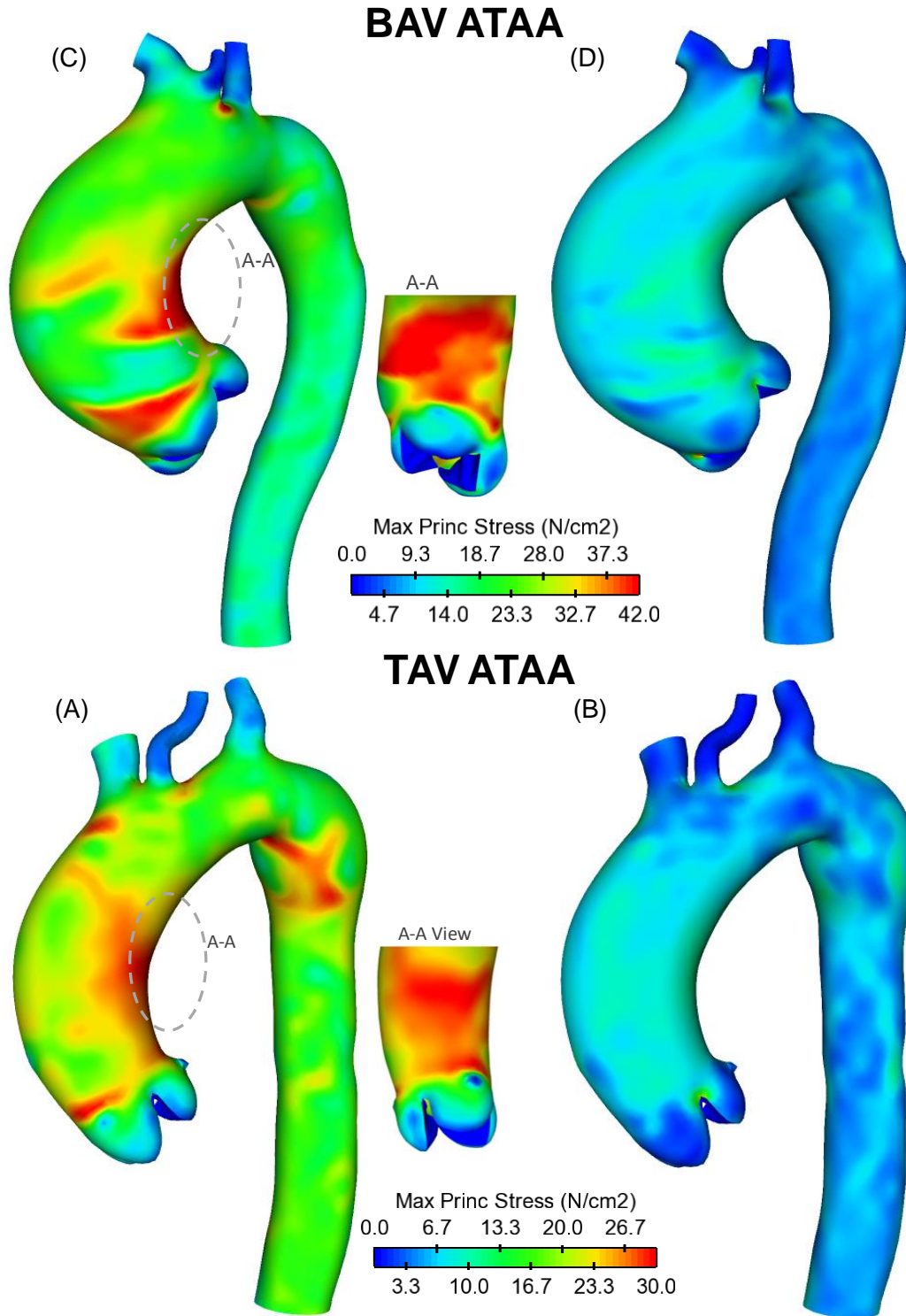


Figure 4.8: Comparison of maximum principal stress for ATAA patient (A) with BAV and ATAA patient (C) with TAV at inner layer (left models) and outer layer (right models).

These findings suggested that the stress was discontinuous, at the interface between aortic layers in the two-layered ATAA model, due to differences in material properties; this will most commonly results in tearing of the aorta. Similar stress discontinuities between inner and outer layers were found for all patients with either BAV or TAV. Local maxima of wall stress occurred on either the anterolateral or posterolateral regions of the ascending aorta, but stresses on the greater curvature side tended to be slightly greater than those related to the smaller side. Local maxima of WPS occurred just above STJ where type A dissection frequently occurs. High wall stresses ($WPS = 27.5 \text{ N/cm}^2$ for BAV ATAA and $WPS = 25.5 \text{ N/cm}^2$ for TAV ATAA at inner layers) were also observed in the aortic arch distal to the ostia of the supra-aortic vessels where type B dissections frequently occur [11]. This elevated stress region was most likely due to a stress concentration effect. Similar stress distributions at inner aortic layer were found for all ATAA patients with either BAV or TAV.

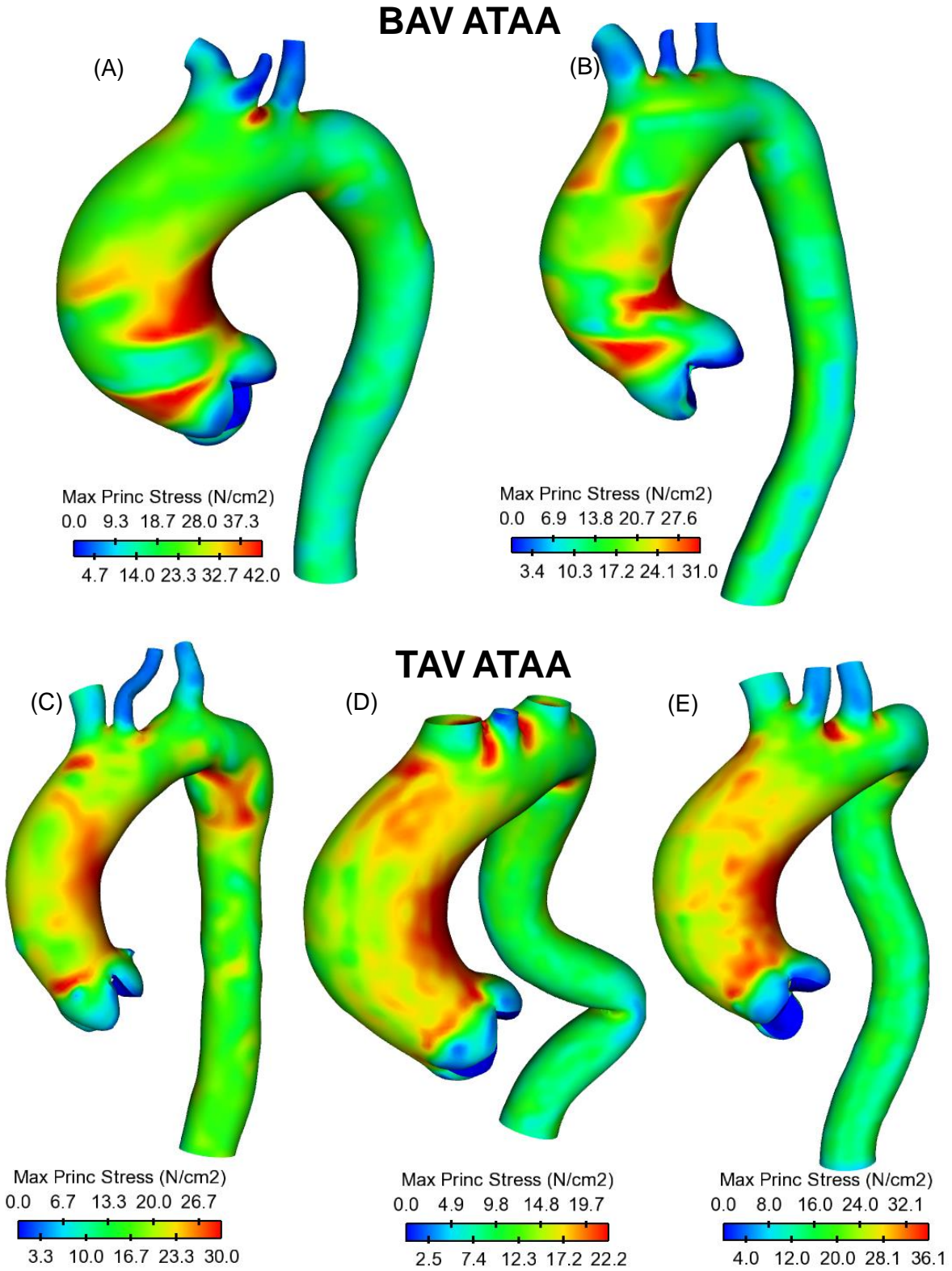


Figure 4.9 Comparison of maximum principal stress for ATAA patients with BAV (top two models) and TAV (bottom three models) at inner aortic layer.

Findings suggest that stresses just above STJ for patients with BAV appeared slightly higher than those of patients with TAV, highlighting a greater risk of AoD among patients with BAV (average WPS = 36.5 N/cm^2 for BAV ATAAs and average WPS = 29.4 N/cm^2 for TAV ATAAs).

4.4 Conclusion

- High hemodynamic stress and intrinsic aortic flow characterizing BAV predispose the aneurysmal aorta to an asymmetric, high wall stress distribution.
- Aortic valve morphology introduce eccentric blood flow jet angle and regional variation of shear loads exerted on aortic wall of ATAAs, which may ultimately cause a mechanism of destructive vascular remodeling and promote aneurysm dilatation
- Differences in elastic material properties of aortic layers are responsible for discontinuity of wall stress at layer interfaces.
- Intimal and media layers of aortic wall are stronger circumferentially than longitudinally.
- Abnormal blood flow and hemodynamic indicators may predispose patients to aneurysm development, and that dissimilarities are likely due to the pathological, different valve morphology.

References

1. McGloughlin, T.M. and B.J. Doyle, *New approaches to abdominal aortic aneurysm rupture risk assessment engineering insights with clinical gain*. Arteriosclerosis, thrombosis, and vascular biology, 2010. **30**(9): p. 1687-1694.
2. Cripe, L., et al., *Bicuspid aortic valve is heritable*. Journal of the American College of Cardiology, 2004. **44**(1): p. 138-143.
3. Keane, M.G., et al., *Bicuspid aortic valves are associated with aortic dilatation out of proportion to coexistent valvular lesions*. Circulation, 2000. **102**(suppl 3): p. Iii-35-Iii-39.
4. Shaaban, A.M. and A.J. Duerinckx, *Wall shear stress and early atherosclerosis: a review*. American Journal of Roentgenology, 2000. **174**(6): p. 1657-1665.
5. Sakamoto, N., et al., *Effect of spatial gradient in fluid shear stress on morphological changes in endothelial cells in response to flow*. Biochemical and biophysical research communications, 2010. **395**(2): p. 264-269.
6. Khanafer, K. and R. Berguer, *Fluid–structure interaction analysis of turbulent pulsatile flow within a layered aortic wall as related to aortic dissection*. Journal of biomechanics, 2009. **42**(16): p. 2642-2648.
7. Pasta, S., et al., *Effect of aneurysm on the mechanical dissection properties of the human ascending thoracic aorta*. The Journal of thoracic and cardiovascular surgery, 2012. **143**(2): p. 460-467.
8. Raghavan, M. and D.A. Vorp, *Toward a biomechanical tool to evaluate rupture potential of abdominal aortic aneurysm: identification of a finite strain constitutive model and evaluation of its applicability*. Journal of biomechanics, 2000. **33**(4): p. 475-482.
9. Hope, M.D., et al., *Bicuspid Aortic Valve: Four-dimensional MR Evaluation of Ascending Aortic Systolic Flow Patterns I*. Radiology, 2010. **255**(1): p. 53-61.
10. Sigovan, M., et al., *Comparison of four-dimensional flow parameters for quantification of flow eccentricity in the ascending aorta*. Journal of Magnetic Resonance Imaging, 2011. **34**(5): p. 1226-1230.
11. Conrad, M.F. and R.P. Cambria, *Contemporary management of descending thoracic and thoracoabdominal aortic aneurysms: endovascular versus open*. Circulation, 2008. **117**(6): p. 841-852.

Chapter 5

The role of aortic shape and valve phenotypes in aortic pathologies

5.1. Introduction

The work presented in the previous chapter, about the study of hemodynamic differences between patients with ATAA and BAV or TAV, represents an important starting point since it highlights the reliability of FSI analyses when applied to aortic dilatation. Specifically, FSI reliability was assessed by comparing, qualitatively, results obtained with computational methods with those presented by other groups [1] and obtained with other diagnostic tools (i.e. 4D flow MRI). Despite its importance, the previous work presents some weaknesses connected to the small sample size (i.e. only 3 TAV and 2 BAV models) and to the difficulties related to the comparison of results obtained from geometries with different aortic dimension. In a different way, statistical relevance of the previous work was low and the selected geometries were collected from patient with very different demographic data and different degree of aortic dilatation. Thus, aim of this work was to overcome the highlighted problems connected to the previous study by evaluating a wider number

of patients (i.e. 17 BAV patients and 6 TAV patients) and studying the differences between patients with comparable aortic diameters but different valve morphologies.

The present chapter was focused both on the study of hemodynamic in aortic aneurysms with different valve morphologies and on the assessment of hemodynamic differences between BAV patients with different valve phenotypes. More in detail, a first comparison was executed on ATAAs with BAV and TAV while a second and deeper comparison was executed on patients with BAV and different phenotypes.

The idea to study the hemodynamic inside BAV phenotypes generates from the emerging evidence that the heterogeneity of BAV phenotypes, reflecting the diverse molecular pathways, flow dynamics and patterns of aortic dimension, may have a prognostic implication on the development of the bicuspid aortopathy. Thus, the principal hypothesis is that a different aortic valve coaptation area and a different aortic valve opening mechanics may change the hemodynamic inside ascending aorta and thus be responsible for growing of an ATAA. Indeed, BAV-related hemodynamic disturbances may increase local WSS, promoting abnormal regulatory pathways of matrix disruption and fragmentation with consequence weakening and dilatation of the aorta. For this, a group of patients with ATAA and different valve morphologies were studied. Specifically, FSI analyses were executed on patient specific aortic geometries and hemodynamic parameters were collected and studied. Both morphological, demographic and hemodynamic data got by each sub-group were compared with statistical analyses.

5.2. Method

5.2.1. Data collection

For the purpose of this study, patients data with ATAA were retrospectively collected from the registry of our local hospital. Among all the patients present in this registry, we collected a group of them with comparable aortic diameter dimension and with aortic insufficiency (AI) and stenosis

(AS) lower or equal to moderate. In this way, the study group comprised of 28 patients matched for the degree of aortic dilatation.

Several data were collected for each of these patients; specifically, demographic (i.e. age and gender), morphological (i.e. ATAA geometry, valve morphology), clinical (i.e. aortic valve pathologies, patient general condition, level of stenosis and regurgitation, transthoracic aortic flow) and radiological (ECG-gated CTA) data were studied.

Since the patients selected for this study should be comparable for the dimension of their aorta, three regions of the thoracic aorta (i.e. Sinus of Valsalva, STJ and AA) were identified as shown in Figure 5.1. The dimensions of the aorta, in these regions, were evaluated and the results obtained were used to include or exclude patients from the sample chosen.

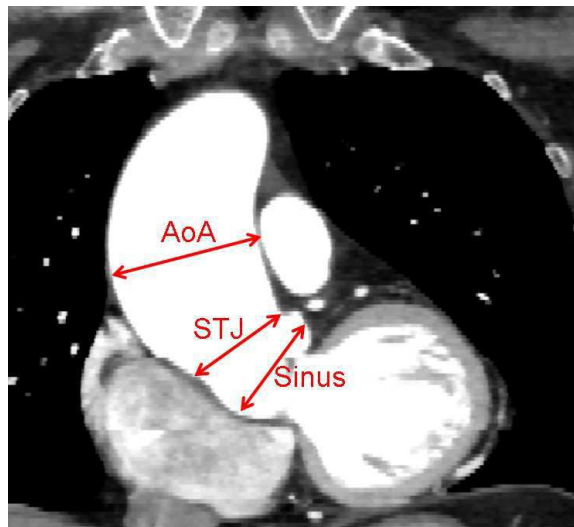


Figure 5.1: Regions of interest for the determination of aortic diameter dimension

After morphological data collection, ATAAs were classified, as shown in figure 5.2, into two groups (i.e. Type TA and Type AR) according to their patterns of dilatation:

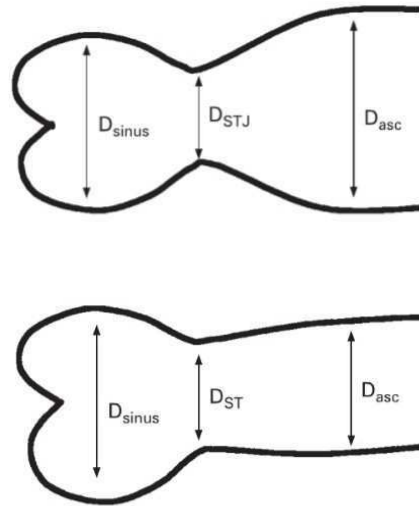


Figure 5.2: Schaefer aortic morphology classification[2] used to classify BAV and TAV patients. Patients with Type TA aortic dilatation had $D_{\text{sinus}} < D_{\text{STJ}}$ and $D_{\text{sinus}} < D_{\text{AoA}}$ while patients classified as Type AR had $D_{\text{sinus}} > D_{\text{STJ}}$ and $D_{\text{sinus}} \geq D_{\text{AoA}}$.

In a similar fashion, patients with BAV were classified according to their phenotype into AP-BAV and RL-BAV following the classification proposed by Kang et al. in their research [3].

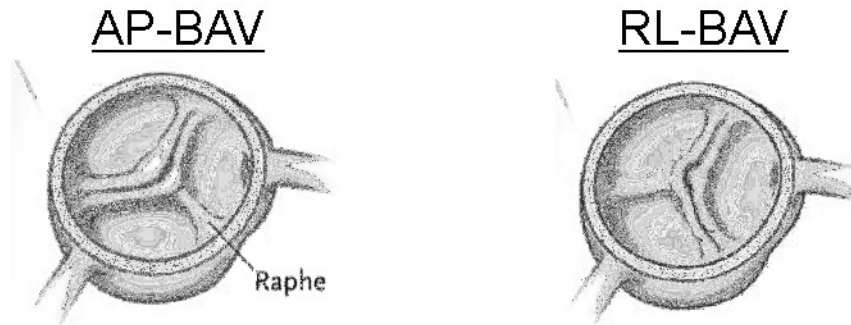


Figure 5.3: BAV divided on the base of their phenotypes into antero-postero (AP) BAV and right-left (RL) BAV

5.2.2. Computational analyses

CTA images were segmented, using the vascular modeling toolkit VMTK v0.9.0 (<http://www.vmtk.org>), to reconstruct the three-dimensional (3D) AoD geometries of each

patients. Model reconstruction included the aortic valve, ascending aorta, aortic arch with supra-aortic vessels and the descending aorta. The models were reconstructed with the aortic valve fully opened.

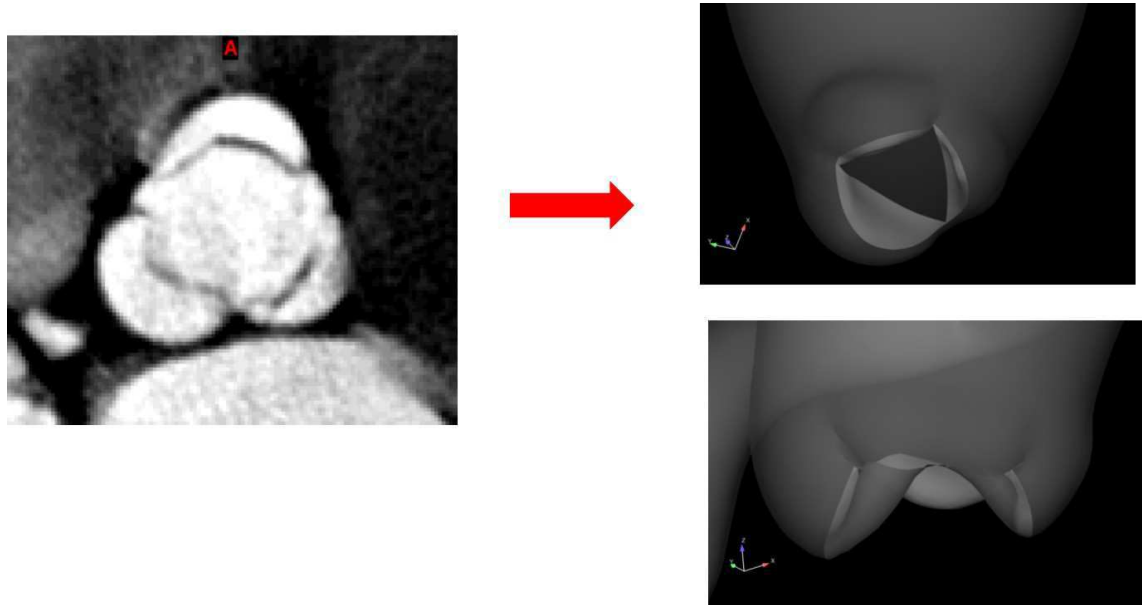


Figure 5.4: (A) Tricuspid aortic valve axial view in ECG-gated CT angiography. (B), (C) 3D reconstruction of a tricuspid aortic valve fully opened

After reconstruction, 3D models were exported to Gambit (ANSYS Inc., Canonsburg, PA) for meshing both fluid (lumen) and structural (aneurysm wall) domains.

Parallel coupled, two-way FSI analyses were performed using the commercial software MpCCI (Fraunhofer SCAI, Germany) to couple the structural component, Abaqus (SIMULIA Inc, Providence, RI), and the fluid solver, Fluent (ANSYS Inc., Canonsburg, PA). Only the systolic peak was simulated and the exchange time step was set to 0.1 s for a total time of 4 s, which ensured convergence analysis. Data exchange occurred every time step with Fluent sending the fluid-induced wall forces to Abaqus and Abaqus sending the deformed nodal coordinates to Fluent

In the structural model, the aortic wall was modeled as hyperelastic and bi-layered material where the inner layer consisted of the tunica intima and a portion of the tunica media while the outer layer consisted of the tunica adventitia and a portion of the tunica media. The constitutive model adopted was the fiber-reinforced constitutive modeling method proposed by Gasser and collaborators [4].

$$W = \frac{C}{2}(I_1 - 3) + \frac{k_1}{k_2} \{ \exp[k_2(kI_1 + (1 - 3k)I_{4i} - 1)^2] - 1 \} \quad \text{Eqn. 5.1}$$

The k_1 , k_2 and C parameters used in this constitutive model were collected by a study of Pasta and collaborators.

Aortic wall thicknesses were imposed at 1 mm and 0.7 mm for the outer layer and inner layer, respectively. For the aorta to deform in physiological way, the distal ends of supra-aortic vessels, aortic valve and descending aorta were fixed in all directions.

For the fluid model, the blood flow was assumed incompressible and Newtonian with a density of 1060 kg/m³ and viscosity of 0.00371 Pa x s. The PISO algorithm was used for pressure-velocity coupling and a second order upwind scheme for discretization of each control volume. Convergence was enforced by reducing the residual of the continuity equation by 10⁻⁵ at all-time steps. To include patient-specific flow conditions, the fluid model adopted the trans-aortic flow measurements obtained by Doppler echocardiography as the inflow velocity at aortic valve. This flow was distributed between supra-aortic vessels and descending aorta with a ratio of 40/60. A re-meshing technique was used, with re-meshing cells in Fluent are re-meshed based on whether they violate a user specified size and skewness criteria.

A fluid-dynamics analysis in addition to the FSI analysis was performed for each patient to assess the wall shear OSI and the helical flow index (HFI). The HFI gives an information about the helical blood flow pathway and, it has been demonstrated to be a good descriptor of the complex 3D blood flow[5, 6]. The HFI assumes values that range between 0 and +1 and it was calculated as described by Morbiducci et al. [5-7]:

$$HFI = \frac{1}{N_p} \sum_{k=1}^{N_p} hfi_k \quad \text{Eqn. 5.2}$$

Where N_k is the number of points j ($j=1, \dots, N_k$) in the k th trajectory ($k=1, \dots, N_p$) and hfi_k is a quantity that describe the dynamics of the k particle moving in a vessel.

$$hfi_k = \frac{1}{Nk} \sum_{j=1}^{Nk} |LNH|_j \quad \text{Eqn. 5.3}$$

With $0 \leq hfi_k \leq 1$.

The value LNH is the local normalized helicity and is described as:

$$LNH(s; t) = \frac{V(s;t) \cdot \omega(s;t)}{|V(s;t)| |\omega(s;t)|} \quad \text{Eqn. 4.4}$$

The LNH, that is function of the space and the time, assumes values that range between [-1; +1]. Specifically, LNH assumes values close to 1 or -1 if the flow is totally helical and assumes values close to zero in the presence of fluid dynamical reflectional symmetry. The differences between LNH=1 and LNH= -1 is only connected to the blood flow direction of rotation.

5.2.3. Statistical analyses

Statistical analyses were performed to compare all the patients' data and to evaluate if significance differences were present between the different groups.

More in detail, student t-test was performed to compare demographic, morphological and hemodynamic data of BAV versus TAV patients and of BAV AP versus BAV RL patients. Statistical analyses were performed using SPSS software (IBM SPSS Statistics, New York, NY). All the results are shown as mean \pm standard deviation and all the probability values were considered significant at the 0.05 threshold.

5.3. Results

BAV was observed in 17 patients with ATAA while, TAV was observed in 6 individuals. More in detail, patients with BAV-AP were 12 (70%) and they shown a TA dilatation as compared to AR dilatation (n. 9 with TA and n.3 with AR). Differently, BAV-RL occurred in 5 individuals (30%), with only one case of AR dilatation. Following Kang classification[3], among patients with type RL BAV 3 had a type 3 valve and 2 a type 5 valve; while, among patients with type AP BAV, 10 had a type 1 and 3 a type 2 valve.

In the following table 5.1, the main morphological and demographic data for both BAV and TAV ATAAs are reported. BAV patients shown a mean age of 57.3 ± 13.4 years compared to 67.5 ± 7.5 years for TAV patients.

Table 5.1 Sample studied divided into BAV and TAV ATAAs. D_{sinus} = ATAA diameter at sinus region; D_{stj} diameter at sino-tubular junction; D_{AoA} diameter at ascending aorta region; AI = aortic insufficiency; AS = aortic stenosis.

	BAV ATAA (n=17)	TAV ATAA (n=6)
Age	$57.3 \pm 13.4^*$ yrs	67.5 ± 7.5 yrs
Male	80%	65%
D_{sinus}	37.5 ± 4.8 mm	37.8 ± 3.8 mm
D_{STJ}	35.5 ± 6.1 mm	38.4 ± 6.4 mm
D_{AoA}	42.8 ± 5.7 mm	45.9 ± 9.2 mm
AI	18% moderate	25% moderate
AS	5% moderate	12% moderate
* indicate $p < 0.05$		

In a different way, it may be observed that patients with BAV are younger when reach the same dilatation of patients with TAV. These results were statistically relevant since, from t-test analyses for comparing the two population mean age distribution, a p-value = 0.02 was found.

In the studied sample, BAV patients with moderate AI were 18% while those with moderate AS were 5%; in a similar fashion, among TAV patients, 25% shown AI and 12% AS.

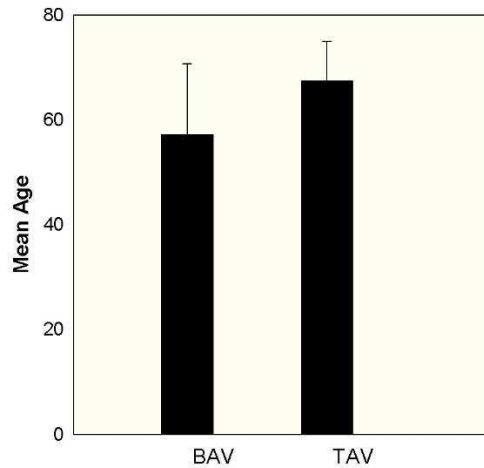


Figure 5.5 BAV vs TAV mean age distribution

The sample accounted for more male patients than female for both BAV (80% male presence) and TAV (65% male presence) group and this reflect what already know from several literature works.

The BAV and TAV ATAAs studied shown a diameter at sinus region of 37.5 ± 4.8 mm and 37.8 ± 3.8 mm respectively; in the sino-tubular region the diameter was 35.5 ± 6.1 mm for BAV and 38.4 ± 6.4 mm for TAV while, in the AoA region ATAA dimension was 42.8 ± 5.7 mm for BAV and 45.9 ± 9.2 mm for TAV. Statistical analyses were also performed on these groups of data to assess the absence of statistical differences and thus to be sure to work with comparable specimens.

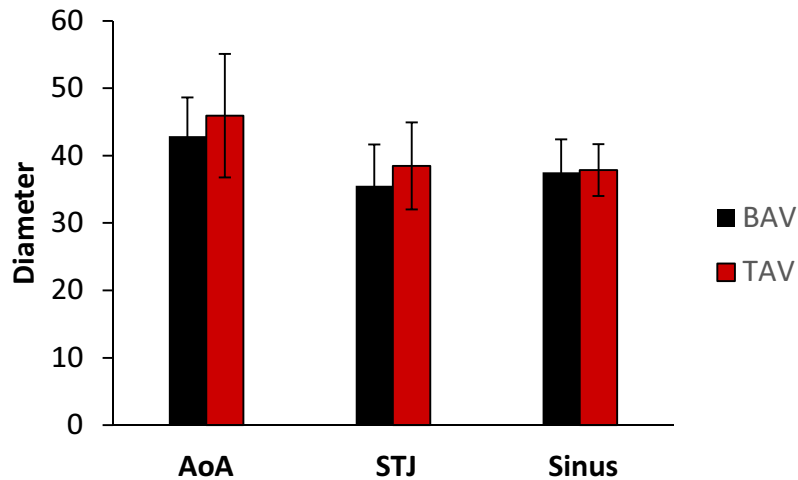


Figure 5.6: Diameter comparison between patient with BAV and TAV at different ascending aorta location. AoA= ascending aorta; STJ =sino-tubular junction; sinus = Sinus of Valsalva Velocity streamlines for patients with ATAA and BAV are shown in figure 5.7; these streamlines shown that, inside a group of patients with the same valve morphology (i.e. BAV), the pathway followed by the blood is strictly connected with the AA morphology and dimension.

BAV patients shown a helical flow in the AA characterized by a left-handed pathway. Specifically, as soon as the blood left the valve region it began to create eddies in the sino-tubular region. A portion of this blood flow continued straight up to the outer curvature of the ascending aorta where, as consequence of the contact with the aortic wall, changed its direction. Moreover, this portion of fluid accelerated along the outer curvature of the ascending aorta. The other portion of the blood flow began to follow a helical pathway as soon as it left the sino-tubular region.

Patient no. 14 had a particular ascending aortic morphology and it may be speculated that this was the cause of the particular blood pathway in this specific case. Indeed, this patient shown straight blood velocity streamlines on the outer curvature and large eddies in the smaller ascending aorta curvature; these eddies seems to form a stagnation region. A similar streamlines profile was observed in patient no. 4 and no. 12.

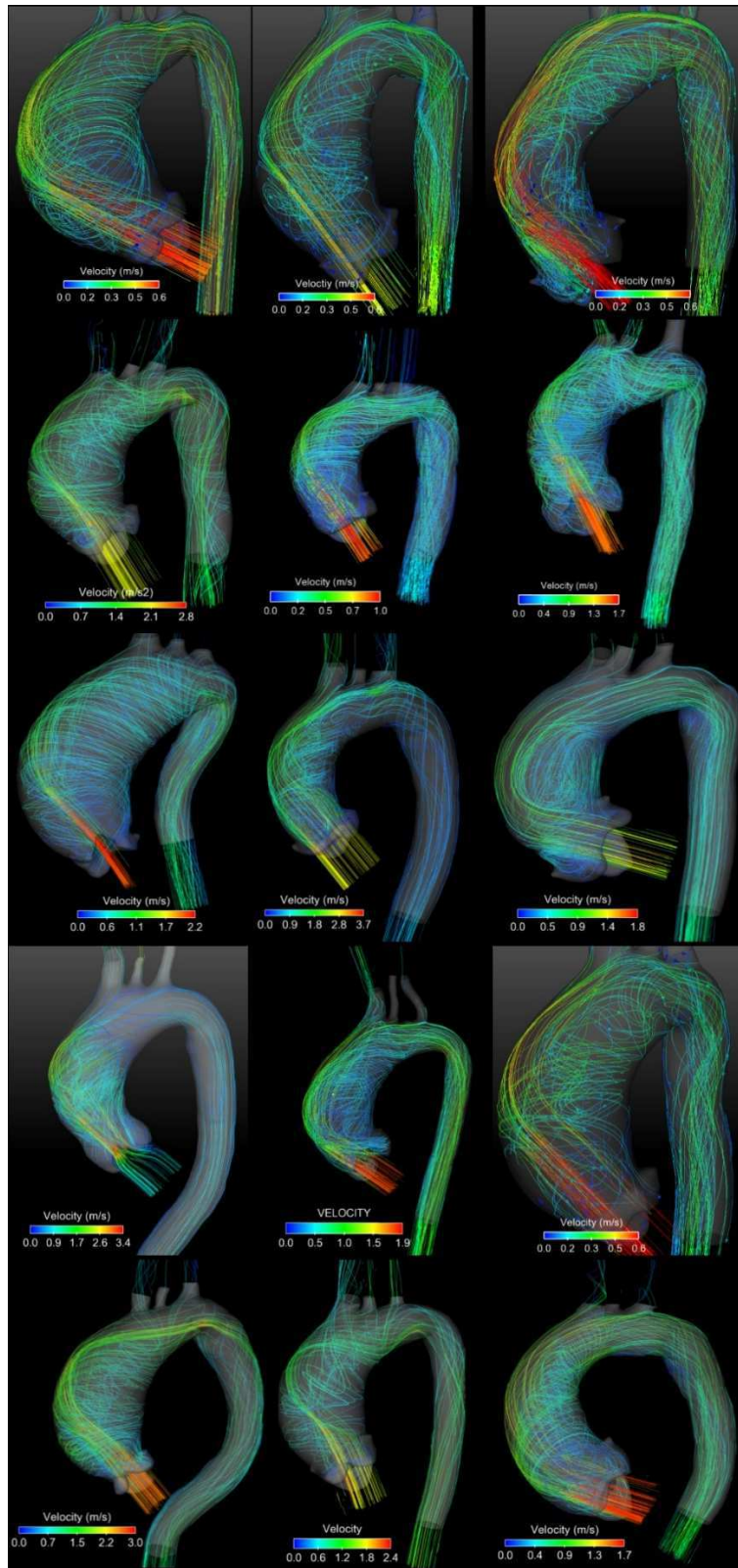


Figure 5.7: Streamlines of blood velocity over cardiac cycle for ATAA patients with BAV AoA where high blood pressure occurred

Maps of blood pressure for ATAA patients shown high blood pressure over cardiac cycle in the AA close to the convex, greater curvature of the aneurysmal wall (figure 5.8). More in detail, the position and extension of the spot at high-pressure was strictly related to AA and valve geometries. It was observed that the high-pressure spot was localized where the portion of blood that followed a straight pathway got in contact with the aortic wall at greater curvature. The highest-pressure values ranged between 121 mmHg (patients no. 1, no.2, no.3 and no. 11) and almost 208 mmHg (patient no. 15). Patients no. 6, no. 12 and no. 14 shown the high pressure spot close to the sino-tubular region and this could be matched with a highly curve aorta. Pressure were high in patients with high blood flow velocity (see patient no. 2, no. 5, no. 6, no. 13 and no. 15).

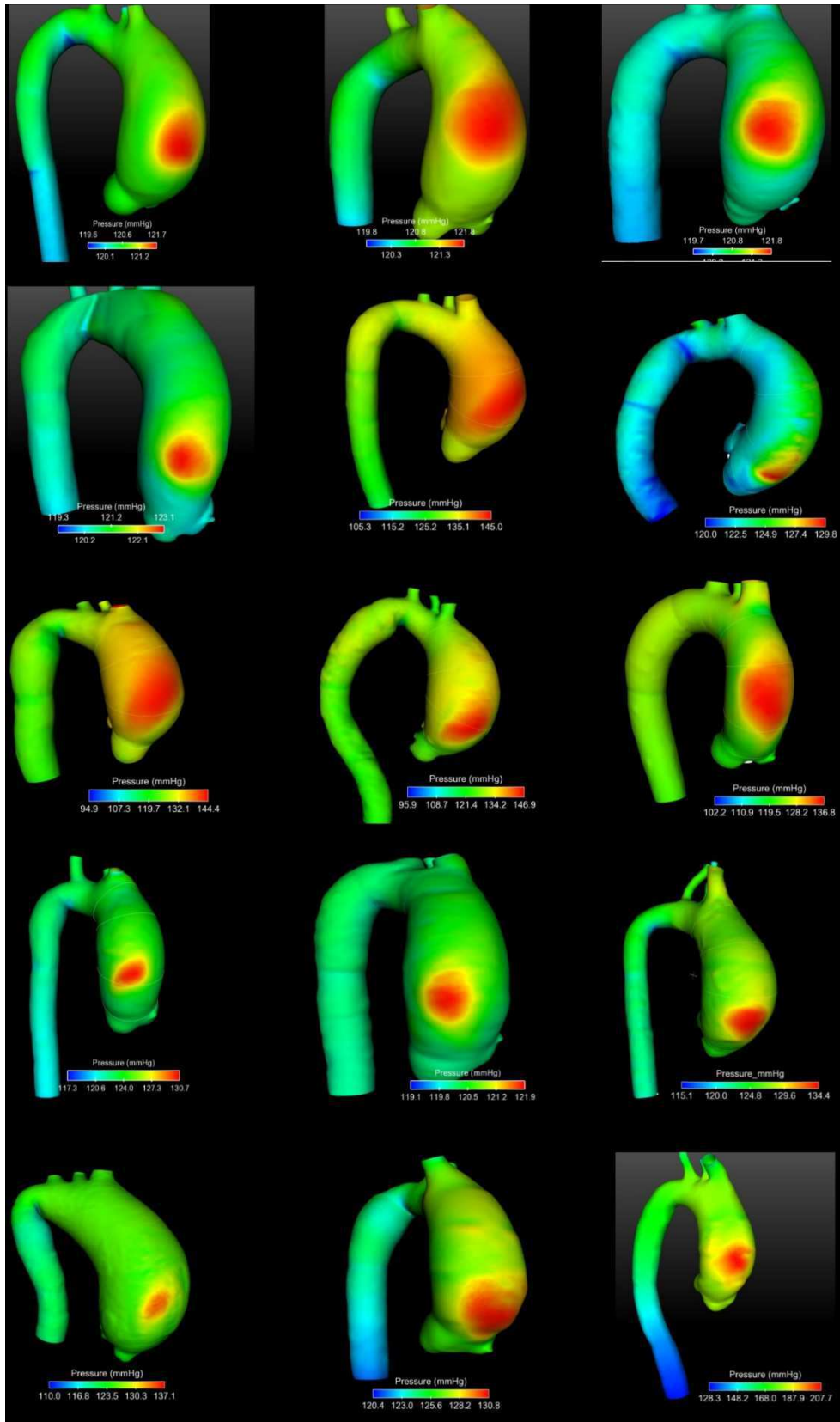


Figure 5.8: Blood pressure map for ATAA patients with BAV at systole

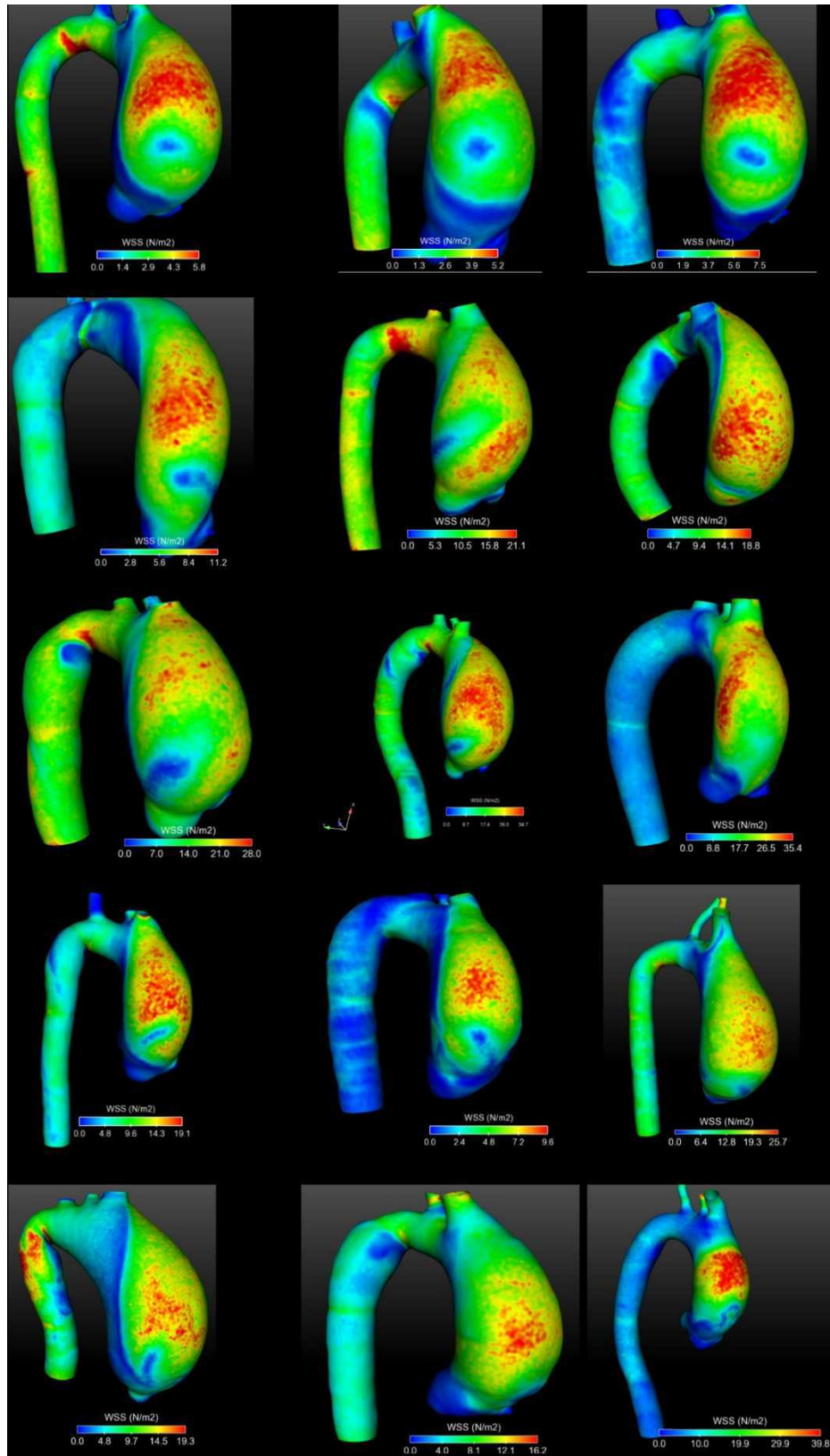


Figure 5.9: Wall shear stress for ATAA patients with BAV

WSS distribution for BAV patients is shown in figure 5.9. In this representation, the sites of minimum WSS were observed in the anterolateral region of low AA where high blood pressure occurred (see figure 5.8) and in the region of the sinus of Valsalva. WSS values ranged between 5.2 N/m^2 (see patient no.2) to 39.8 N/m^2 in patient no. 15 and they depended on the degree of blood flow velocity.

Statistical comparisons between WSS in BAV and TAV patients were also performed at different AA locations; specifically, as shown in figure 5.10, 5 regions were identified and studied (i.e. AA3, AA2, AA1, STJ, Sinus).

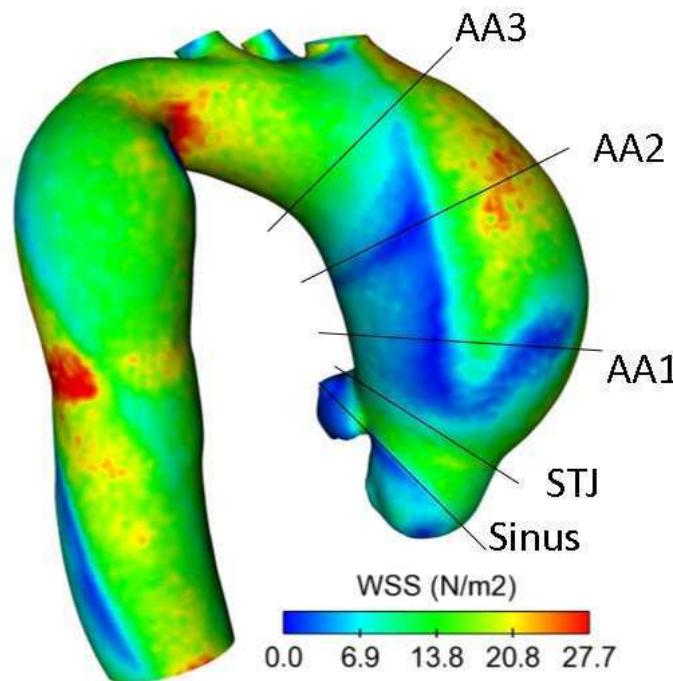
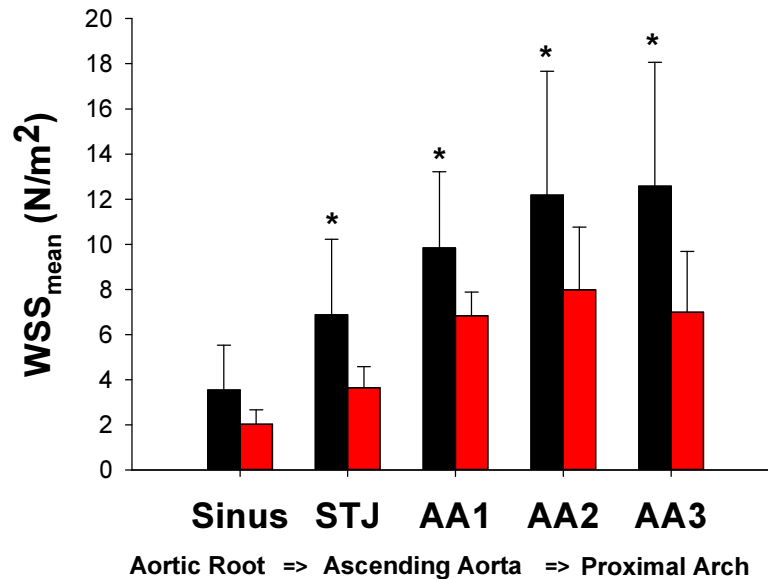


Figure 5.10: Representation of the 5 region considered to evaluate, statistically, if difference were present between WSS in patient with BAV and TAV

It was found that WSS in BAV ATAAs was higher than WSS associated with TAV ATAAs when compared at same aortic region. This difference was statistically significant in every aortic region except for the sinus zone ($p > 0.05$). Moreover, it was observed that WSS mean values increased, for both BAV and TAV ATAAs, from the aortic root to the proximal aortic arch; the only exception

was represented by the AA3 sector of TAV ATAAs in which the WSS decreased respect to the AA2 sector.

Among the group of BAV ATAAs, the difference between WSS related to AP and RL valve was also investigated. As shown in figure 5.11, WSS values were evaluated at 8 points (i.e. antero (A), right-antero (RA), right (R), postero-right (PR), postero (P), left-postero (LP), left (L) and antero-left (AL)) along the circumferential pathway of the AoA. Significant statistical differences were found in the AA2 region at RA, A and AL, in AA1 region at R and in STJ region at RA and A. WSS values were found higher in AP BAV if compared to RL BAV in the whole STJ region and in the antero-lateral portion of the AA2 region. RL BAV shown, in the R point of the AA1 and AA2 regions high values of WSS even if this result is not statistically significant.



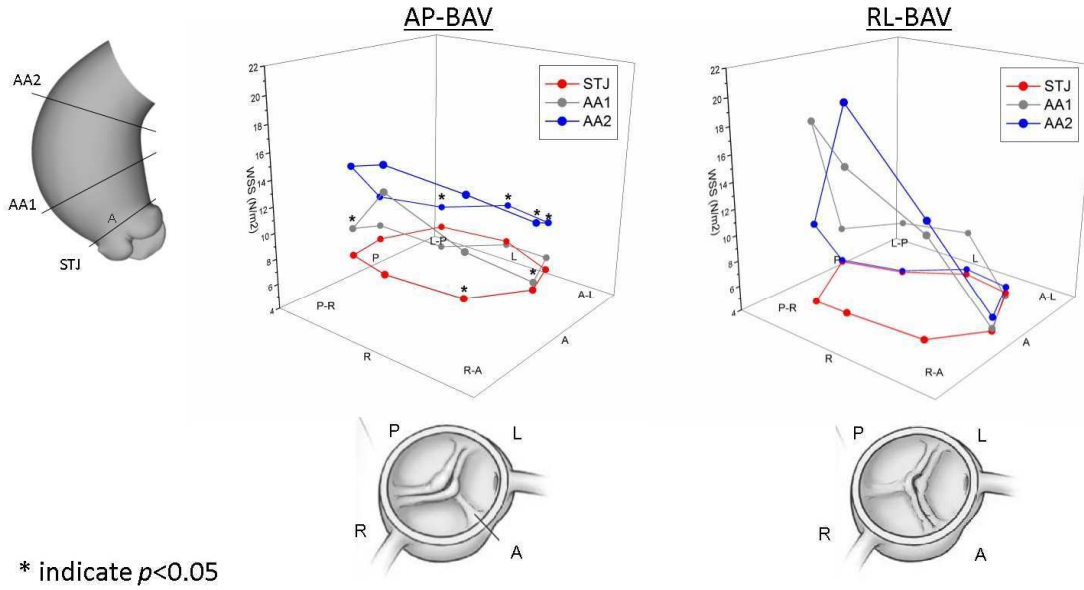


Figure 5.11: (a) Statistical comparison of WSS between patient with BAV (black bar) and TAV (red bar) at different ascending aorta locations. **(b)** Statistical analysis of WSS between patient with AP and RL BAV.

Differences in WSS were also evaluated by subdividing the total population studied into two groups on the base of the aortic dilatation profile. Thus, as already done in the comparison of AP and RL BAV, a statistical analysis was executed for these two sub-groups. It was observed that, for the entire investigated region, the AR WSS was slightly higher than that measured for TA. Specifically, in the AA1 and AA2 regions the WSS difference had statistical significance only at PR and P while in the STJ region the statistical difference was present only at PR.

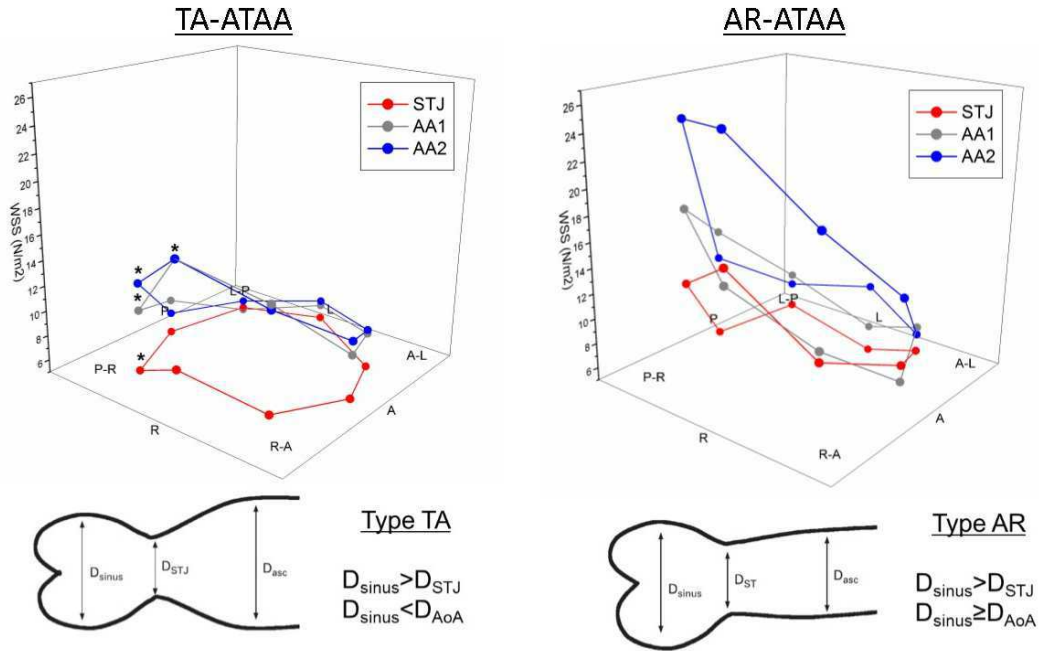


Figure 5.12: Statistical analysis of WSS between patient with type TA and type AR aortic dilatation.

Shear forces were investigated, in a different way, by comparison of OSI between patients with BAV and TAV. Specifically, a statistical analysis was executed, for each of AoA segments, to assess if differences were present in OSI values for these two sub-groups of ATAA patients. As shown in figure 5.13, patients with TAV had, for each of AA segments, a higher OSI if compared to BAV at same aortic region. However, the obtained results had no statistical relevance since the threshold values obtained were: $p=0.270$ for AA3, $p=0.102$ for AA2, $p=0.107$ for AA1, $p=0.284$ for STJ and $p=0.619$ for sinus.

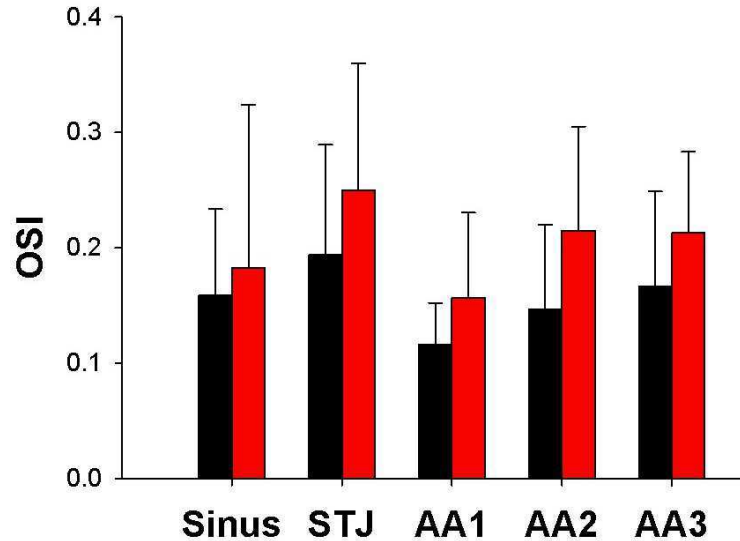


Figure 5.13: OSI values comparison between BAV (black bar) and TAV (red bar) patients

5.4. Discussion

In this work, the influence of valve morphologies on ATAA hemodynamic was investigated. The basic idea was that hemodynamic alterations may be responsible for aortic dilatation as much as genetic alteration, and that these alterations may be related to a particular valve morphology. Thus, we studied several hemodynamic parameters, which describe the blood flow inside the AA, and their relation to valve morphology.

Thus, it is possible to conclude that:

- Patients with BAV are younger than those with TAV when reach the same magnitude of aortic dilatation.
- Aortic valve morphology and phenotype, in synergy with aortic morphology, influence blood pathway, aortic wall pressure and stress distribution.
 - In BAV ATAA blood flow follows a left-handed helical pathway while in patients with TAV blood flow is straight with minimum deviance.

CHAPTER 5: The role of aortic shape and valve phenotype in aortic pathologies

- Patients with ATAA experience high blood pressure in the portion of wall (i.e. high-pressure spot) of AA at higher curvature. High-pressure value is related to blood pathway and to the incidence of the blood flow on aortic wall. Moreover, high-pressure spot changes its wideness depending on AoA morphology and valve coaptation area.

- WSS is higher for BAV patients if compared to TAV patients.

- BAV phenotypes influences hemodynamic parameters since, WSS was found statistically significant higher in AP BAV if compared to RL BAV. Even aortic morphology was identified as responsible for changes in WSS distribution with higher WSS values for AR aorta if compared to TA.

Reference

1. Hope, M.D., et al., *Bicuspid Aortic Valve: Four-dimensional MR Evaluation of Ascending Aortic Systolic Flow Patterns 1*. Radiology, 2010. **255**(1): p. 53-61.
2. Schaefer, B.M., et al., *The bicuspid aortic valve: an integrated phenotypic classification of leaflet morphology and aortic root shape*. Heart, 2008. **94**(12): p. 1634-1638.
3. Kang, J.-W., et al., *Association between bicuspid aortic valve phenotype and patterns of valvular dysfunction and bicuspid aortopathy: comprehensive evaluation using MDCT and echocardiography*. JACC: Cardiovascular Imaging, 2013. **6**(2): p. 150-161.
4. Gasser, T.C., R.W. Ogden, and G.A. Holzapfel, *Hyperelastic modelling of arterial layers with distributed collagen fibre orientations*. Journal of the royal society interface, 2006. **3**(6): p. 15-35.
5. Morbiducci, U., et al., *In vivo quantification of helical blood flow in human aorta by time-resolved three-dimensional cine phase contrast magnetic resonance imaging*. Annals of biomedical engineering, 2009. **37**(3): p. 516-531.
6. Morbiducci, U., et al., *Helical flow as fluid dynamic signature for atherogenesis risk in aortocoronary bypass. A numeric study*. Journal of biomechanics, 2007. **40**(3): p. 519-534.
7. Grigioni, M., et al., *A mathematical description of blood spiral flow in vessels: application to a numerical study of flow in arterial bending*. Journal of biomechanics, 2005. **38**(7): p. 1375-1386.

Nome file: Chapter 5_last.docx
Directory: C:\Users\Dell\Dropbox\Tesi AR\Tesi\almost final\capitoli
modificati dal 17_12_2015\definitivi 04-01-2015
Modello: C:\Users\Dell\AppData\Roaming\Microsoft\Templates\Normal.dot
m
Titolo:
Oggetto:
Autore: Antonino Rinaudo
Parole chiave:
Commenti:
Data creazione: 1/7/2016 12:29:00 AM
Numero revisione: 3
Data ultimo salvataggio: 1/7/2016 11:46:00 AM
Autore ultimo salvataggio: Antonino Rinaudo
Tempo totale modifica 12 minuti
Data ultima stampa: 1/7/2016 11:46:00 AM
Come da ultima stampa completa
Numero pagine: 22
Numero parole: 3,154 (circa)
Numero caratteri: 17,980 (circa)

Dear Award Committee,

the participation to the 21st Congress of the European Society of Biomechanics would be for me an incredible opportunity to growth from a personal and professional point of view. It is my opinion that the work I am going to present to the Congress audience will be of great interest and through a process of idea exchange (i.e. brain storming), with the other participants to the Congress, we could come out with some new projects or cooperation.

For all the aforementioned reasons I am applying for a travel award and thus I please you to consider my application.

I am looking forward to hearing from you,

Antonino

Ph.D. Student,

Department of Chemical, Industrial, Informatics and Mechanical Engineering,

Università degli Studi di Palermo

Mobile: +39 3893468454

Email: antonino.rinaudo@unipa.it ; antonino.rinaudo@gmail.com

Skype: antonino.rinaudo

Chapter 6

FSI applied to penetrating ulcer

6.1. Introduction

Penetrating atherosclerotic ulcer (PAU) is a condition characterized by an atheromatous plaque that ulcerates and disrupts the internal elastic lamina of the aortic wall; it extends to the medial layer and is associated with a variable amount of aortic wall hematoma. Patients with PAU that present symptoms are treated with endovascular procedure with the implant of a stent graft[1].

Although PAUs may simply represent variants of aortic dissection or intramural hematoma, several studies indicate that there may be differences in the clinical behavior of these diseases [2],[3],[4] that lead to an objective difficulties in PAU diagnosis. PAU onset is characterized by an ulcer that develops in patients with advanced atherosclerosis. Clinical PAU course may follow three different ways; PAU may form an intramural hematoma or a false aortic aneurysm or worst

lead to aortic wall rupture. Aortic rupture related to PAU has an incidence as high as 40% that is almost 6-fold higher than rupture rate related to type B aortic dissection (i.e. 7%).

In this work, the FSI model, described in the previous chapters, was applied to the case of a PAU for the identification of those parameters that may predict PAU evolution. Specifically, hemodynamic loads exerted on the aortic wall of both pre- and post-repair model were estimated using steady and unsteady fluid dynamic simulations using FLUENT v13.0.0 (ANSYS Inc., Canonsburg, PA). Structural analyses were performed using ABAQUS v6.12 (SIMULIA Inc, Providence, RI) software to assess the stress distribution around the PAU, and were coupled to CFD analyses with the software MpCCI v4.2 (Fraunhofer SCAI, Germany).

6.2. Experimental Procedure

This study was conducted on a 3D model geometry reconstructed from CT of a patient admitted and diagnosed with a ruptured PAU.

The patient was a 66 year-old man admitted to our local hospital for sudden onset of chest pain radiating to the back and inter-scapular region. A contrasted CT scan confirmed a ruptured PAU distal to the left subclavian artery, with a large intramural hematoma involving the thoracic aorta and the distal aortic arch.

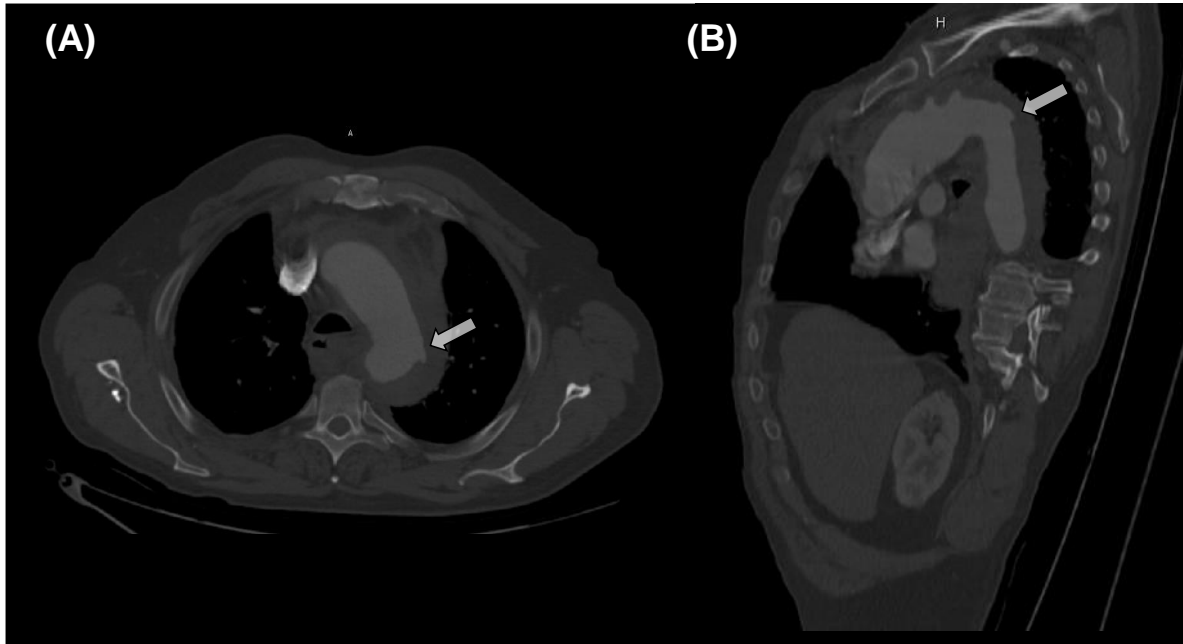


Figure 6.1: Normal axial CT image (A) and oblique image (B) of the patient with PAU; the arrows indicate the position of the ulcerating lesion.

After diagnosis, the patient underwent an emergent endovascular intervention to implant a 42-150 mm thoracic endo-prosthesis (Talent®, Medtronic, CA, USA) and seal the ruptured PAU.

The 3D aortic arch geometry created in our model was segmented from the patient's CT data using the vascular modeling toolkit VMTK v0.9.0 (<http://www.vmtk.org>). The aorta 3D anatomy was modeled from the aortic valve, through the ascending aorta, the aortic arch and supra-aortic vessels (i.e., innominate artery, left common carotid artery, left subclavian artery) and the descending aorta, ending at the level of the diaphragm.

The geometry of the stent graft, extracted from the post-repair patient's CT scan, was modeled as a tubular protrusion into the aortic arch. The protrusion geometry was defined by two parameters: i) the protrusion extension, defined as the length of TASG protrusion not in contact with the aortic wall, and ii) the angle between the lesser curvature of the aorta and the protruded segment of the stent graft wall. The stent graft was placed into the 3D model as it appeared in the CT images of the patient following PAU repair, using the surgical planning and anatomical editing tools.

Computational analyses were executed by coupling, by mean of MpCCI v4.2 (Fraunhofer SCAI, Germany), a structural solver, ABAQUS v6.12 (SIMULIA Inc, Providence, RI), and a CFD solver, FLUENT v13.0.0 (ANSYS Inc., Canonsburg, PA).

For structural analysis, aortic wall was assumed to be 1.72 mm thick and, following the constitutive model developed by Raghavan et al. [5], was modeled as an incompressible, hyperelastic, homogeneous and isotropic material.

6.3. Results

In this study, FSI modeling was applied to quantify the role of the hemodynamic and structural loads exerted on the PAU lesion and to assess the potential causative factors leading to blood penetration and progression of the lesion.

Map of pressure, obtained from CFD analyses post-processing, shown, for peak systole, a maximum value of pressure (117 mmHg), induced by the penetrating ulcer, in proximity of the bulged aortic wall. In the same spot and at the same aortic region, a lower value of wall principal stress (120 kPa), if compared to ascending aorta and surrounding aortic regions, is highlighted.

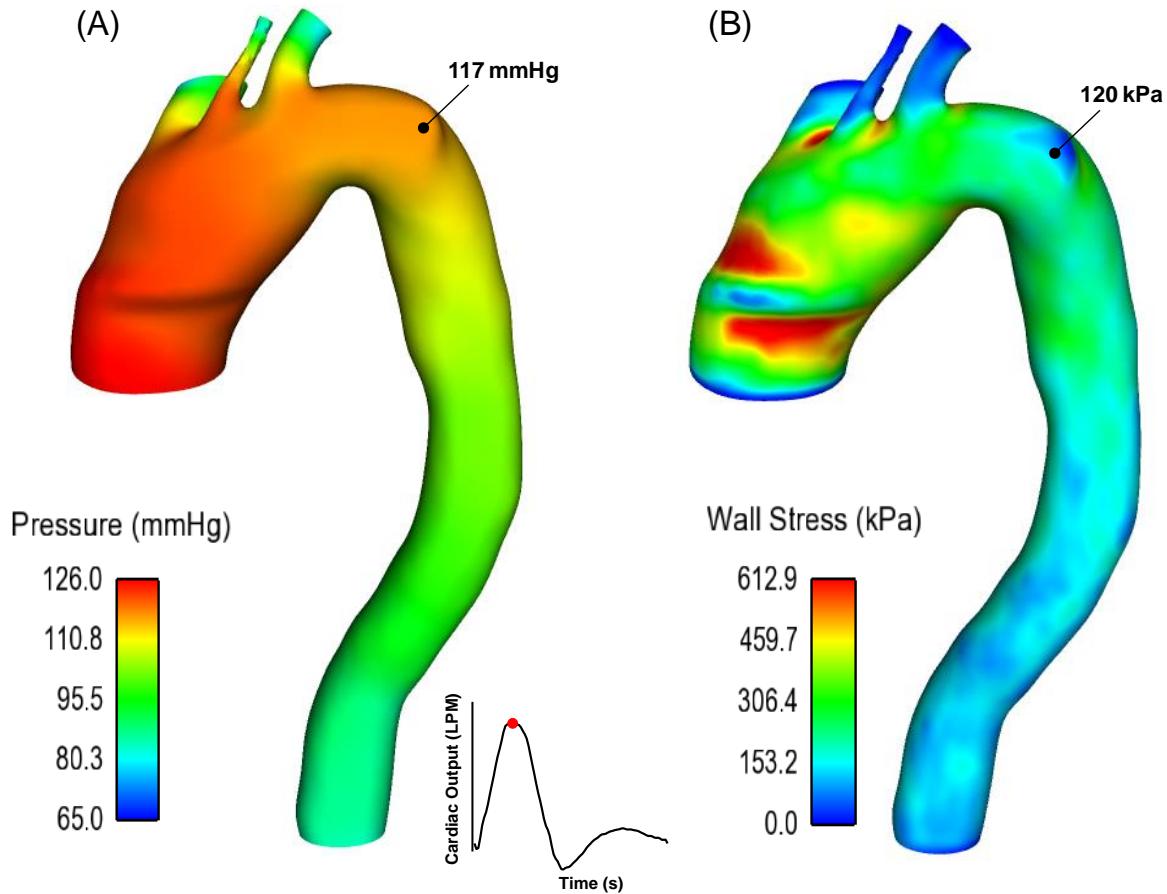


Figure 6.2: Distribution of pressure (A) and Wall Stress at peak of systole in correspondence of PAU.

Hemodynamic characteristics are illustrated using both streamlines and distribution of blood velocity on the aortic wall (Figure 6.2). Blood velocity was high in proximity of the supra-aortic vessels since blood flew through narrow spaces; at the contrary, velocity was low in proximity of the PAU region where its magnitude is 0.15 m/s. Specifically, during systolic phase, blood streamlines were well organized with parallel streamlines spanning the ascending aorta and without particular eddies.

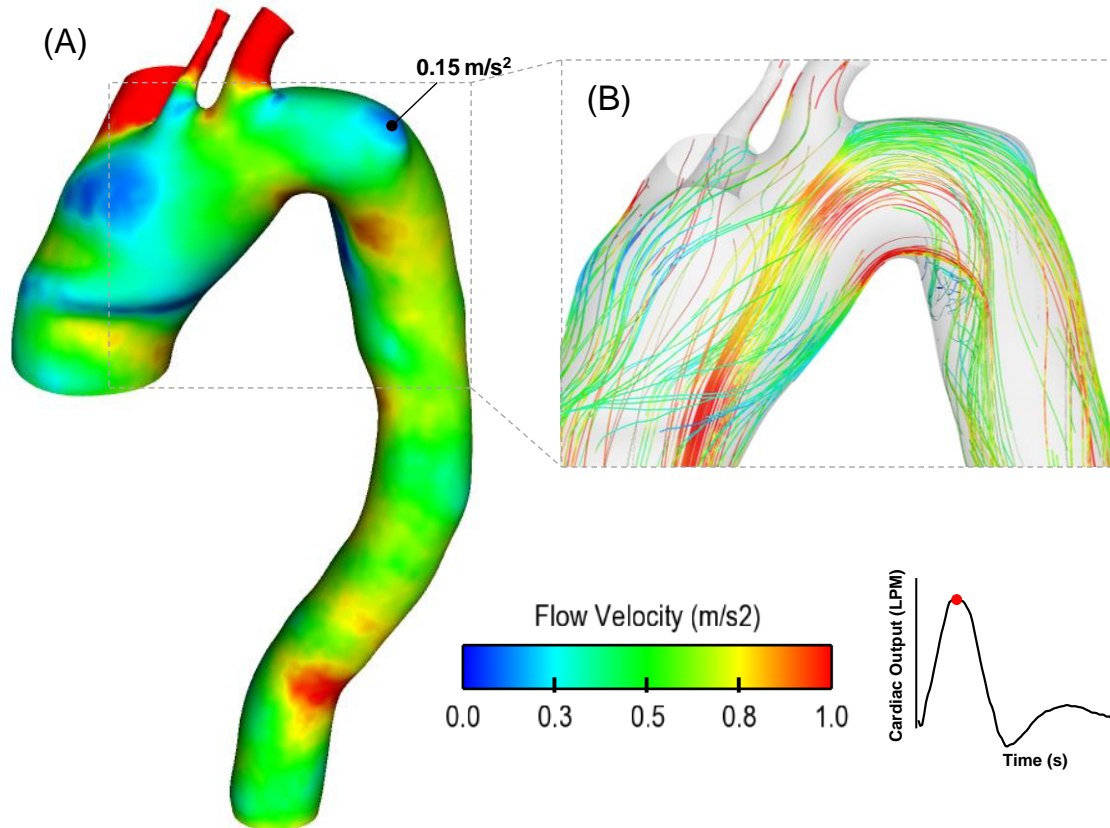


Figure 6.3: Distribution of blood velocity at aortic wall (A) and particular of velocity streamlines at peak of systole in correspondence of PAU.

Shear forces exerted on aortic intimal layer were also studied by the extrapolation of time-averaged wall shear stress (TAWSS) and the OSI. Specifically, TAWSS was low in the region proximal to PAU with a minimum value of 1.24 N/m^2 while OSI, in the same region, reached a pick regional value equal to 0.13. The high value of OSI suggested reversal flow in proximity of the onset of ulcerating lesion.

As expected, near the onset of PAU lesion, the post-repaired aorta exhibited lower magnitude of blood pressure compared to that of pre-repaired aortic model. The TAWSS increased to 1.6 N/m^2 while OSI reduced to 0.085. In contrast, velocity streamlines lost their characteristic laminar pattern to show complex flow in the proximal luminal surface of the stent graft.

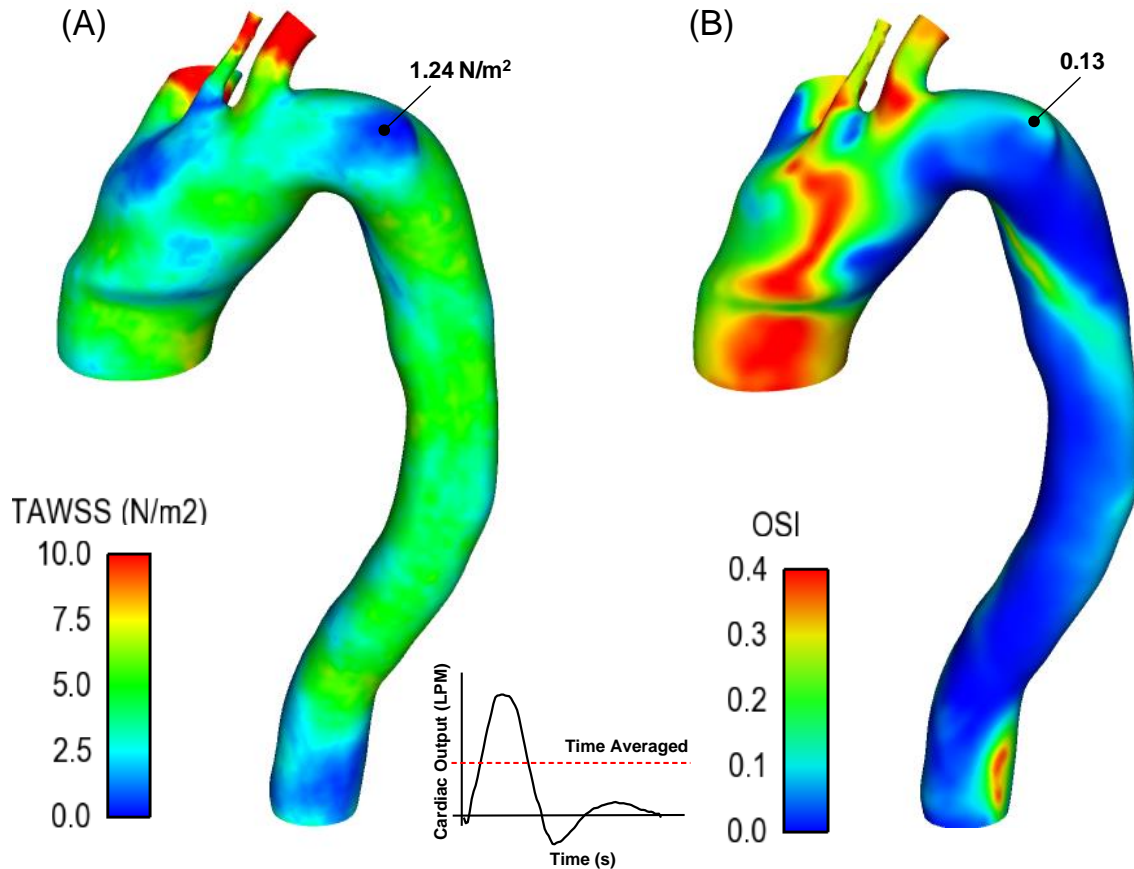


Fig. 6.4 Distribution of TAWSS (A) and OSI (B) over cardiac cycle.

6.4. Conclusion

The aim of our study was to assess the hemodynamic and the wall loads in the aortic region proximal to PAU by mean of FSI analyses on patient specific geometries. The present study demonstrated that FSI analyses could be used to identify PAUs at higher risk of developing intramural hematoma or dissection.

- Region close to PAU experiences low blood velocity and high intraluminal pressure. This particular condition was found in previous studies about saccular aneurysms [6] and was indicated as predisposing to aneurysm progression and enlargement.

- The region of greater curvature of the aortic wall just distal to the left subclavian artery is interested by hemodynamic disturbance more than other aortic region. Specifically, low shear stress (i.e. TAWSS) and high shear stress index (i.e. OSI) were found in PAU region and this can be suggestive of mechanical damage.
- It is generally assumed that a TAWSS of 2.0 N/m^2 is suitable for maintaining the structure of the vessel, and a value lower than 1.5 N/m^2 will degenerate endothelial cells via the apoptotic cell cycle. In our study, the shear stress in the PAU regions was barely 1.24 N/m^2 and the PAU had in fact ruptured.

References

1. Pauls, S., et al., *Endovascular repair of symptomatic penetrating atherosclerotic ulcer of the thoracic aorta*. European journal of vascular and endovascular surgery, 2007. **34**(1): p. 66-73.
2. Hirschl, D. and R.J. Dym, *Penetrating Atherosclerotic Ulcer*. Cardiac Imaging, 2014: p. 72.
3. Cho, K.R., et al., *Penetrating atherosclerotic ulcer of the descending thoracic aorta and arch*. The Journal of Thoracic and Cardiovascular Surgery, 2004. **127**(5): p. 1393-1401.
4. Macura, K.J., et al., *Pathogenesis in acute aortic syndromes: aortic dissection, intramural hematoma, and penetrating atherosclerotic aortic ulcer*. American journal of roentgenology, 2003. **181**(2): p. 309-316.
5. Raghavan, M. and D.A. Vorp, *Toward a biomechanical tool to evaluate rupture potential of abdominal aortic aneurysm: identification of a finite strain constitutive model and evaluation of its applicability*. Journal of biomechanics, 2000. **33**(4): p. 475-482.
6. Jeong, W. and K. Rhee, *Hemodynamics of cerebral aneurysms: computational analyses of aneurysm progress and treatment*. Computational and mathematical methods in medicine, 2012. **2012**.

Chapter 7

CFD analyses to assess dissected aorta perfusion and predict negative outcome

7.1. Introduction

AoD is a life-threatening TAA complication, in which the blood penetrates the aortic wall via a tear in the intimal layer. A dissected aorta presents two separate lumen, the original lumen (i.e. true lumen) and a new lumen (i.e. false lumen) generated by the flowing blood into the aortic wall. It has been demonstrated that the application of baseline morphological imaging variables does not describe completely the complex hemodynamic implication in type B AoD.

Morphological variables, such as entry points dimension and proximal/distal location as well as FL patency, have been recently indicated as predictor of type B AoD adverse outcome[1-5]. Additionally, hemodynamic variables, such as flow rate and pattern in FL and TL as well as WSS, obtained from CFD analyses, should be considered. It has been studied that hemodynamic variables influence aortic dissection outcome; specifically, blood pressure has effects on aortic

dilatation and on increasing in circumferential pressure on aortic wall while WSS affects endothelial cell function and deteriorates aortic wall[6-8].

The aim of this study was to assess the hemodynamic in patient specific aortic geometries with type B aortic dissection and to evaluate the influences of tear morphology on blood flow patterns. The initial hypothesis was that the amount of blood flowing in a patent FL, dependent on entry tear morphology, may have a predictive value in differentiating patients for whom a surgical management may be beneficial. The initial hypothesis was tested with CFD analyses executed on patient specific geometries.

7.2. Procedure

We collected radiological imaging of patients with type B aortic dissection from our local hospital registry. The studied accounted for 225 patients, enrolled from January 2007 and July 2013, for whom CT scans were performed at initial in-hospital admission.

In 15 patients, a residual Type B AoD occurred after a successful surgical repair of a Type A AoD (i.e., the group termed Type A → Type B). These patients exhibited, as the group with native Type B AoDs, the main proximal tear in proximity of aortic arch or distal to the left subclavian artery (LSA). These patients were clinically treated as native Type B dissections [9].

According to the outcome, all patients were therefore separated into three groups: acutely complicated (AC), aneurysm evolution (AE) and uncomplicated AoD (UN).

For each patients, several geometrical parameter were considered (see Figure 7.1): a) entry tear or main proximal communication between true and false lumina height, defined as the distance between the upper and lower margins of the entry tear. b) Position of entry tear as function of the distance from the ostium of LSA. c) Width of entry tear. d) Number of re-entry tears as well as their heights and widths as defined for entry tears. (e) Ratio between the true and false luminal area as well as the FL area were also calculated.

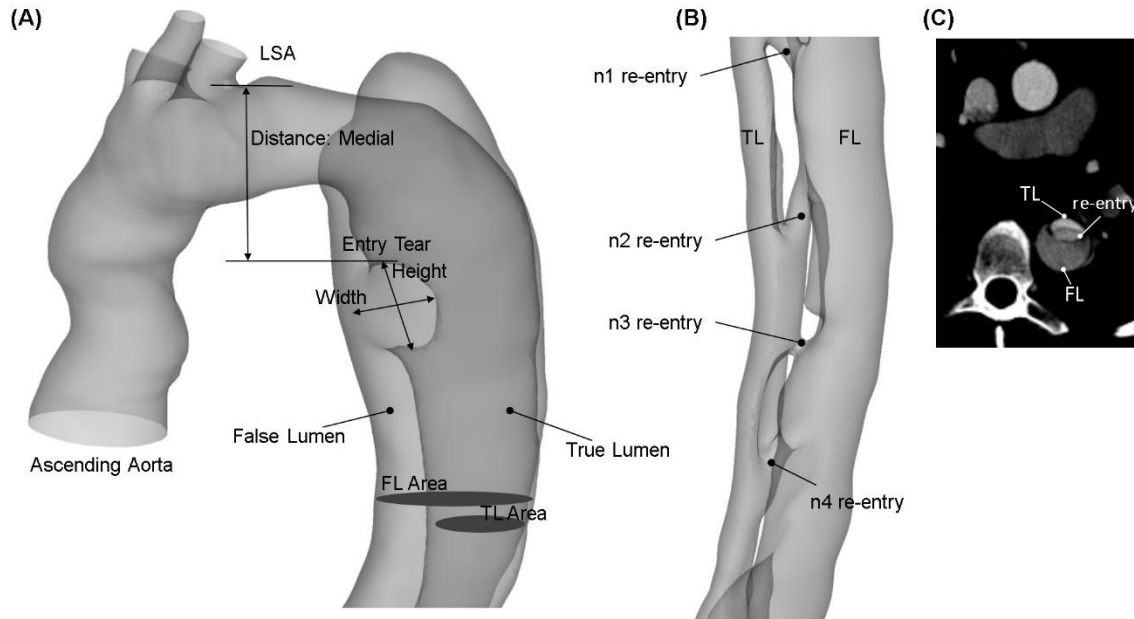


Figure 7.1 (A) Representative aortic Type B AoD model demonstrating parameters measured; (B) particular of a descending aorta showing multiple re-entry tears; (C) axial slice of CT scan showing re-entry tear communications between TL and FL

7.3. CFD analyses

CTA scans of AoD were retro-reconstructed using the vascular modeling toolkit VMTK (<http://www.vmtk.org>). Images were segmented from the ascending aorta, through the aortic arch, the supra-aortic vessel and the descending aorta. Entry and multiple re-entry tears were also reconstructed with the aid of the aortographies and the guide of our clinicians. Specifically, aortographies with contrast liquid were used to detect the flow entering FL by X-rays and thus to individuate the position and number of re-entry tears, which appear in CT scans as a third channel running parallel and between FL and TL (see Figure 7.1). However, CT scans did not allow us to reconstruct small-sized flow communications between false and true lumina. FL was considered as a separate outlet for AoDs running parallel to the TL without presenting a re-entry tear before the iliac bifurcation. However, this was observed in only one patient.

As described in the previous chapters, the 3D geometries reconstructed were discretized into a set of small elements to create a computational mesh. The mesh consists of a 1 million of unstructured tetrahedral elements, approximately. Thus, hemodynamic was evaluated by unsteady

computational fluid dynamic simulations using the commercial finite-element package FLUENT v14.0.0 (ANSYS Inc., Canonsburg, PA).

In CFD analyses of large vessel, blood flow is modelled as laminar but in AoD analyses, lumen diameter is reduced if compared to normal aorta and thus may lead to turbulent condition. However, Reynolds number obtained in this analyses were 1302 at ascending aorta, 2171 at FL inflow and 895 at FL outflow; these finding gave the possibility to work with a laminar flow.

The following hemodynamic variables for each simulation were evaluated. (a) The FL pressure index (FPI%), which was measured in a cross section of descending aorta just after the proximal entry tear at systole, was calculated as $FPI\% = (FL \text{ systolic pressure} / TL \text{ systolic pressure}) \times 100$ according to Tsai et al [10]. (b) The FL flow rate was computed as $FL \text{ flow } (\%) = (FL \text{ flow} / (TL \text{ flow} + FL \text{ flow})) \times 100$. The time-averaged pressure distribution and WSS over one cardiac cycle were shown for representative models of dissected aortas.

Follow-up was used to assess whether differences exist in the hemodynamic data over time. Therefore, computational flow analyses were also performed for each patient's follow-up (i.e., additional twenty-five CFD analyses). Given the short follow-up, FL flow and FPI did not show any remarkable difference over time so that results of each patient were shown as the average data between initial admission and follow-up.

7.4. Results

CFD study of AoD geometries is more complex than that of healthy or aneurysmal aortas due to the presence of two lumens and the several connections between them.

Entry tear was frequently observed on the outer curvature of the descending thoracic aorta whereas multiple re-entry tears were found in 10 patients with patent FL. Entry tear height <10mm was found in 8 patients, and most of them had a residual Type B AoD after surgical resection of a Type A AoD.

In figure 7.2 the blood pattern of 4 patients that suffered for different dissection related complication were plotted. Subjects 1, 13 and 14 shown an increasing in blood velocity when blood flowed through the entry tear region and then decelerated to form a zone of elevated number

of vortices. Adversely, blood accelerated in the zone distal to the re-entry point when the FL blood met the TL blood.

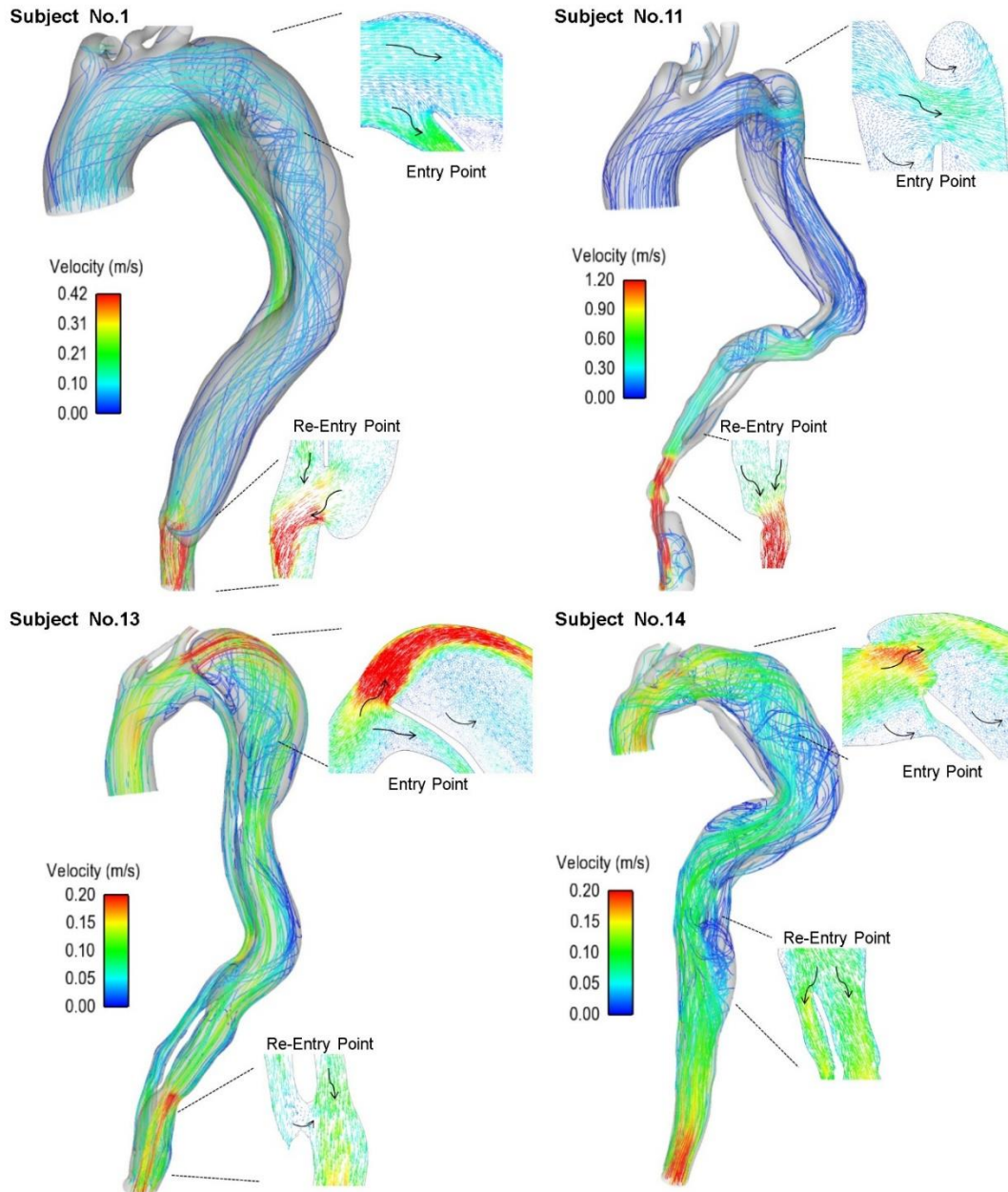


Figure 7.2 Time-averaged velocity streamlines of blood flow over one cardiac cycle for different Type B AoDs; Subject No. 1 with Type B AoD complicated by aneurysm evolution; Subject No. 11 with acutely complicated Type B AoD; Subject No. 13 with Type B AoD complicated by aneurysm evolution; Subject No. 14 with Type A → Type B AoD complicated by aneurysm evolution

An entry tear proximal to the LSA induced an impinging flow on the inner FL wall whereas a distal entry tear determined a slower-moving flow with vortexes nested in the upper FL region (compare Subject No. 11 to Subjects No. 1, 13, 14). Dimension of FL influenced blood flow and it was observed that in larger FL blood decelerated until reach a steady state condition during the entire cardiac cycle leading to a higher risk of thrombus formation. Moreover, figure 7.2 shown that blood flowing into TL followed a less complicated pathway if compared to that flowing into FL; additionally, TL blood did not form recirculating vortexes.

Maps of blood pressure (Figure 7.3) for 6 patients with AoD shown high blood pressure in ascending thoracic aorta; moreover, descending aorta suffered high mean pressure over cardiac cycle, most likely due to flow impingement into entry tear region. Pressure values dropped to lower magnitudes when blood flowed in TL and FL. However, pressure distributions and values changed depending on AoD geometries and FL or TL morphologies.

Patient with multiple entry/re-entry points, No.2 and No. 16, shown a more homogeneous pressure distribution in both of the two lumina; moreover, the differential pressure among TL and FL were negligible for these patients resulting into a FPI close to 100%. Patient No. 9 suffered of a Type B AoD acute complication with organ malperfusion that resulted also by CFD analyses where was observed a remarkable pressure drop in correspondence of the narrowed FL area close to celiac trunk.

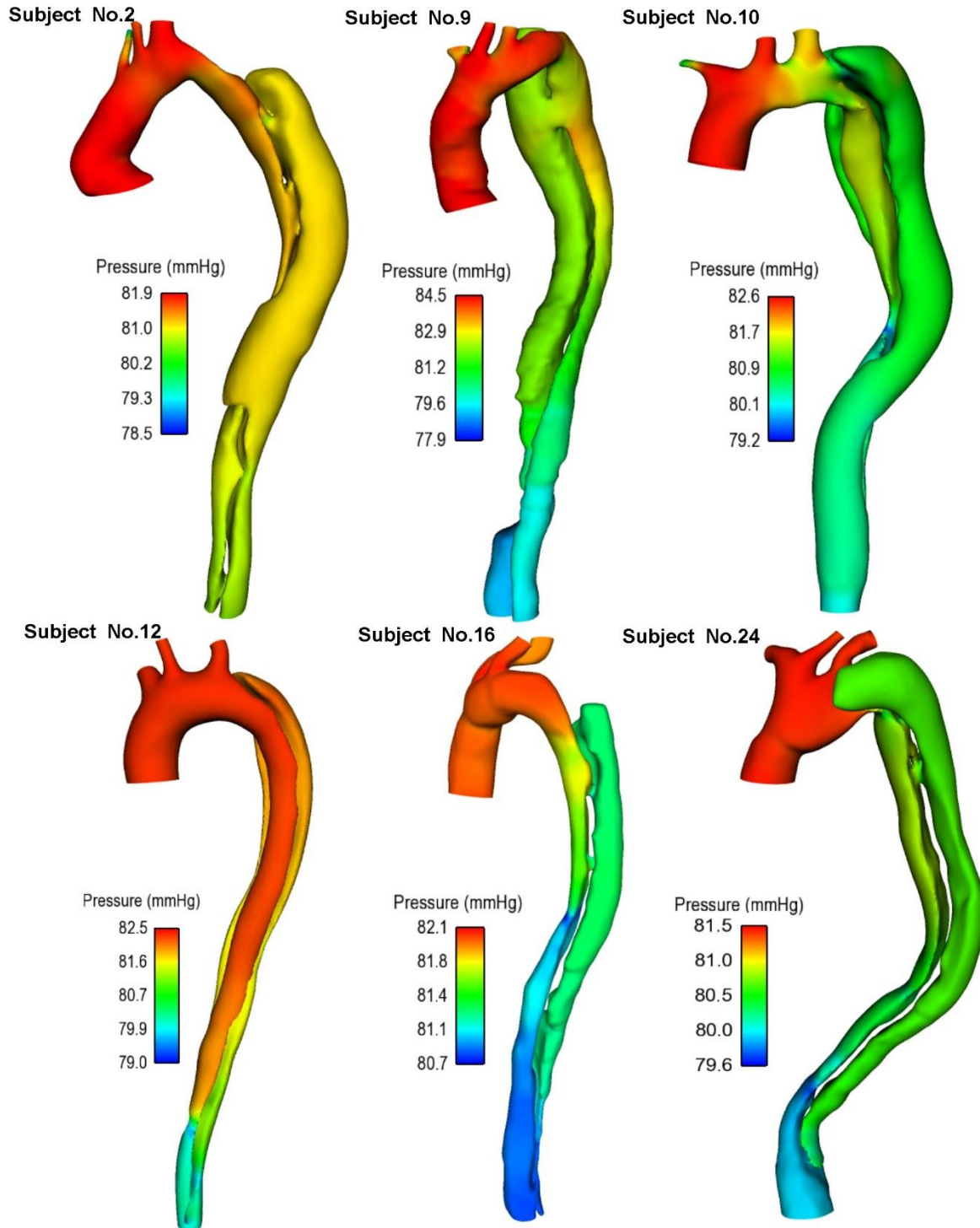


Figure 7.3 Time-averaged pressure distribution over one cardiac cycle for different Type B AoDs; Subject No. 2 with Type A → Type B AoD complicated by aneurysm evolution; Subject No. 9 with Type B AoD complicated by aneurysm evolution; Subject No. 10 with uncomplicated Type A → Type B AoD; Subject No. 12 with acutely complicated Type B AoD; Subject No. 16 with

uncomplicated Type A → Type B AoD; Subject No. 24 with uncomplicated Type A → Type B AoD

The distribution of TAWSS was studied over the cardiac cycle and over time, for each patients, to evaluate the most vulnerable regions. Not remarkable differences were observed between initial in-hospital admission and follow-up since the study was conducted over a short period of time and thus the geometries studied, for each patient, were similar over time.

Figure 7.4 shown that the entry and re-entry point regions were those exposed to high TAWSS were the blood was accelerated and velocity was high. More in detail, the re-entry point regions appeared also more exposed to high TAWSS than entry-point region, suggesting particular attention to those locations.

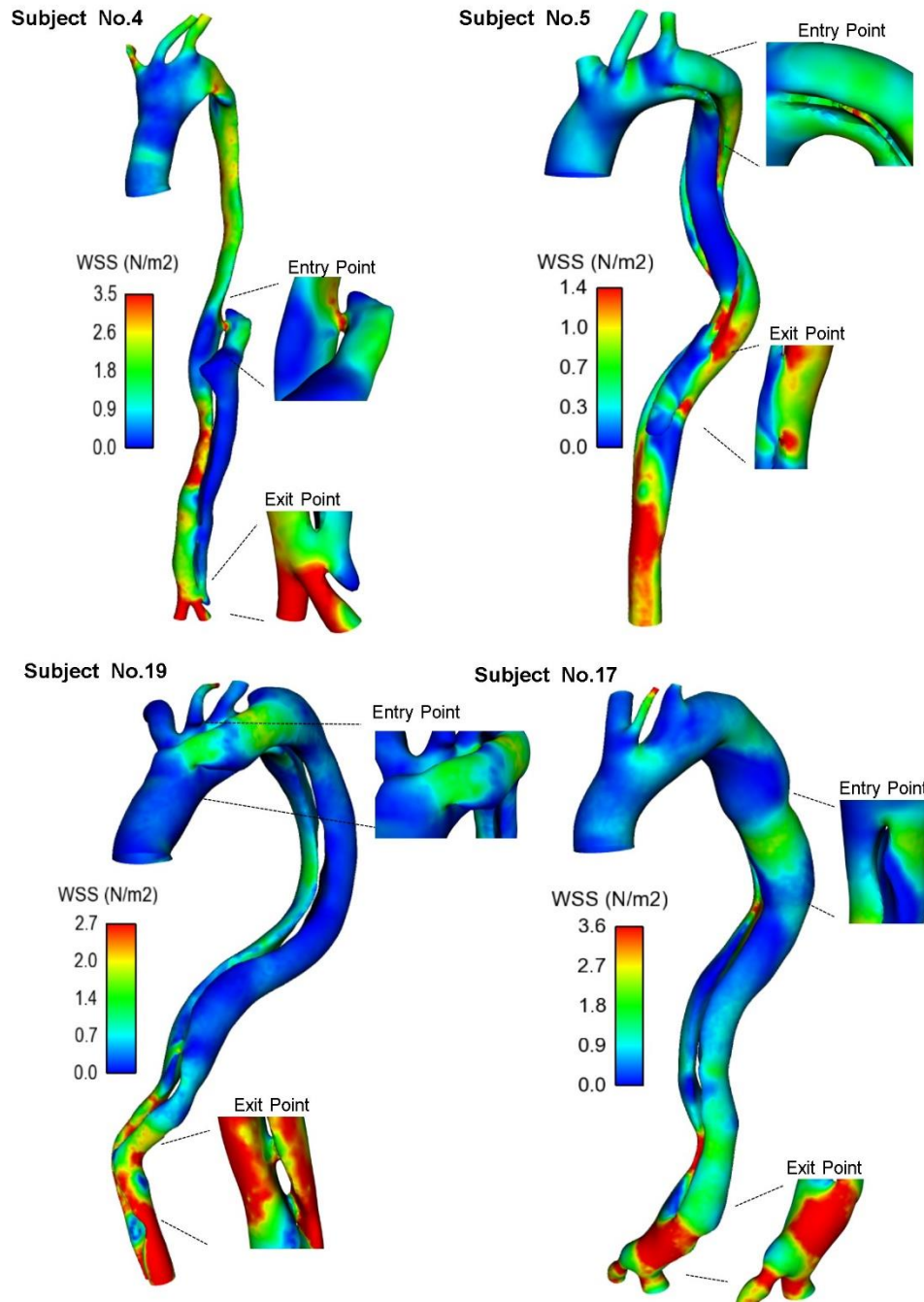


Figure 7.4 Time-averaged WSS distribution for different Type B AoDs; Subject No. 4 with Type B AoD complicated by aneurysm evolution; Subject No. 5 with acutely complicated Type B AoD; Subject No. 9 with FL thrombosis and Type B AoD complicated by aneurysm evolution; Subject No. 19 with uncomplicated Type A → Type B AoD

The WSS reduced greatly in the TL wall and close to the aortic arch (i.e., Subject No. 5 and 17). Partial thrombosis of upper descending aorta drastically decreased WSSs due to low blood likely flowing through the FL (i.e., Subject No. 4). Regions of low WSS (i.e., <0.4 Pa), observed along descending aorta, may suggest atherosclerotic plaque formation as observed clinically.

A strong correlation between entry tear height and FL flow rate was found with low flows associated with reduced height entry tears (i.e., FL Flow=31.6% for tear height <10 mm, $n=8$, and FL Flow=64.5% for tear height ≥ 10 mm, $n=17$, $p < 0.001$, Figure 7.5).

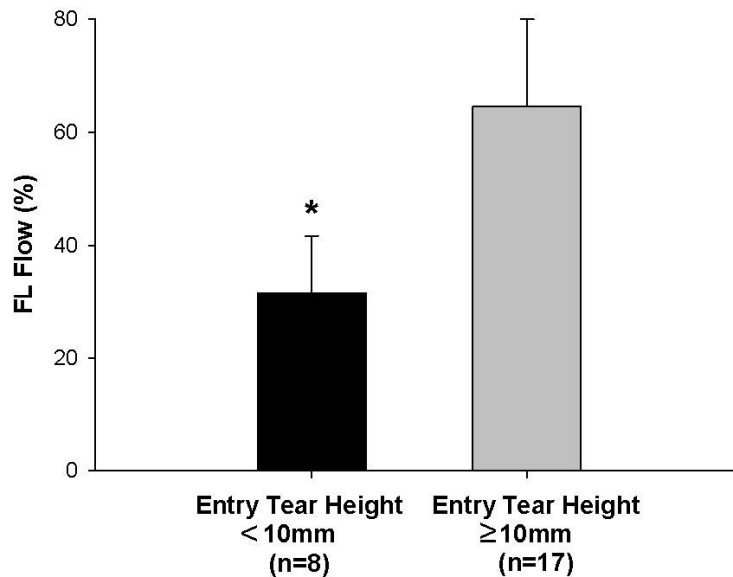


Figure 7.5 Comparison of FL Flow rate between small and large entry tear heights where the cutoff was a value ≥ 10 mm; * significantly different from entry tear height ≥ 10 mm ($p < 0.05$)

However, no statistical difference was found between acute complicated or uncomplicated patients with AoDs with either entry tear height less or more than 10 mm.

Person's correlation showed that FL flow is the only hemodynamic variable related to anatomical ones. More in detail, FL flow was statistically related to:

- Entry tear location ($R = -0.46$, $p = 0.025$, $n = 25$).
- Entry tear height ($R = 0.66$, $p = 0.001$, $n = 25$).
- Entry tear width ($R = 0.41$, $p = 0.038$, $n = 25$).
- FL area ($R = 0.39$, $p = 0.049$, $n = 25$).

- TL/FL area ($R=-0.49$, $p=0.013$, $n=25$)

At multiple regression for all patients, entry tear height was the sole independent determinant that statistically predicted FL flow rate ($p=0.046$, $OR=1.18$, $95\% CI: 0.023-2.338$). Specifically, FL flow rate increases directly with the entry tear height of Type B AoDs.

7.5. Conclusion

Aim of this study was to assess the hemodynamic inside type B AoDs with the application of CFD analyses to patient specific geometries.

The results obtained demonstrated a strong relationship between the entry tear height and the blood flow rate inside the FL. In a different way, it is possible to consider the entry tear height as a significant predictor of the volume of blood flowing into a patent FL; specifically, as wider is the entry tear as bigger is the amount of blood that perfuse the FL. This hemodynamic predictor can be used to identify a high-risk subgroup of patients with Type B AoDs that may clinically benefit from early intervention.

The complex AoD geometries, do not give the possibility to associate, directly, hemodynamic variable to patient clinical outcomes. Patent and highly perfused FL is clinically associated with adverse patient outcomes suggesting a close monitoring. More in detail, among the patients studied, those experiencing low FL flow rate had a type B AoD evolved into chronic aneurysms (i.e. 9 patients) while those with highly perfused FL were uncomplicated or acutely complicated (i.e. 10 and 6 patients, respectively).

FL abnormally disturbed flow may cause physiological changes in the vessel wall including wall remodeling, flow resistance and inflammation. The synergy of abnormal blood flow patterns and excessive hemodynamic stresses increase the risk of aneurysm formation, growth or rupture [8, 11-13].

Different blood pathway and velocity between FL and TL result in an impaired balance between the pressures of these lumina. Moreover, reduced flow velocity in FL increases the pressure and consequently the load on the dissected wall increasing the risk of aortic dilatation and rupture. Cyclic high pressure has detrimental effects since it may lead to elasticity change in FL wall due to loss of muscle cells and collagen accumulation[8].

Another hemodynamic factor influencing aortic wall properties is the WSS that has been indicated as an important regulator of vascular homeostasis; specifically, low WSS and highly deflected flow increase the risk of wall inflammation and weakening [6, 7] while high WSS and laminar flow promote endothelial cell functions and tissue integrity. In this study, the blood flowing inside FL was slower than that in TL and has a recirculating pathway. This introduce a mechanism of damaging to cell-cell junctions or cell surface integrity. In proximity of the entry tear WSS has detrimental effects since it assumes elevated values and may contribute to initial tear propagation. In conclusion, results from computational flow analysis may be combined with imaging technique to identify patient at greater risk of dissection-related complications and to improve the management of patients with AoDs.

Reference

1. Bernard, Y., et al., *False lumen patency as a predictor of late outcome in aortic dissection*. The American journal of cardiology, 2001. **87**(12): p. 1378-1382.
2. Moon, M.R., et al., *Does the extent of proximal or distal resection influence outcome for type A dissections?* The Annals of thoracic surgery, 2001. **71**(4): p. 1244-1249.
3. Hao, Z., et al., *Endovascular stent-graft placement or open surgery for the treatment of acute type B aortic dissection: a meta-analysis*. Annals of vascular surgery, 2012. **26**(4): p. 454-461.
4. Elefteriades, J.A., *Natural history of thoracic aortic aneurysms: indications for surgery, and surgical versus nonsurgical risks*. The Annals of thoracic surgery, 2002. **74**(5): p. S1877-S1880.
5. Evangelista, A., et al., *Long-Term Outcome of Aortic Dissection With Patent False Lumen Predictive Role of Entry Tear Size and Location*. Circulation, 2012. **125**(25): p. 3133-3141.
6. Sakamoto, N., et al., *Effect of spatial gradient in fluid shear stress on morphological changes in endothelial cells in response to flow*. Biochemical and biophysical research communications, 2010. **395**(2): p. 264-269.
7. Shaaban, A.M. and A.J. Duerinckx, *Wall shear stress and early atherosclerosis: a review*. American Journal of Roentgenology, 2000. **174**(6): p. 1657-1665.
8. Gimbrone, M.A., et al., *Endothelial dysfunction, hemodynamic forces, and atherogenesis*. Annals of the New York Academy of Sciences, 2000. **902**(1): p. 230-240.
9. Kato, M., et al., *Determining surgical indications for acute type B dissection based on enlargement of aortic diameter during the chronic phase*. Circulation, 1995. **92**(9): p. 107-112.
10. Tsai, T.T., et al., *Tear size and location impacts false lumen pressure in an ex vivo model of chronic type B aortic dissection*. Journal of vascular surgery, 2008. **47**(4): p. 844-851.
11. Pasta, S., et al., *Difference in hemodynamic and wall stress of ascending thoracic aortic aneurysms with bicuspid and tricuspid aortic valve*. Journal of biomechanics, 2013. **46**(10): p. 1729-1738.

12. Dolan, J.M., J. Kolega, and H. Meng, *High wall shear stress and spatial gradients in vascular pathology: a review*. *Annals of biomedical engineering*, 2013. **41**(7): p. 1411-1427.
13. Clough, R.E., et al., *A new imaging method for assessment of aortic dissection using four-dimensional phase contrast magnetic resonance imaging*. *Journal of vascular surgery*, 2012. **55**(4): p. 914-923.

Chapter 8

Towards the evaluation of the thoracic aortic stent graft failure risk related to endograft infolding

8.1. Introduction

Thoracic endovascular repair (TEVAR) has rapidly emerged in the last decades as the best treatment for a variety of thoracic aortic pathologies. TEVAR procedure, based on the repair of unhealthy aorta by endovascular implant of Thoracic Aortic Stent-Graft (TAG), presents reduced risk of paraplegia, renal insufficiency, cardiac complication and early death if compared to open surgical repair[1].

TEVAR procedure, despite its main advantages, is still challenging when applied to traumatic injuries especially in young patients[2, 3]. The reduced time related to an emergency procedure and the particular dimension of patient aortic lumen, most of the time do not allow the surgeon to find a device of the optimal size. Thus, frequently TAGs implanted in young patients, under emergency procedure, have a diameter bigger than it should be. Device oversizing may induce to

premature failure and endograft collapse/infolding with consequent hemodynamic perturbation and the necessity for a second intervention. A recent clinical study on 33,000 Gore TAG thoracic endoprosthesis (W. L. Gore and Assoc, Flagstaff, Ariz) shown a 139 cases of device failure with an incidence rate of 0.4% occurring at a median and mean follow-up of 9.5 and 76 days, respectively[4]. Of these events, 60.4% occurred in trauma patients, with an overall average of 36% device oversizing.

Depending on the particular aortic geometry (i.e. highly curved or angulated aortic arch), the device is implanted with a so called “bird-beak” configuration; this means that part of the stent is not in contact with the smaller curvature of the aortic arch. Bird-beaking is not desirable since exposes the TAG to excessive hemodynamic loads. However, we speculate that the bird-beak configuration, as an isolated event, may not necessarily be responsible for stent-graft collapse.

Thus, aim of this study was to assess the hemodynamic loads role on the collapse of an implanted stent by means of computational tools and experimental data. For this, material properties of TAG were studied by matching the infolding results from in vitro studies with the infolding data of FSI analyses.

8.2. Material and Method

The hemodynamic and the strain/stress distributions on the protruded stent-graft for four patients with mean age of 32 ± 9 years were assessed via computational analyses.

Specifically, we previously studied the mechanism of endograft collapse by studying the hemodynamic, wall stress and strain acting on the bird-beak configuration in a patient who underwent TEVAR for a traumatic aortic injury with a subsequent stent-graft collapse as previously investigated by Shukla et al. [5]. Hemodynamic parameters were studied experimentally with a pulsatile circuit like that proposed by Tsai et al. [6] used to mimic the cardiovascular system. Experimental testing were used to calibrate the global mechanical behavior of the endograft; the obtained data were used in the computational analyses of the four patients.

The pulsatile circuit consisted of four components: (1) a custom-made pulsatile pump, (2) a phantom model with the TAG device, (3) a compliance chamber, and (4) a fluid collector, all connected by silicone tubes and plastic connectors.

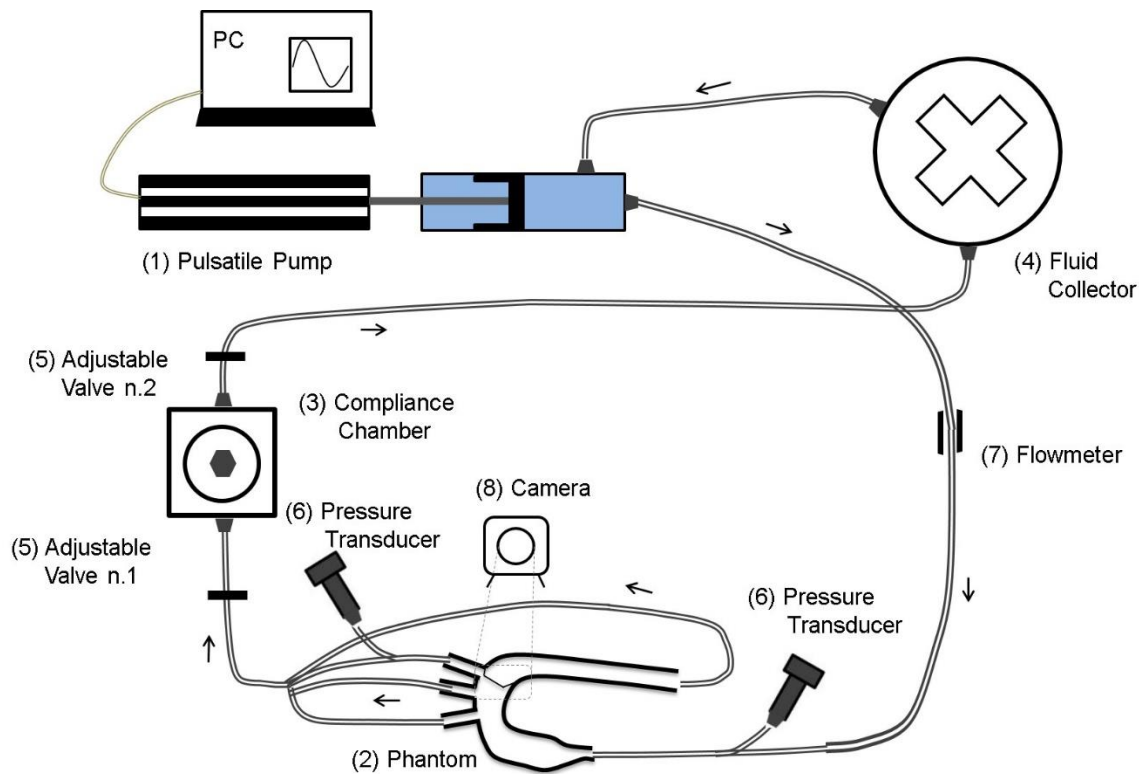


Figure 8.1: Schematic representation of pulsatile flow circuit.

8.2.1. Phantom and Flow Circuit

Three-dimensional patient-specific geometric model was reconstructed from CT scans using the vascular modelling toolkit VMTK v0.9.0 (<http://www.vmtk.org>). The reconstructed 3D geometry was used to manufacture a silicone phantom model that represented a scale 1:1 of the patients' aortic anatomy; specifically a core and an outer mold were manufactured to obtain the final model. The core mold had the same dimension of the reconstructed model and was built by the Metal Professional Company using a silicone rubber elastomer while the outer core was made of two pieces and was 2.5 mm larger than the 3D model. Core mold was placed into the outer mold and

CHAPTER 8: Towards the evaluation of the thoracic aortic stent graft failure risk related to endograft infolding

silicone was poured in the free space between them to obtain a compliant, transparent flow channel with the patient's aortic anatomy. As suggested in several studies[6, 7], silicone was used as phantom material since it, with its distensibility, allows mimicking the human aorta behavior.

A 26 mm x10 cm TAG device (TAG v1.5) was deployed inside the silicone phantom with the same position, coverage of the left subclavian artery (LSA), as that observed in the CT imaging after TEVAR. Since phantom diameter just distal to LSA was 23.6 mm, the 26 mm TAG device oversizing was 11%. Moreover, studies were also conducted with a larger TAG device (34 mm x 10 cm) to investigate the influence of a more aggressive device oversizing on the mechanism of TAG failure.

The bird-beak configuration is described by two parameters: (1) PE, that is the length of the device not in contact with the aortic wall, and (2) the angle (θ) between the aortic arch wall and the protruded stent wall. Device deployment determined a PE equal to 19 mm and an angle (θ) of 24 degree. The effect of PE was investigated with two additional configurations with fixed angle and PE = 13 mm and 24 mm.

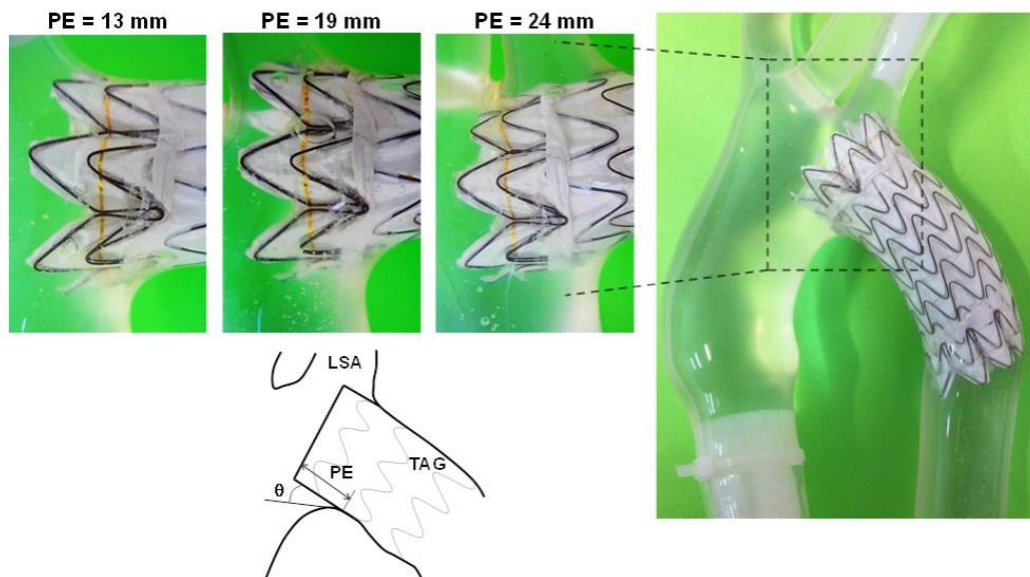


Figure 8.2: (A) Photographs of phantom model with particulars of bird-beak configurations and representation of geometric parameters used to define the TAG device protrusion geometry; (B) CT scan after TEVAR showing poor apposition of the device to the aortic wall, with a significant bird-beak (images are not at the same scale).

The pumping system consisted of a homemade pump made by a brushless linear actuator (P01-48x360F, LinMot®) connected to a piston. An electronic controller and a custom software controlled piston movements (i.e. stroke, velocity, direction). Moreover, stroke volume followed a sinusoidal waveform with stroke time depending on diastolic and systolic phase duration. The compliance chamber was projected with a spring mounted piston and variable spring rate to adjust the amount of compressed fluid and to model the Windkessel's effect. Systolic and diastolic pressures were obtained by changing valve (5) resistance and by varying the spring pre-load. The circuit was equipped with two pressure transducers (X5072 Druck, GE Measurement & Control) connected to 20G catheters (6) and thus recorded with LabVIEW software (National Instruments, Austin, TX, USA). These transducers were placed proximal to aortic inlet and distal to the left subclavian artery. Flow rate was measured with an electromagnetic flow-meter (7) (Optiflux 5300C, Krohne, Duisburg, Germany) placed at the outlet of the pulsatile pump; moreover, flow measurement were also gate at the outlet of the innominate artery and of the common carotid artery.

Endograft infolding parameters (i.e. displacements and rotations) were monitored with a high resolution CMOS camera (8) (Evo8050, SVS-Vistek, Seefeld, Germany) with a Nikon Micro-Nikkor lens (AF Micro-Nikkor 60mm f/2.8D) placed on the top of the aortic phantom model. Images were acquired and processed with the Matlab Image Acquisition Toolbox (The MathWorks, Natick, MA, USA). The accuracy of the measured TAG device displacement was 29 μm , together with a field of view of 30 x 35 mm. Images were acquired at a frame rate of 30 fps, while a ruler was used to scale images from pixels to millimeters.

8.2.2. Perfusion setting

Each bird-beak configuration (i.e. PE=13, 19, 24 mm) was perfused with different flow condition (i.e. cardiac output = 3, 5, 7 L/min) to investigate endograft infolding parameters. Several flow conditions were investigated since patient specific flow and pressure condition were not available. For the cardiac output of 5 L/min pressure were imposed as high as 120 mmHg and 80 mmHg for systolic and diastolic phase respectively; systolic duration was imposed to 330 milliseconds with a heart rate of 60 bpm. Instead, for the cardiac output of 3 L/min the pressure were 90/55 mmHg

and the heart rate was 60 bpm; in the last hemodynamic condition a cardiac output of 7 L/min with a heart rate of 70 bpm and pressure of 170/110 mmHg were imposed. All these parameters are shown in the following figure 8.3.

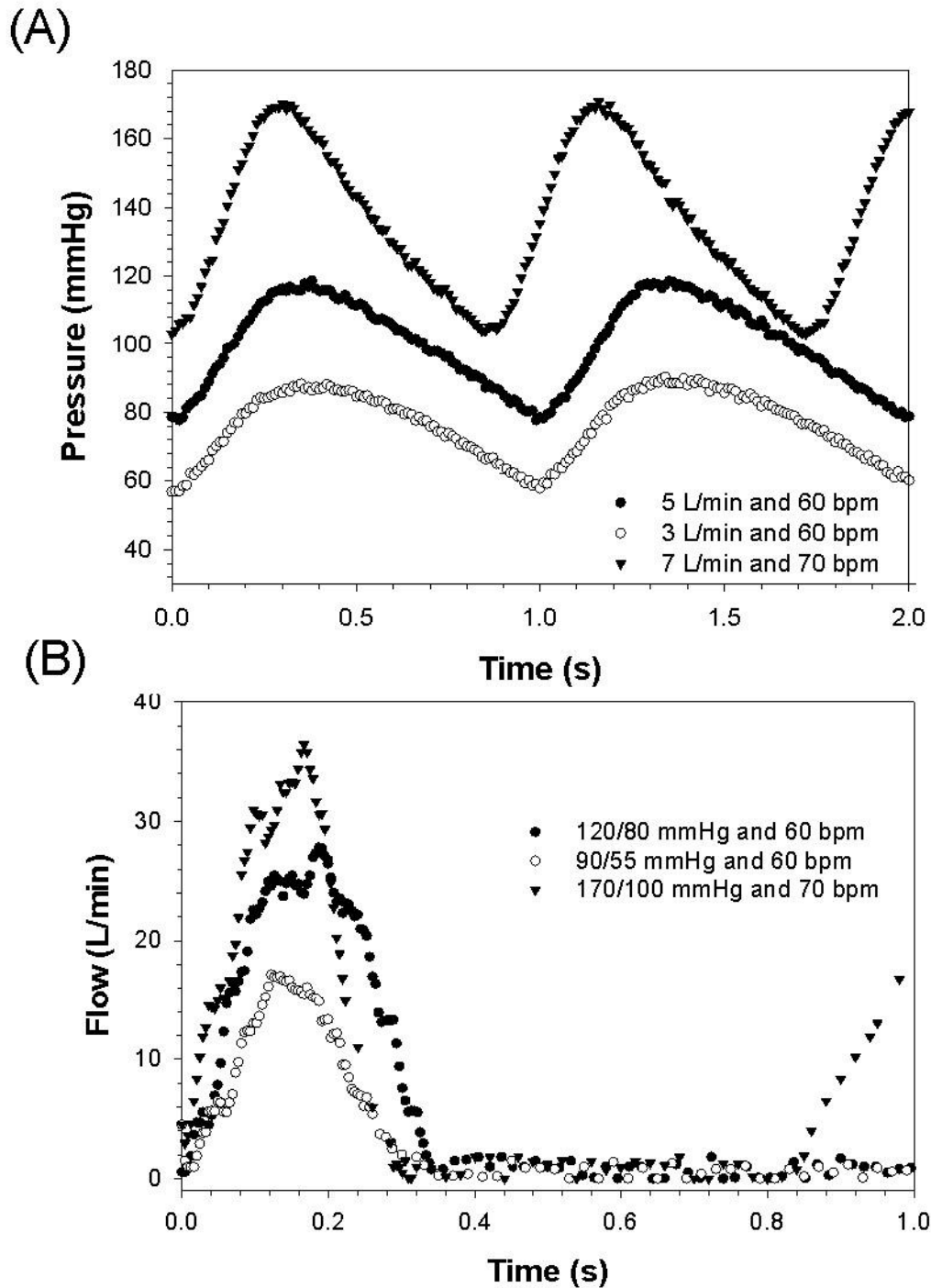


Figure 8.3 (A) pressure profiles measured for bird-beak configuration with PE=19 mm and $\theta = 20$ deg at different cardiac outputs; (B) flow profiles measured at aortic inlet.

8.2.3. FSI Computational Modeling

The experimental perfusion testing were reproduced via one-way FSI analyses from which hemodynamic connected to bird-beak configuration and mechanical forces on the endograft PE were extrapolated. FSI analyses were also applied to the four patients who underwent TEVAR.

Patients' specific geometries were discretized with GAMBIT v2.3.6 (ANSYS Inc., Canonsburg, PA) to obtain a fluid domain with 1 million of tetrahedral and a structural domain of approximately 300000 quadrilateral elements. The fluid mesh included the aortic lumen while the structural mesh included both the aortic and the PE wall. As described in the previous chapters, FSI analyses were performed coupling FLUENT v14.0.0 solve (ANSYS Inc., Canonsburg, PA) with ABAQUS v6.12 (SIMULIA Inc, Providence, RI) using a commercial software MpCCI v4.2 (Fraunhofer SCAI, Germany). Both codes shared a common boundary surface consisting on a) the undersurface and luminal surface of the endograft PE, and b) the aortic wall. These surfaces were used for the data exchange (i.e., wall stress forces) at every time step (0.1 s) upon the total analysis time (1 s).

CFD analyses were set as already specified in the previous chapters; fluid flow was considered as laminar since the highest Reynolds number ($Re=1710$), found in the patient D, was lower than the threshold value that distinguish between laminar and turbulent flow.

Stent was modeled without the sent frame and as a shell with thickness of 0.9 mm. Moreover, endograft compliance was iteratively adjusted to match infolding displacements measured by experimental testing. For the structural model, the bird-beak protrusion was assumed as a linear-elastic material with Poisson's ratio of 0.3 as previously described by Pasta et al. [8].

8.3. Results

It was observed that hemodynamic loads generated by physiological flow do not necessarily lead to stent-graft collapse. The implanted device tended to move from its starting position assumed during diastolic phase to final position assumed during systolic phase, as shown in the next figure, without failure risk evidence.

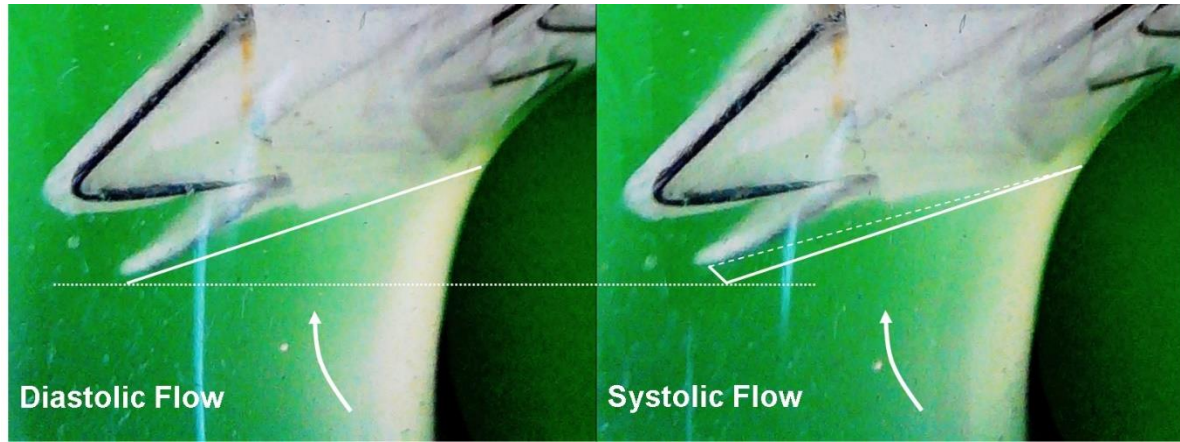


Figure 8.4: Photographs of TAG device infolding for the bird-beak configuration with PE=13 mm and $\theta = 24$ deg.

Both endograft displacement and rotation depend on the amount of cardiac cycle pulsatility and flow rate. Specifically, infolding increased from systemic pressure and flow rate of 90/55 mmHg and 3 L/min, respectively, to that one with pulse pressure of 170/100 mmHg and flow rate of 7 L/min.

In table (7.1) the preeminent role of PE dimension on TAG displacement was assessed, since infolding increases with greater device PE.

Table 8.1: TAG device displacements experimentally measured under different perfusion conditions.

	TAG Device Displacement (mm)		
	$\Delta P=90/55\text{mmHg};$ CO=3L/min	$\Delta P=120/80\text{mmHg};$ CO=5L/min	$\Delta P=170/100\text{mmHg};$ CO=7L/min
PE=13mm	0.26	0.39	0.65
PE=19mm	0.60	0.89	1.20
PE=24mm	0.72	1.01	1.66

Note: DP: systemic pressure; CO: cardiac output

Calibration of the bird-beak mechanical parameter under different hemodynamic conditions and bird-beak configurations revealed that the endograft compliance increases with higher systemic

pressure and flow rate (Figure 8.5). For a given hemodynamic condition, the endograft compliance linearly increased as the PE decreased.

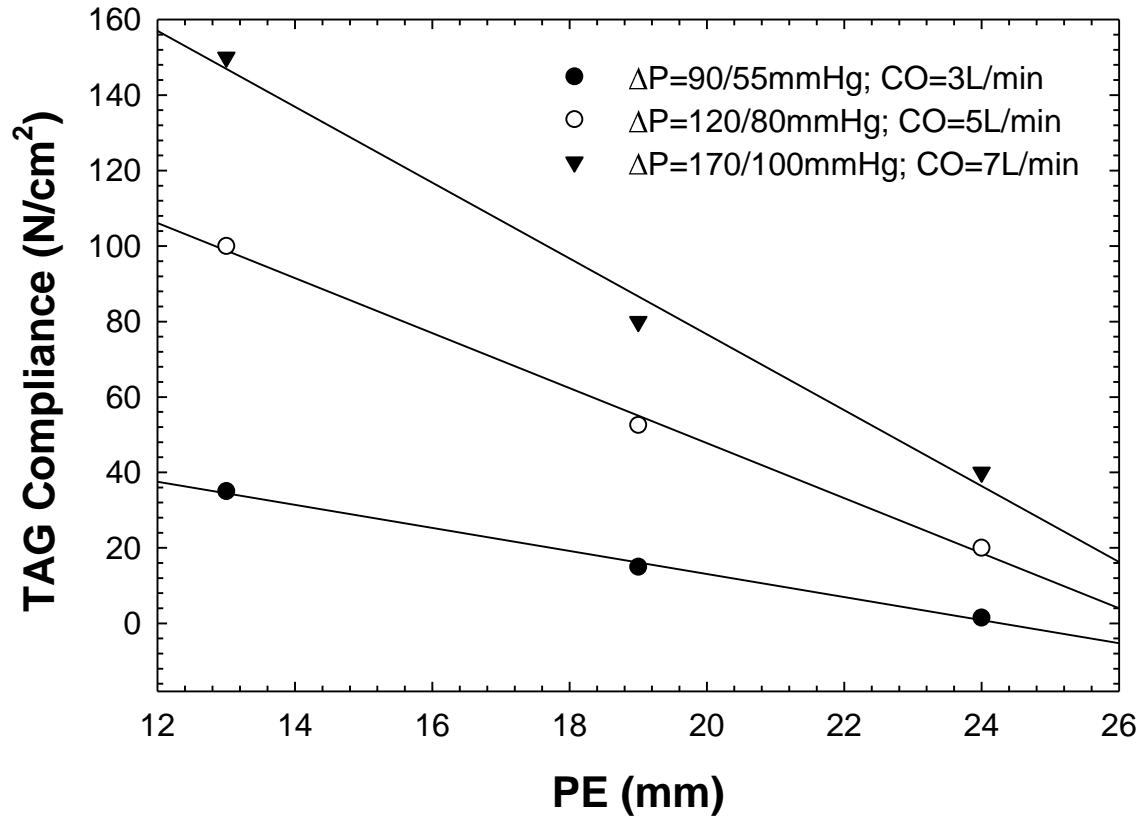


Figure 8.5: TAG compliance profiles obtained after iterative (manual) calibration of infolding parameters for the investigated hemodynamic scenarios ($R^2 > 0.96$ for all fitting curves).

It should be noticed that, in this work, the mentioned stent compliance is not the Young's modulus but rather a global parameter that describes the device behavior when exposed to particular hemodynamic load condition, geometrical configurations and device characterization.

Calibration of compliance was obtained on the first patient by comparing experimental and numerical results. Once compliance was calibrated, it was used in FSI analyses executed for all the patients; for these analyses, cardiac output was set equal to 5 L/min and systemic pressure equal to 120/80 mmHg. The four investigated stent graft had different PE ranging from 19 mm for the shorter to 28 mm for the longer.

CHAPTER 8: Towards the evaluation of the thoracic aortic stent graft failure risk related to endograft infolding

As shown in Figure 8.6, pressure map and velocity streamlines had a particular trend, if compared to healthy aorta, due to the presence of the stent graft and the bird-beak configuration inside the aortic lumen. In patients A, B and C systemic pressure followed a bimodal distribution with high pressure in the ascending aorta, aortic arch and supra-aortic vessel and lower pressure at the end of the stent graft in the thoracic descending aorta. This differential pressure between pre- and post-stent regions is symptom of a physiological coarctation of the vessel, resulting from the proximal protrusion of the thoracic aortic stent-graft into the arch as reported by Go and collaborators for Case A[9].

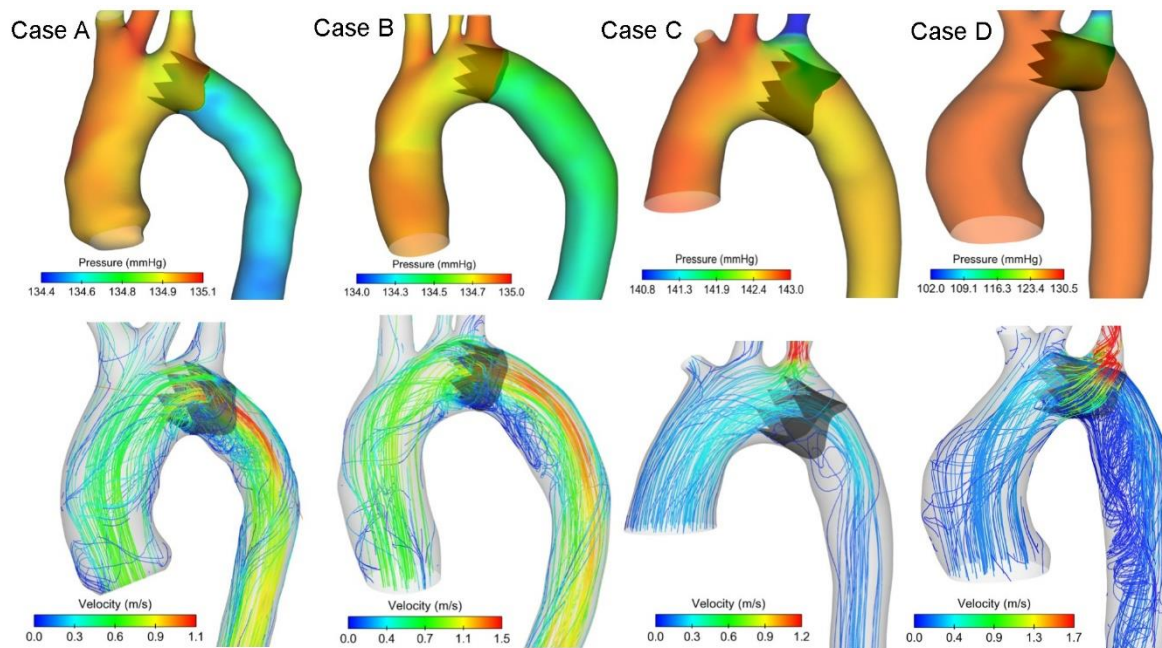


Figure 8.6: Pressure distribution (row above) and velocity streamlines (row below) at systolic peak for all patients with a protruded endograft wall; Case A with PE=19mm; Case B with PE=21mm; Case C with PE=26mm; Case D with PE=28mm

Pressure distribution were also investigated on the stent-graft wall and a sensible differential pressure between the outer and inner PE wall (i.e. transmural pressure) was found; specifically, this differential pressure increased with PE and reached the value of 18 mmHg for PE = 28 mm (case D).

CHAPTER 8: Towards the evaluation of the thoracic aortic stent graft failure risk related to endograft infolding

Transmural pressure and endograft infolding followed a particular trend (i.e. they increased with PE up to PE=26, but decreased for PE=28 mm); it should be considered that the particular parameters found in patient D (PE=28 mm) are strongly influenced by the ostium of the LSA which limits the TAG displacement (see figure 8.6).

Table 8.2: Transmural pressure across the protruded endograft wall and endograft displacements for all patients; Case A with PE=19mm; Case B with PE=21mm; Case C with PE=26mm; Case D with PE=28mm

	Case A	Case B	Case C	Case D
Transmural Pressure (mmHg)	0.89	1.26	2.85	8.72
Endograft Displacement (mm)	0.89	1.18	4.10	3.15

The graft implant influenced not only the pressure but also the hemodynamic scenario; specifically, the graft presence was cause of vortices in several regions of the aorta. Vortices, especially for patient D, were found at the proximal luminal surface of the endograft close to the smaller curvature of aortic arch; moreover, all the four investigated patients had vortices in the descending aorta where the fluid flows from a narrow region (i.e. TAG lumen) to a wider region (i.e. descending aortic lumen).

Mises stress were also studied with a focus on the eight-stent apices, where higher stress concentration were present as consequence of sharply-curved stent graft. As already found for other parameters, the longer the PE is the higher the Mises stress is (compare Case D with Case A). FSI analyses revealed a principal strain amplitude of 0.7% for Case C, which exhibited the highest device displacement of 4.10 mm and an unconstrained PE. Differently, other bird-beak configurations exhibited lower principal strain due to low device displacements (i.e., Case A and B) or anatomic constraining (Case D).

8.4. Conclusion

Aim of this study was to evaluate the mechanics on the base of stent-graft infolding or collapse; thus, hemodynamic and structural parameters, that may describe the influence of TAG implanted in aorta, were studied via experimental and numerical analyses.

The discussed results shown that, TAG device position and bird-beak protrusion extension into the aortic arch can severely influence the hemodynamic and structural loads exerted on the same device. Specifically, bird-beak protrusion extension has a relevant role on several parameters such as onset of a functional aortic coarctation (i.e., pressure drop) into the arch, hemodynamic disturbance in the aortic arch and descending aorta, device displacement, elevated trans-mural pressure and wall stress in to the stent-graft wall.

From results analysis it is possible to speculate that a bird-beak configuration with a PE= 21 mm necessitate of accurate clinical surveillance since it may lead to excessive endo-graft displacement. Our FSI results shown, for all the studied patients, a device infolding with a irrelevant or minimal influences on the mechanism of TAG device failure; specifically, all the hemodynamic and morphological parameter were not strong enough to cause device collapse. However, since the amplitude of principal strain observed for all the studied patients were comparable to the fatigue limit reported in literature, it is possible to conclude that TAG device could fail as consequence of material failure of the Nitinol stent-graft frame under the cyclic loading conditions imposed by the cardiac rhythm.

The results here obtained may be proposed as a starting point to project and design new devices that may be appropriate to be used safely in young patients.

Reference

1. Cheng, D., et al., *Endovascular aortic repair versus open surgical repair for descending thoracic aortic disease: a systematic review and meta-analysis of comparative studies*. Journal of the American College of Cardiology, 2010. **55**(10): p. 986-1001.
2. Makaroun, M.S., et al., *Five-year results of endovascular treatment with the Gore TAG device compared with open repair of thoracic aortic aneurysms*. Journal of vascular surgery, 2008. **47**(5): p. 912-918.
3. Steinbauer, M.G., et al., *Endovascular repair of proximal endograft collapse after treatment for thoracic aortic disease*. Journal of vascular surgery, 2006. **43**(3): p. 609-612.
4. Kasirajan, K., et al., *Incidence and outcomes after infolding or collapse of thoracic stent grafts*. Journal of vascular surgery, 2012. **55**(3): p. 652-658.
5. Shukla, A.J., G. Jeyabalan, and J.-S. Cho, *Late collapse of a thoracic endoprosthesis*. Journal of vascular surgery, 2011. **53**(3): p. 798-801.
6. Tsai, T.T., et al., *Tear size and location impacts false lumen pressure in an ex vivo model of chronic type B aortic dissection*. Journal of vascular surgery, 2008. **47**(4): p. 844-851.
7. Rudenick, P.A., et al., *An in vitro phantom study on the influence of tear size and configuration on the hemodynamics of the lumina in chronic type B aortic dissections*. Journal of vascular surgery, 2013. **57**(2): p. 464-474. e5.
8. Pasta, S., et al., *Computer modeling for the prediction of thoracic aortic stent graft collapse*. Journal of vascular surgery, 2013. **57**(5): p. 1353-1361.
9. Go, M.R., et al., *Physiologic coarctation of the aorta resulting from proximal protrusion of thoracic aortic stent grafts into the arch*. Journal of vascular surgery, 2008. **48**(4): p. 1007-1011.

Chapter 9

Conclusion

In this thesis, aortic pathologies were studied with the application of computational analyses to patient specific aortic geometries. The reliability of computational analyses, when applied to CVDs, was shown; in addition, in this thesis was assessed the possibility to integrate computational methods into the daily clinical practice in order to help physicians in their decision-making processes.

The main goal was to establish which hemodynamic features play a key role in the onset and growth of the ATAAs in order to improve the knowledge about aortic dilatation. Thus, analyses results shown that the particular valve morphology (i.e. BAV or TAV) influences the hemodynamic inside aorta and consequently influence the stresses on the aortic wall. It was found that patients with BAV had an eccentric blood flow jet angle and overload the AA wall if compared to TAV patients. Moreover, it was found that even among the patients with BAV there are huge hemodynamic differences on the base of aortic valve phenotypes (i.e. AP or RL).

The long-term goal is to substitute the actual criterion adopted by the physicians to decide about ATAA patient management with a new and more reliable criterion. The actual criterion is simply based on ATAA dimension and prescribes that ATAA patients should be treated

surgically if their aortic diameter is larger than 6.0 cm. However, this criterion failed several times (i.e. aneurysm rupture below the threshold value) and thus we propose a new approach that may account for multiple parameters such as aortic diameter, patient's clinical situation and parameters obtained from FSI analyses in order to support clinicians. In order to obtain this final criterion is necessary to collect and study a wider number of patients with ATAA.

The same approach was followed in the study of Type B AoD where CFD analyses were applied to aortic geometries with FL and TL. The main goal was to find some particular threshold value that might indicate if a pharmacological therapy would be enough for the patient management or if it was necessary a more aggressive procedure. It was found that patent and highly perfused FL is clinically associated with adverse patients' outcome. Moreover, from CFD analyses it was found that FL flow is strongly related to entry tear height; thus, it may be suggested that CFD analyses results should be combined with imaging technique to identify patients at higher risk of dissection-related complications.

This thesis poses the basis for future researches to obtain a wider integration of computational analyses on the clinical practice, both with a patient management criterion and with basic tool variables of interest estimation.

